Journal of Materials Chemistry A

ROYAL SOCIETY OF CHEMISTRY

REVIEW

Cite this: *J. Mater. Chem. A*, 2021, **9**, 1970

Chemical supercapacitors: a review focusing on metallic compounds and conducting polymers

Pappu Naskar, Apurba Maiti, Priyanka Chakraborty, Debojyoti Kundu, Biplab Biswas and Anjan Banerjee *

Capacitors began their journey in 1745, and to date have advanced in the form of supercapacitors. Supercapacitors are one of the advanced forms of capacitors with higher energy density, bridging capacitors and batteries. The energy storage through the formation of an electrical double layer is pivotal for supercapacitor technology. Accordingly, to further improve the energy density, surface faradaic (pseudocapacitive) processes are employed, and henceforth, the journey of chemical supercapacitors commenced. Herein, the materials, mechanisms and fabrication of chemical supercapacitors based on metallic compounds and conducting polymers are discussed in detail. The inherent limitations of these materials are addressed, and the feasible mitigation measures are identified. Poor conductivity, slow diffusion kinetics and rapid structural disintegration over cycling are the common constraints of metallic compounds, which can be overcome by preparing conductive nanocomposites. Thus, versatile conductive nanocomposites of metal oxides, hydroxides, carbides, nitrides, phosphides, phosphates, phosphites, and chalcogenides are elaborated. A lack of structural integrity is the prime obstacle for the realization of conducting polymer-based supercapacitors, which may be solved by forming composites with robust support from carbonaceous materials or metallic compounds. Consequently, the composites of polyaniline, polypyrrole, polythiophene and polythiophene-derivatives are discussed. The historical accounts of early stages of works are emphasised in order to review the developmental pathways of chemical supercapacitors. The construction of full cells and their performance data are presented herein, which synchronize the behaviour of practical scaled-up devices. To the best of our knowledge, this review is the first holistic description of chemical supercapacitors based on metallic compounds and conducting polymers from the first reports to recent advancements.

Received 2nd October 2020
Accepted 24th November 2020

DOI: 10.1039/d0ta09655e

rsc.li/materials-a

1. What is a capacitor?

There are records[1] that German scientist Ewald Georg von Kleist invented the capacitor in November 1745. A couple of months later, Dutch Professor Pieter van Musschenbroek, at the

Department of Chemistry, Presidency University-Kolkata, 86/1 College Street, Kolkata-700073, India. E-mail: anjan.chem@presiuniv.ac.in

Mr Pappu Naskar received his BSc Degree (2014) from the University of Calcutta, India, and was awarded an MSc Degree (2017) in Chemistry from Chhatrapati Shahu Ji Maharaj University, India. Currently, he is a PhD scholar at Presidency University, Kolkata, India, and actively working in the field of electrochemical energy storage systems (batteries and supercapacitors) for a sustainable future.

Mr Apurba Maiti received his BSc Degree (2018) from The University of Burdwan, India, and was awarded an MSc Degree (2020) in Chemistry from Presidency University, Kolkata, India. Currently, he is a project intern, and extending his MSc project on conducting polymer-based supercapacitors, especially focusing on the electrochemical characterization of polythiophene derivatives.

University of Leyden, came up with a similar device in the form of the Leyden jar, which is typically accredited as the first capacitor. Henceforth, the research and development on capacitors have become one of the major research topics in the physical and chemical sciences. A capacitor is a passive electronic module containing a pair of conducting plates disjointed by a dielectric medium. Capacitors accumulate electrical energy as electrostatic charge division with equal amounts of positive and negative charges on opposite faces of the conducting plates. Consequently, a voltage difference is generated between the plates. By connecting two plates with an external load, current flows until complete charge balance is achieved, and the stored energy is entirely delivered. The capacitor can then be recharged by applying voltage from an external power supply. Since the charge is stored physically (non-faradaic) without any chemical/phase changes (faradaic), the charge/discharge schedule is highly reversible, and the service life of a capacitor is virtually unlimited.

The amount of charge (Q) stored in a capacitor is proportional to the system voltage (V), and the proportionality constant (C) is called capacitance, *i.e.*

$$Q = CV \tag{1}$$

Reorganizing these terms,

$$C = Q/V \tag{2}$$

For a capacitor, capacitance (in farad/F) is directly proportional to the geometric area of the plate (A), inversely proportional to the inter-plate separation (d) and also depends on the

Ms Priyanka Chakraborty received her BSc Degree (2018) from the University of Calcutta, India, and was awarded an MSc degree (2020) in Chemistry from Presidency University, Kolkata, India. Currently, she is a project intern, and extending her MSc project on metal oxide/hydroxide materials for supercapacitor devices. She is actively working on various carbon composites of oxides/hydroxides for greater performances.

Dr Biplab Biswas was awarded a PhD Degree (2008) from the Max Planck Institute for Bioinorganic Chemistry Muelheim an der Ruhr, Germany and continued his postdoctoral research at the same institute until 2009. He carried out others post-doctoral research in CEA Grenoble, France (2009–2011) and Karlsruhe Institute of Technology, Germany (2011–2013). Presently, he is an Assistant Professor in Chemistry at Presidency University, Kolkata, India. He has expertise in various fields in inorganic and materials chemistry, including coordination chemistry, magneto-chemistry, spectroscopy, radical chemistry, catalysis and environmental sciences. He has nineteen publications in internationally reputed peer-reviewed journals.

Mr Debojyoti Kundu received his BSc Degree (2018) from The University of Burdwan, India, and was awarded an MSc Degree (2020) in Chemistry from Presidency University, Kolkata, India. Currently, he is a project intern, and extending his MSc project on the pseudocapacitive characterization of nitrides/phosphides/sulfides. The surface modulations of these materials are the prime focus of his research for the improved durability of supercapacitors.

Dr Anjan Banerjee was received his PhD degree (2014) from the Indian Institute of Science, Bangalore, India and carried out post-doctoral research at Bar-Ilan University, Israel (2015–2017). He was associated with different battery manufacturing industries in India from 2017 to 2018. Currently, he is serving at Presidency University, Kolkata, India as an Assistant Professor in Chemistry. His research activities are focused on electrochemical energy storage systems, especially Li-ion batteries, Na-ion batteries, lead-acid batteries, flow batteries and supercapacitors. The major focus of his research is device development for practical applications. He has filed six patents (four US & two Indian patents) and published twenty-eight articles in reputed peer-reviewed journals.

permittivity of the medium (ε in F m^{-1}). Accordingly, the capacitance of a capacitor is demonstrated by,

$$C = \varepsilon A/d \quad (3)$$

For vacuum, the value of absolute permittivity (ε_o) is 8.85 × 10^{-12} F m^{-1}.[2] For any other material, permittivity (ε) is measured by the multiplication of the relative permittivity (ε_r) of the material and absolute permittivity (ε_o).

Accordingly, eqn (3) can be rewritten as,

$$C = \varepsilon_o \varepsilon_r (A/d) \quad (4)$$

In practice, the capacitance of a capacitor may be estimated from its galvanostatic charge/discharge profiles. For each galvanostatic charge/discharge of the capacitor, its capacitance is estimated from the equation

$$C = It/\Delta V \quad (5)$$

where I is the charge/discharge current, t is the charge/discharge time and ΔV is the voltage difference between the initial and final states, respectively.

The electrical energy (E) accumulated in a capacitor is

$$E = \int (Q/C) \mathrm{d}Q \quad (6)$$

As the voltage of the capacitor increases from 0 to V, the charge stored on the electrode increases from 0 to Q, and consequently, the accumulated energy E is presented as[3]

$$E = (1/C) \times \left(\frac{1}{2}Q^2\right) = \frac{1}{2}CV^2 \quad (7)$$

One of the functional characteristics of a capacitor is its response time or time constant (τ), which is the multiplication of its resistance (R) and capacitance (C). Capacitors with small time constant acquire/deliver energy in a relatively short time, while those with high time constant charge/discharge over a relatively longer time. Hence, the maximum power[4] (rate of energy acquiring or delivering, expressed in watt) of a capacitor is evaluated from the ratio of energy (watt-second) and response time (second).

The equivalent circuit diagram of a capacitor is shown in Fig. 1, which is constructed by three components, *i.e.* the capacitance (C), equivalent series resistance (ESR) and equivalent parallel resistance (EPR). The ESR represents the resistive loss through internal heating of the capacitor. The EPR of a capacitor is linked with the leakage current, which impacts the self-discharge voltage loss. There is no self-discharge of an ideal capacitor. Nevertheless, self-discharge is the most common phenomenon for all practical capacitors due to thermal randomization of dipoles and parasitic processes through the dielectric medium. The self-discharge rate of a capacitor is measured by the float (leakage) current across the device terminals in the fully charged state. To preserve 100% state-of-charge, the float current counteracts the self-discharge voltage loss.[5]

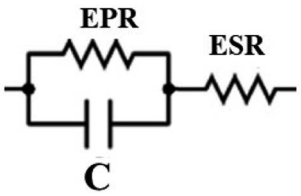

Fig. 1 Simplified equivalent circuit for a capacitor.

2. The journey from capacitors to supercapacitors

2.1. Classification of capacitors

Based on the response time or time constant (τ), capacitors can be classified into three broad groups,[6] namely, electrostatic capacitors, electrolytic capacitors and electrochemical capacitors. The utility of each group is unique in real life applications. Electrostatic capacitors[7] consist of dielectric media, such as air, mica, polymer films, and ceramics, sandwiched between two conducting electrodes. These capacitors function in the GHz frequency range and are characterized by lowest capacitance values among of the three groups. Electrolytic capacitors[8] are polarized capacitors that employ suitable electrolytes (solid, liquid or gel) to achieve greater energy (~10 times higher) than former. These capacitors can usually be operated at a frequency of up to ~20 kHz. The operating principle of an electrochemical capacitor is based on the formation of an electrical double-layer (EDL). It is acknowledged that an EDL is generated at the electrode/electrolyte interface by physical charge separation. The EDL[9] may extend to about a few angstroms (Å), and stores electrostatic energy like a capacitor. The capacitance values of electrochemical capacitors are appreciably high compared to the other two groups, and thus can be envisaged for possible energy storage applications. On the contrary, by the virtue of their high frequency responses, electrostatic and electrolytic capacitors have immense applications in electrical/electronic engineering. The construction and characteristic of these three different types of capacitors are depicted in Fig. 2.

2.2. Why electrochemical capacitors are termed super (or ultra) capacitors?

It is evident from eqn (4) that the capacitance of a capacitor can be enhanced by increasing its surface area and decreasing the distance between its two oppositely charged layers. In electrochemical capacitors, the formation of an EDL is the origin of the capacitance, while, the charge-separation distance in the EDL is in molecular dimensions, *i.e.*, less than 10^{-9} m. On the other hand, high surface area (~10^6 m^2 kg^{-1}) activated carbons are conventionally used as active materials for electrochemical capacitors. The relative permittivity or dielectric constant at the primary adsorption polarized solvent layer (water medium) is nearly 6.[10] Hence, the capacitance of electrochemical capacitors will be ($6 \times 8.8 \times 10^{-12} \times 10^6$)/$10^{-9}$, *i.e.* ~$10^4$ F kg^{-1}.[11–14] Due to the high value

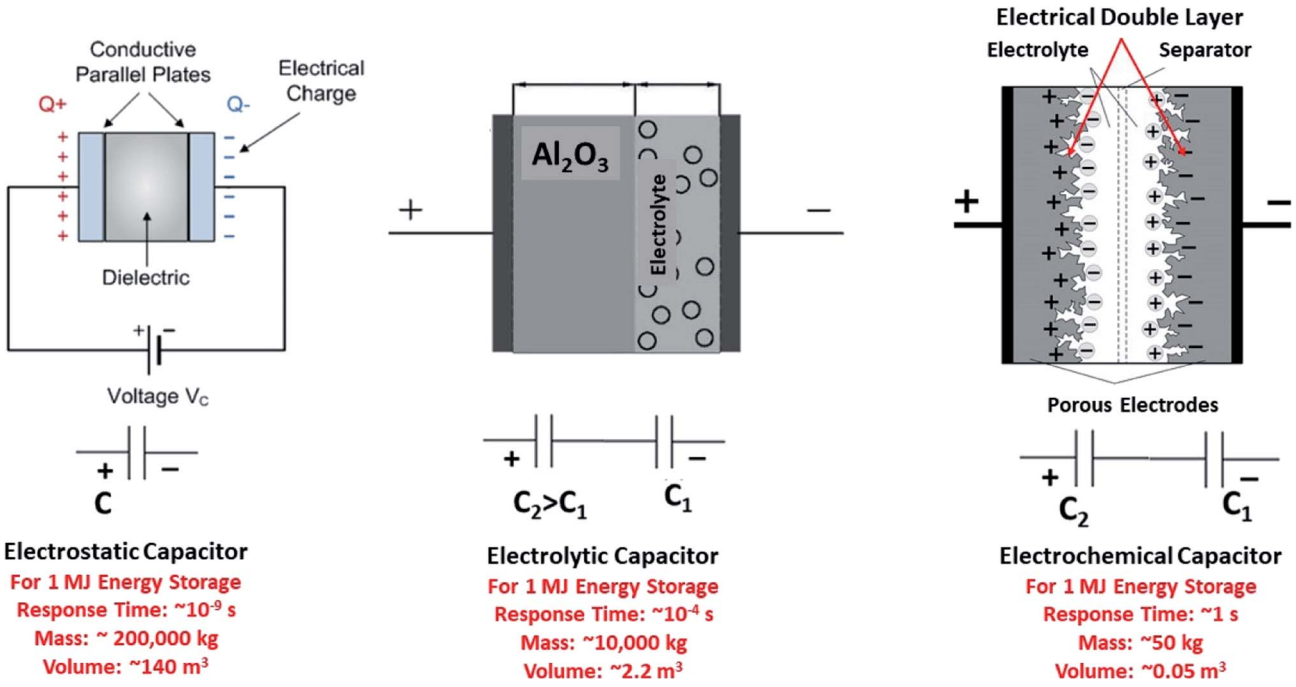

Fig. 2 Construction and characteristic features of electrostatic, electrolytic and electrochemical capacitors.[2]

(many thousands of farad) of capacitance, electrochemical capacitors are termed supercapacitors or ultracapacitors. Fig. 3(a–d) depict the electrochemical cell construction, respective equivalent circuit, microscopic illustration of the EDL and potential gradient in the EDL for typical supercapacitors, respectively.[9,10]

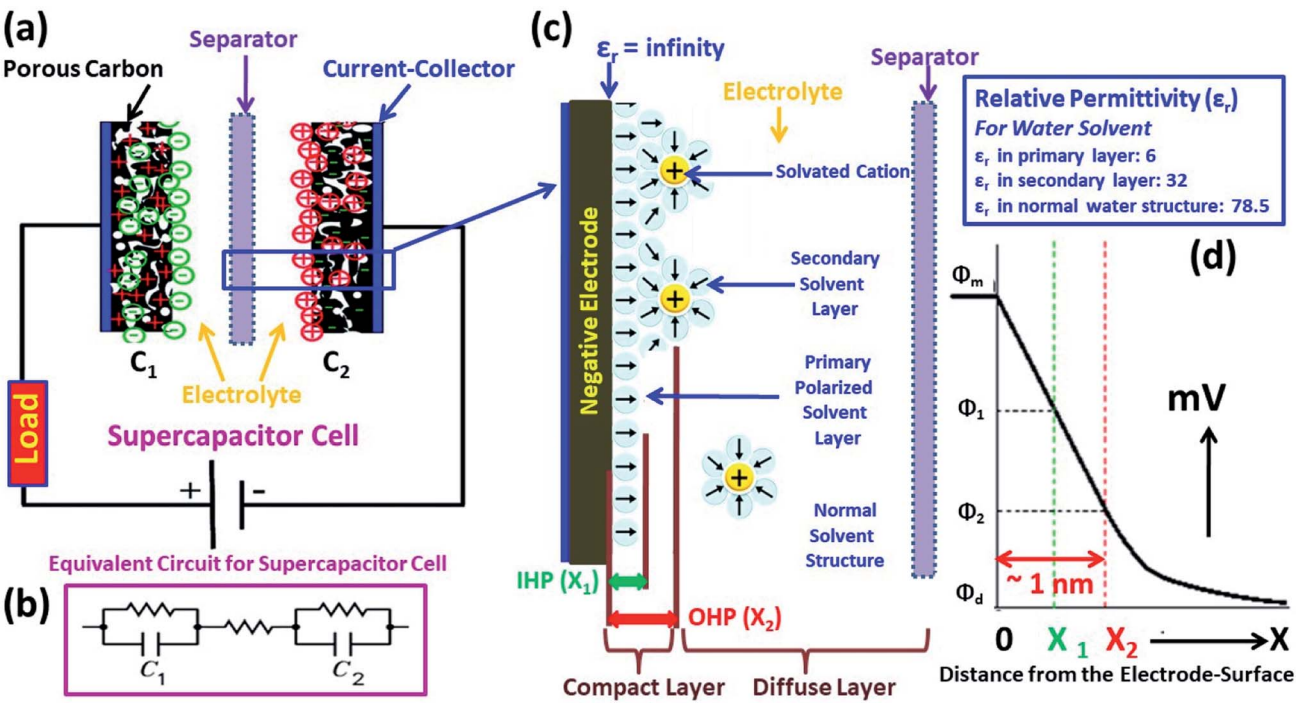

Fig. 3 Schematic illustration of a supercapacitor: (a) electrochemical cell construction; (b) simplified equivalent circuit for supercapacitor cell; and (c) microscopic illustration of EDL: the inner Helmholtz plane (IHP) passes through the centre of the primary polarized solvent layer and outer Helmholtz plane (OHP) passes through the centre of oppositely charged solvated ions at the closest distance towards electrode. Between the electrode and OHP region is a compact-layer (~1 nm separation) and beyond the OHP is termed the diffuse layer. The variation in the relative permittivity at different positions of the EDL in aqueous electrolyte is mentioned in the blue box, and the value at the metallic electrode surface is infinity. (d) Potential (mV) gradient in EDL: Φ_m, Φ_1, Φ_2 and Φ_d represent the potentials at the metallic substrate, IHP, OHP and diffuse-layer.[10]

2.3. Classification of supercapacitors

Mechanistically, supercapacitors are classified into two groups, namely, electrical double-layer capacitors (EDLC) and pseudocapacitors. In his path-finding book, namely, 'Electrochemical supercapacitors: scientific fundamentals and technological applications'[9] Conway stated that "Regular double layer capacitance arises from the potential-dependence of the surface density of charges stored electrostatically (*i.e.*, non-faradaically) at the interfaces of the capacitor electrodes. Pseudocapacitance arises at the electrode surfaces, where a completely different charge-storage mechanism applies. It is faradaic in origin, involving the passage of charge across the double layer, as in battery charging or discharging, but capacitance arises due to the special relation that can originate for thermodynamic reasons between the extent of charge acceptance (Δq) and change in potential (ΔV), and thus the derivative $\mathrm{d}(\Delta q)/\mathrm{d}(\Delta V)$ or $\mathrm{d}q/\mathrm{d}V$, which is equivalent to capacitance, can be formulated and experimentally measured by the dc, ac, or transient techniques". Therefore, non-faradaic (capacitive) physical charge separation through the formation of an EDL is the operating principle of EDLC-type supercapacitors. Diverse carbonaceous materials, such as activated carbon (AC), carbon black (CB), graphite, graphene (single and multi-layer), graphene oxide (GO), reduced graphene oxide (rGO), single- and multi-walled carbon nanotubes (SWCNT and MWCNT), carbon nanofibers (CNF), carbon nanorods, are employed in EDLC devices.[15,16] On the other hand, pseudocapacitors operated with surface-controlled pseudo-faradaic (pseudocapacitive) charge storage mechanisms. In the 1990s, Conway and his group identified two distinct pseudocapacitive processes, *i.e.*, redox pseudocapacitance and intercalation pseudocapacitance.[9] The former occurs when ions are specifically adsorbed on the electrode surface by electrochemical means and participate in faradaic charge-transfer between the electrode/electrolyte interface. The latter occurs when ions intercalate/deintercalate in/from the redox active host frameworks associated with faradaic electron-transfer devoid of crystallographic phase changes. Various conducting polymers, metal oxides, hydroxides, carbides, nitrides, phosphides, phosphates, phosphites, chalcogenides, *etc.* are conventionally utilized in pseudocapacitors.[17–21] Unlike surface-controlled pseudo-faradaic process, the faradaic charge-transfer process is directed by diffusion-controlled mass-transfer limitations, which occurs in the bulk of the active materials of the electrode.[9,22,23] Importantly, all battery technologies are developed based on faradaic charge-transfer mechanisms, which are responsible for their large energy storage capacity and low power capability. In contrast, due to the surface-controlled operating processes, EDLCs and pseudocapacitors are characterized by high power capability with lower energy storage capacity. In practical electrochemical energy storage systems, the diffusion-controlled faradaic processes and surface-controlled non-faradaic/pseudo-faradaic processes coexist with varying proportions. Eventually, the contributory diffusion-controlled and surface-controlled processes can be qualitatively and quantitatively analysed *via* cyclic voltammetry, which are depicted by eqn (8) and (9), respectively.[24]

$$i = av^b \tag{8}$$

$$i(v) = k_1 v + k_2 v^{1/2} \tag{9}$$

where i and v are the current response and scan rate, respectively, and a and b are characteristic constants. $b = 0.5$ indicates a diffusion-controlled faradaic process according to the Randles–Sevcik equation, whereas, $b = 1$ suggests surface-controlled non-faradaic/pseudo-faradaic processes. k_1 and k_2 are the coefficients related to the surface-controlled and diffusion-controlled mechanisms, respectively.

Construction-wise, supercapacitors are categorized in three different classes, namely, EDLC, pseudocapacitor and hybrid supercapacitor. The possible materials and mechanisms of EDLCs and pseudocapacitors are mentioned above. These can be constructed by either symmetric (employing the same material in both electrodes) or asymmetric (employing different materials in different electrodes) configurations. Moreover, the coupling of an EDLC and pseudocapacitor is also designated as an asymmetric supercapacitor. On the other hand, hybrid supercapacitors[25] are constructed *via* the smart coupling of battery electrodes (diffusion-controlled) with capacitive/pseudocapacitive electrodes (surface-controlled). Therefore, the power and energy characteristics of hybrid supercapacitors can be tuned by optimization of the non-faradaic, pseudo-faradaic and faradaic contributions towards total charge storage. However, according to the operating principles, EDLC is identified as a physical supercapacitor, whereas, pseudocapacitors and hybrid supercapacitors can be considered chemical supercapacitors.

3. Materials, construction and characterization of chemical supercapacitors

In the pseudocapacitive arena, materials having reversible electron transfer capability between their oxidised and reduced forms with minimal charge-transfer and mass-transfer resistances can be used as active materials. Additionally, materials should have chemical, electrochemical and thermal stability within the operating windows. During prolonged charge and discharge, permanent deformations in the active materials are unavoidable, but these permanent structural disintegrations should be initiated after hundreds to thousands of cycles for commercially successful devices. Thus, based on the above-mentioned criteria, only a few classes of materials exhibit potential for pseudocapacitive applications, including conducting polymers, metal oxides, hydroxides, carbides, nitrides, phosphides, phosphates, phosphites, and chalcogenides. Among the different metallic compounds, RuO_2, MnO_x, NiO, CoO_x, VO_x, FeO_x, $Ni(OH)_2$, $Co(OH)_2$, NiCo-layered double hydroxide (LDH), NiFe-LDH, Ti_3C_2, TiC, VN, TiN, Ni_2P, $Ni_2P_2O_7$, $Co_3(PO_4)_2$, $NiHPO_3$, MoS_2, WS_2, and $Co_{0.85}Se$ exhibit promising

performances[18–21] in terms of capacitance, energy density and operational life. These materials are extremely stable and robust under the operating conditions. On the other hand, conducting polymers, such as polyaniline (PANI), polypyrrole (PPy), polythiophene (PTh) and derivatives of PTh, are important candidates for pseudocapacitive applications because of their high conductivity, high capacitance, environmental benign nature, low cost and flexibility.[17] These chemical supercapacitors are mostly assembled in aqueous media with few exceptions, whereas organic media and ionic liquids (ILs) are employed.[9,17,18] As an aqueous system, the full cell voltage is thermodynamically limited at 1.23 V due to the breakdown of water molecules.[26] At different electrode surfaces, the overpotential values for the oxygen and hydrogen evolution reactions kinetically deviate from thermodynamic standards, and hence, the full cell voltage can be varied from the exact value of 1.23 V. In reality, the device voltage kinetically varies from 1 to 1.5 V (upper limit may increase up to 1.8 V in a few instances) for different materials in acidic and alkaline media, except, Pb-based systems, which exhibit ~2 V in acidic media.[2,9] On the other hand, surface insertion/deinsertion-mediated aqueous pseudocapacitors are used to fabricate cells in neutral media, and the full cells exhibit an ~2 V rated voltage due to the higher overpotentials of the hydrogen and oxygen evolution reactions.[9] However, safe and hazard-free devices result from aqueous media by compromising the higher voltage limits (above 2.5 V) and higher energy densities compared to that in nonaqueous media. On the other hand, high power characteristics are achieved in aqueous systems because of the higher ionic mobility in water medium compared to organic solvents.[27]

Recently, a new class of materials, namely, metal–organic-frameworks (MOFs), are considered for pseudocapacitive systems[28] due to their diverse scaffold structures, flexible pore sizes, large surface area (>6000 $m^2\ g^{-1}$), and abundant metallic redox sites. In 1995, Yaghi[29] defined MOFs as crystalline coordination polymers produced *via* self-assembly, resulting in a highly structured infinite network. These coordination polymers consist of metal ions or ion clusters and organic ligands connected through coordination bonds, auxiliary hydrogen-bonds, π–π stacking, metallic bonding or van der Walls forces. In the case of MOFs, their specialized interconnected pore channels permit efficient electrolyte infiltration, which shortens the diffusion pathways of electrolyte ions, and hence, fast kinetics is achieved. However, besides metallic compounds, conducting polymers and MOFs, a few other advanced multifunctional materials may be applied in chemical supercapacitors, including covalent-organic-frameworks (COFs),[30,31] heteroatom-doped carbonaceous materials,[32–35] bio-waste-derived carbons with redox functionalities,[36,37] black phosphorous,[38] mixed conductors,[39] perovskite nanoparticles,[40] polyoxometalates (POMs),[41,42] and redox active electrolytes.[43–45] Nevertheless, this review focuses on metallic compounds and conducting polymers for the construction of chemical supercapacitors.

Device construction is carried out with optimized electrodes, electrolytes, current-collectors, separators and other passive components upon their successful characterization using various electrochemical tools, such as cyclic voltammetry (CV), linear swipe voltammetry (LSV), electrochemical impedance spectroscopy (EIS), galvanostatic charge/discharge (GCD), chronoamperometry, and Tafel polarization. The key parameter of a good performance full cell is the charge balance ($Q_{pos} = Q_{neg}$) between its positive and negative electrodes, and thus an optimized mass balance between these two electrodes is essential. The mass balance formulism is represented as eqn (10).

$$M_{pos}/M_{neg} = (C_{neg} \times \Delta V_{neg})/(C_{pos} \times \Delta V_{pos}) \quad (10)$$

where M, C and ΔV are the mass, specific capacitance and operating voltage range for each electrode, respectively. The four major performance parameters of an energy storage device, namely, specific capacity/capacitance, energy density, power density and durability are emphasised herein since these characteristics are a matter-of-concern for end-users. The formulas to determine the energy density (E/W h kg^{-1}) and power density (P/W kg^{-1}) of a supercapacitor device are as follows:[46]

$$E = \frac{1}{2 \times 3.6} \times C_{cell} \times V^2 \quad (11)$$

$$P = \frac{E}{t} \quad (12)$$

where C_{cell}, V and t are the specific capacitance (F g^{-1}), rated voltage (V) and discharge time (h), respectively.

or[47]

$$P = \Delta V \times \frac{I}{m} \quad (13)$$

$$E = P \times \frac{t}{3600} \quad (14)$$

$$\Delta V = \frac{V_{max} + V_{min}}{2} \quad (15)$$

where I, m, t, V_{max} and V_{min} are the applied current (A), mass (kg), discharge time (s), maximum and minimum voltages (V) of operation, respectively.

4. Chemical supercapacitors based on metallic compounds

Minimally diffusion limited reversible surface-faradaic reactions, which are distinctly different from battery-type bulk-faradaic reactions, are the realization of pseudocapacitive mechanisms. In 1971, the pseudocapacitive characteristics were first recognized on RuO_2 films through nearly rectangular CV in 1 M $HClO_4$ electrolyte by Trasatti and Buzzanca.[48] These authors interpreted the electrochemical behaviour of the RuO_2 films in terms of hydration-driven non-stoichiometry. In the hydrous oxide, Ru^{3+} is balanced by the protons in its lattice according to the following reaction.

$$RuO_2 + xe^- + xH^+ \rightarrow RuO_{2-x}(OH)_x \quad (16)$$

In 1974, Galizzioli, Tantardini and Trasatti[49] published further detailed electrochemical studies on RuO_2 films together with possible mechanisms. Here, the authors identified the reversible redox reactions of RuO_2 in acidic medium as follows:

$$2RuO_2 + 2H^+ + 2e^- \leftrightarrow Ru_2O_3 + H_2O \quad (17)$$

In acidic medium, RuO_2 rapidly equilibrates with protons at the interface and demonstrates the initial rest voltage of 0.94 V *vs.* normal hydrogen electrode (NHE). Nonetheless, in open circuit conditions, the voltage decreases to 0.74 *vs.* NHE due to time-dependent self-discharge. In the case of the surface of RuO_2 films, eqn (18) is the preferable representation, instead of eqn (17), as the true scenario.

$$RuO_2 + H^+ + e^- \leftrightarrow RuOOH \quad (18)$$

The Gibbs formation energy of RuO_2 depicts a value of 0.43 V *vs.* NHE, which signifies the following reaction:

$$RuO_2 + 4H^+ + 4e^- \leftrightarrow Ru + 2H_2O \quad (19)$$

Notably, 0.43 V is not the stationary potential in acidic medium because RuO_2 hardly reduces to metallic state under a negative sweep in CV. However, the non-stoichiometry, availability of several successive redox states (+2, +3, +4 and even +6) and high electronic conductivity (order of 10^4 ohm^{-1} cm^{-1}) are primarily responsible for good pseudocapacitance of RuO_2 electrodes. After the initial work of Trasatti,[48,49] Conway and co-workers[50,51] demonstrated the pseudocapacitive behaviours of RuO_2 films that were anodically synthesized on metallic Ru at a scan rate of 25 mV s^{-1} in the voltage range of 0.05–1.40 V *vs.* reversible hydrogen electrode (RHE) in aqueous H_2SO_4 solution. The CV responses of the anodically formed RuO_2 films were found to be more reversible compared to the thermally formed RuO_2 films reported by Trasatti and co-workers. Soon after the publication by Conway *et al.*,[50] in 1975, the Ottawa group developed the first RuO_2-based commercial supercapacitors in collaboration with Continental Group Inc.[9] Additionally, IrO_2, WO_3, MoO_3, Co_3O_4 and molybdenum nitrides also exhibit pseudocapacitance in aqueous medium *via* a similar mechanism to that of RuO_2.[52,53] Nevertheless, these materials show a lower potential range (0.8 V *vs.* RHE) than that of RuO_2. In 1997, Miller *et al.*[54] synthesized a high surface area (434.5 m^2 g^{-1}) Ru/carbon aerogel composite electrode, where the electrochemically oxidized Ru particles provided pseudocapacitance and drastically improved the specific capacitance of the aerogel. The composite electrode showed a specific capacitances of 206 F g^{-1} in contrast to 95 F g^{-1} for the pristine aerogel at a scan rate of 2 mV s^{-1} in the voltage range of 0–0.8 V *vs.* standard calomel electrode (SCE) in 1 M H_2SO_4 electrolyte. The development of pseudocapacitors started from the abovementioned pioneering works, and consequently, today pseudocapacitors have a significant contribution in the energy storage sector. In modern science, the arena of pseudocapacitors is expanding from metal oxides to other metallic compounds (such as hydroxides, carbides, nitrides, phosphides, phosphates, phosphites, and chalcogenides), conducting polymers, MOFs, COFs, *etc.* However, besides a few exceptions, metallic compounds are not adequately conducting to achieve successful pseudocapacitive reactions. Thus, to circumvent this limitation, nanostructuring and the fabrication of composite with conductive matrices are intensively carried out. However, metallic compound-based supercapacitors achieve higher energy densities compared to EDLCs due to the pseudo-faradaic charge storage, while nanostructuring and composites with conductive matrices offer appreciable power densities that are marginally lower than that of EDLCs. Consequently, chemical supercapacitors based on various metallic compounds have attracted commercial attention.

4.1. Metal oxides and composites

The concept of pseudocapacitance originated from a metal oxide, namely RuO_2, as previously mentioned. In this section, we will briefly discuss the pseudocapacitance behaviours of various metal oxides and their composites.

4.1.1. Ruthenium oxide and composites. The underneath pseudocapacitance mechanisms of RuO_2 was further investigated in detail by several researchers. In 1995, Zheng *et al.*[55] proposed a four-step mechanism to determine the pseudocapacitance of hydrous oxide ($RuO_x \cdot nH_2O$) as follows: (i) electron hopping within $RuO_x \cdot nH_2O$ primary particles, (ii) electron hopping between particles, (iii) electron hopping between electrode materials and current collectors, and (iv) proton diffusion within $RuO_x \cdot nH_2O$ particles. Crystallization reduces the intra-particle electron hopping resistance of $RuO_x \cdot nH_2O$, while it increases the diffusion barrier of protons within crystallites and minimizes the active mass utilization.[56] Therefore, the highest specific capacitance is achieved when the annealing temperature of nanocrystalline $RuO_x \cdot nH_2O$ is set slightly below the crystalline temperature.[55,57] However, recent research focused on amorphous hydrous $RuO_x \cdot nH_2O$ thin films for supercapacitor applications due to their high specific capacitance, high conductivity and good cycling stability.[58–62] Different methods may be employed for synthesizing amorphous hydrous oxides, such as electrochemical deposition, sol–gel synthesis, spray deposition, hydrothermal synthesis, and oxidative synthesis.[59–61] In 1999, Long *et al.*[62] reported a specific capacitance of ~900 F g^{-1} for $RuO_2 \cdot 0.5H_2O$ (surface area: 75 m^2 g^{-1}) at 2 mV s^{-1} in the voltage range of 0–0.8 V *vs.* SCE in 0.5 M H_2SO_4 electrolyte, which decreased to ~29 F g^{-1} for $RuO_2 \cdot 0.3H_2O$ (surface area: 30 m^2 g^{-1}) due to the reduction of the water content in hydrous oxide. Diverse composite materials have been designed to enhance the electrochemical performances of RuO_2. In 2001, Kim *et al.*[63] synthesized amorphous $RuO_x \cdot nH_2O$/carbon nanocomposites with varying $RuO_x \cdot nH_2O$ loadings *via* a colloidal method, where the annealing temperature was set to 100 °C. The optimized composition (40 wt% Ru, surface area: 201 m^2 g^{-1}) exhibited a specific capacitance of 407 F g^{-1} at 1 mV s^{-1} in the voltage range of 0–0.9 V *vs.* SCE in 1 M H_2SO_4 electrolyte. The pseudocapacitance contribution from only $RuO_x \cdot nH_2O$ was calculated to be 863 F g^{-1} by subtracting the EDL contribution resulting from carbon (Vulcan XC-72 CB)

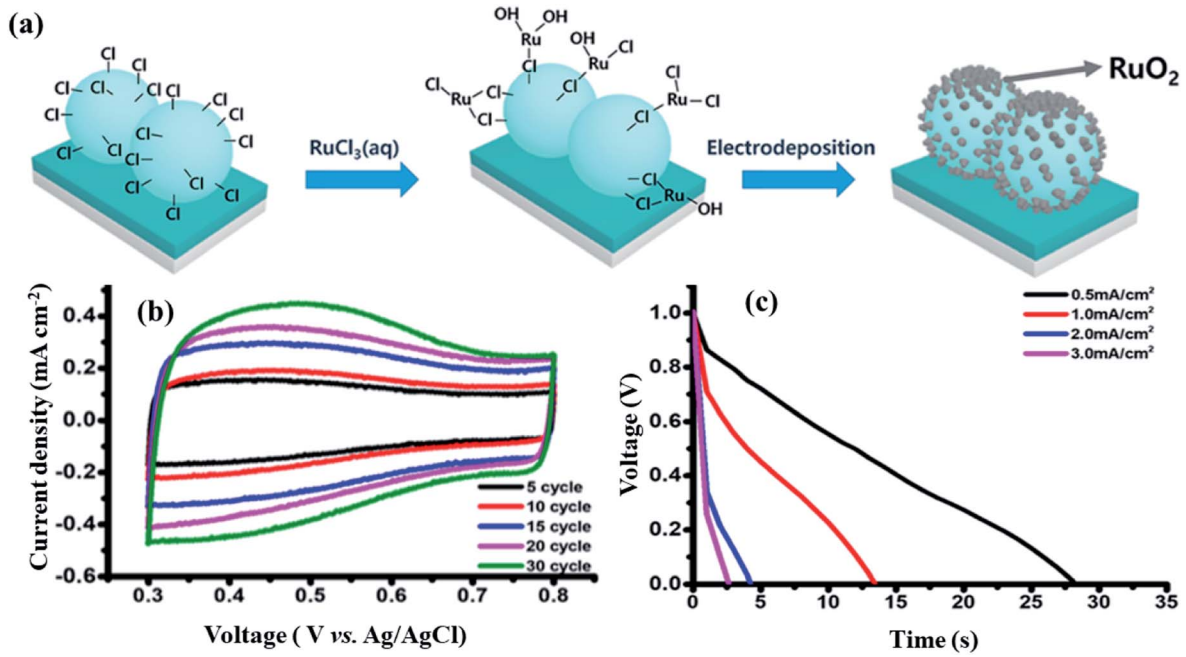

Fig. 4 (a) Schematic display for the fabrication process of the PS/RuO_2 nanospheres on ITO-coated glass substrate, indicating the development of Ru–Cl bonds on the Cl-functionalized PS surface prior to the electrodeposition of RuO_2. (b) CV profiles of PS/RuO_2 nanospheres in three-electrode cell assembly and (c) GCD profiles of PS/RuO_2 nanospheres in two-electrode cell (symmetric) assembly. Figure reproduced from ref. 64 with permission Copyright (2018) from American Chemical Society.

in the composite. The composite material showed only 10% capacitance loss after 1000 cycles at a scan rate of 2 mV s^{-1}. Moreover, the constant current (@100 mA cm^{-2}) and constant power (@4000 W kg^{-1}) discharge tests delivered a specific capacitance and energy density of 344 F g^{-1} and 17.6 W h kg^{-1}, respectively. In 2018, Hong and Yim[64] prepared 2D polystyrene (PS)/RuO_2 core/shell nanospheres *via* the electrodeposition of RuO_2 nanoparticles on a hexagonal close-packed PS monolayer. The hexagonal close-packed PS monolayer, which was prepared using PS nanospheres with chlorinated surface, was positioned on an indium tin oxide (ITO)-coated glass substrate using a scooping transfer technique,[65] and then placed in ruthenium chloride hydrate ($RuCl_3 \cdot xH_2O$) aqueous solution prior to electrodeposition (Fig. 4(a)). The overall reaction for the electrodeposition of RuO_2 from the $RuCl_3$ precursor is depicted below.

$$Ru^{3+} + 4OH^- \rightarrow RuO_2 \cdot 2H_2O + e^- \quad (20)$$

The specific capacitance of the PS/RuO_2 composite was found to be 65.9 mF cm^{-2} at 10 mV s^{-1} in the voltage range of 0.3–0.8 V *vs.* Ag/AgCl in 0.5 M H_2SO_4 medium, while pristine RuO_2 showed 33.7 mF cm^{-2}. Furthermore, a symmetric full cell based on the PS/RuO_2 composite was assembled and tested through GCD and cycling stability. The specific capacitance was observed to be 14.1 mF cm^{-2} (*i.e.*, 258 F g^{-1}) at 0.5 mA cm^{-2} within an operating window of 0–1 V, while the corresponding energy density was determined to be 35.8 W h kg^{-1}. Moreover, the full cell device showed 84.3% capacitance retention after 500 cycles at a current density of 1 mA cm^{-2}. Fig. 4(b and c) demonstrate the CV and GCD profiles of the PS/RuO_2 composite in three-electrode and two-electrode cell (symmetric) assemblies, respectively. However, the high cost and toxic nature of RuO_2 restrict the commercial viability of RuO_2-based supercapacitors, even though these supercapacitors show a high energy density together with an appreciable power density and durability.

4.1.2. Manganese oxides and composites. Low toxicity, low cost and high pseudocapacitance are the attractive features of manganese oxides for supercapacitive applications, where their pseudocapacitance is attributed to the redox transitions between Mn^{3+}/Mn^{2+}, Mn^{4+}/Mn^{3+} and Mn^{6+}/Mn^{4+}.[66] Among the various manganese oxides, such as MnO, Mn_2O_3, Mn_3O_4, MnO_2, and MnO_x, the most used candidate is MnO_2 (having α, β, γ, δ and λ-type polymorphs) due to its high theoretical specific capacitance (>1000 F g^{-1}) for the Mn^{4+}/Mn^{3+} couple. The journey of MnO_2-based supercapacitors started from the pioneering work of Lee and Goodenough (1999).[67] In this first report, the authors demonstrated the pseudocapacitive behaviours of amorphous $MnO_2 \cdot nH_2O$ in 2 M KCl (aq.) electrolyte in the voltage range of −0.2 and 1.0 V *vs.* SCE. The specific capacitance achieved was 203 F g^{-1} at 2 mA cm^{-2}, which was maintained for up to 100 charge/discharge cycles. Unlike RuO_2, mild aqueous electrolyte, such as KCl, Na_2SO_4, K_2SO_4, Li_2SO_4, and KNO_3 are commonly employed in MnO_2-based supercapacitors.[68] The detail pseudocapacitive mechanisms of MnO_2 have been elucidated from *in situ* and *ex situ* spectroscopic, morphological and diffraction studies in specific electrochemical conditions, but briefly, a summary of the different mechanisms can be described as follows:

$$(MnO_2)_{surface} + A^+ + e^- \leftrightarrow (MnO_2{-}A^+)_{surface}\ (A^+: Li^+, Na^+, K^+)^{67} \quad (21)$$

$$MnO_2 + H^+ + e^- \leftrightarrow MnOOH^{69} \quad (22)$$

$$MnO_2 + A^+ + e^- \leftrightarrow MnOOA\ (A^+: Li^+, Na^+, K^+)^{70} \quad (23)$$

In general, the thick films of MnO_2 encounter poor electrical conductivity and slow electrolyte diffusion, and thus provide specific capacitances in lower ranges, *i.e.*, 125 to 250 F g^{-1}.[68] By contrast, Broughton and Brett[71] (2004) reported the specific capacitance of 700 F g^{-1} at 160 μA cm^{-2} in the voltage range of 0–0.9 V *vs.* Ag/AgCl in 1 M Na_2SO_4 electrolyte for an MnO_2 thin film (loading: ~75 μg cm^{-2}), which was synthesized *via* anodic oxidation. Recently, Zhu *et al.*[72] developed a β-MnO_2/birnessite core–shell structure (surface area: 64 m^2 g^{-1}), where the exposed crystal faces of β-MnO_2 were cores and ultrathin (~5 nm), highly ordered birnessite sheets grown on the surface of β-MnO_2 nanorods. The ultrathin birnessite sheets were grown parallel to the *c*-axis of the β-MnO_2 nanorods and formed fin-like nanostructures, which enhanced the effective contacts between the active material and the electrolyte. 2D birnessite can be envisaged for electrochemical energy storage due to the presence of an Mn^{4+}/Mn^{3+} redox pair and open interlayer channels for effective ion diffusion; however, its poor electrical conductivity limits the utilization of the bulk MnO_6 unit. Nevertheless, in the β-MnO_2/birnessite core–shell nanostructure, birnessite is situated in the shell region and enjoys the maximum active material utilization, which is not trivial for bulk materials. The nanocomposite exhibited a specific capacitance of 306 F g^{-1} (with 92% coulombic efficiency) based on the total mass of β-MnO_2/birnessite and 657 F g^{-1} based on the birnessite mass in 1 M Na_2SO_4 (aq.) electrolyte at 0.25 A g^{-1} and −1 to 0.9 V *vs.* SCE. An asymmetric supercapacitor device was fabricated with the β-MnO_2/birnessite composite as the positive electrode, activated microwave-expanded GO as the negative electrode and 1 M Na_2SO_4 (aq.) as electrolyte. The device exhibited a specific capacitance of 60.2 F g^{-1} (@0.25 A g^{-1}), energy density of 40.4 W h kg^{-1} (@275 W kg^{-1}), power density of 17.6 kW kg^{-1} (@8.1 W h kg^{-1}) and moderate cycling stability (85.7% capacitance retention after 5000 cycles @ 0.5 A g^{-1}) in the voltage range of 0–2.2 V. The feasibility test of this device was conducted *via* the illumination of LEDs and the result was optimistic. Jia and co-workers[73] fabricated a graphene quantum dot (GQD)/MnO_2 heterostructured electrode, which expanded the operating voltage window from 0–1 to 0–1.3 V *vs.* SCE in aqueous medium. In the GQD/MnO_2 heterostructure, GQDs were deposited *in situ* on MnO_2 nanosheets *via* plasma-enhanced chemical vapour deposition (PECVD) through the formation of M–O–C covalent bonds. The heterostructure electrode exhibited a specific capacitance of 1094 F g^{-1} at 5 mV s^{-1} in the voltage range of 0–1 V in 1 M Na_2SO_4 (aq.) electrolyte, while the pristine MnO_2

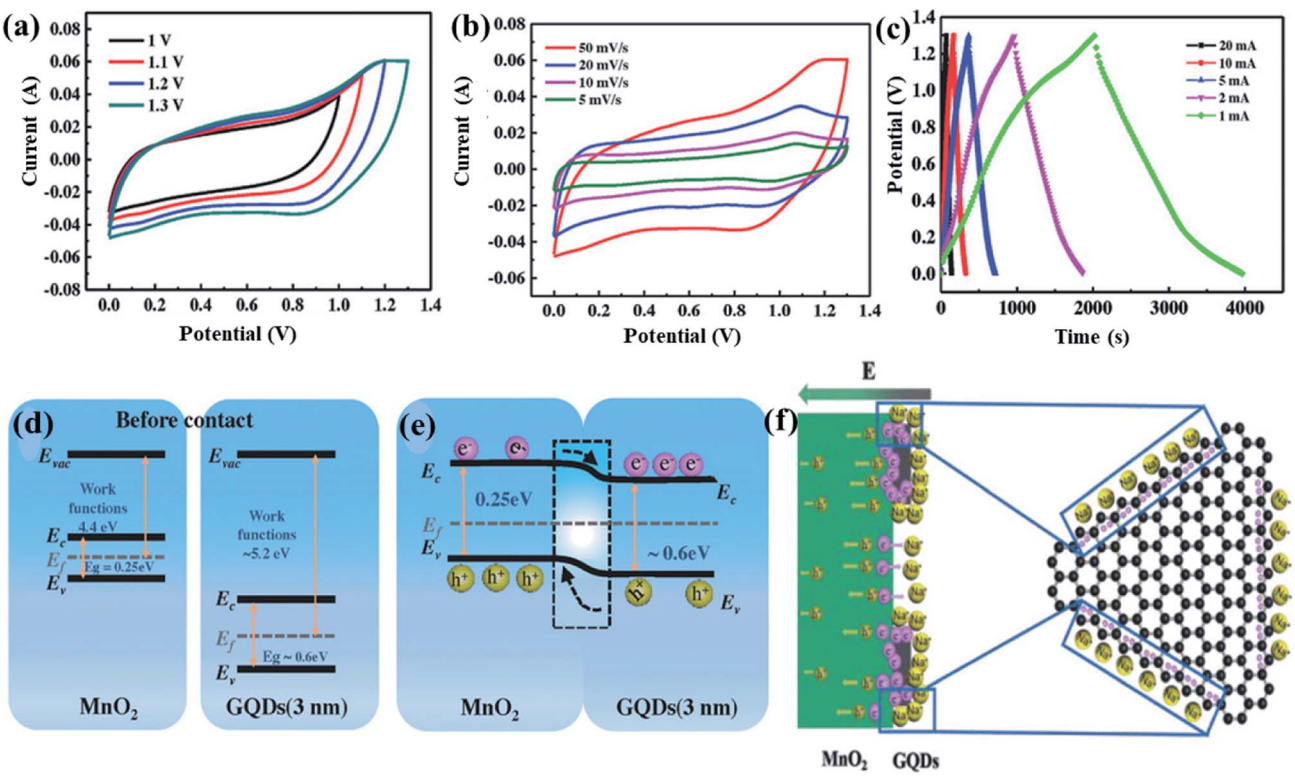

Fig. 5 (a) CV curves of GQDs/MnO_2 composite in different voltage windows of 0–1, 0–1.1, 0–1.2, and 0–1.3 V *vs.* SCE. (b) CV curves of GQDs/MnO_2 composite at different scan rates. (c) GCD curves of the GQDs/MnO_2 composite in 0–1.3 V *vs.* SCE at different currents. (d) Individual energy diagram of MnO_2 and GQDs. (e) Energy diagram of MnO_2 and GQDs at the heterojunction in the GQDs/MnO_2 composite and (f) schematic diagram of the accumulation of free electrons on the surface of the GQDs (specifically near the edge). Figure reproduced from ref. 73.

nanosheet arrays showed only 393 F g^{-1}. Further, the GQD/MnO_2 composite delivered the specific capacitance of 1170 F g^{-1} within 0–1.3 V under similar conditions. The heterostructure electrode retained 92.7% of its initial specific capacitance after 10 000 cycles at a current of 10 mA. Fig. 5(a–c) demonstrate the electrochemical behaviours of the composite electrode in the CV and GCD experiments. An asymmetric device was assembled, comprising the GQD/MnO_2 composite as the positive electrode, nitrogen-doped graphene as the negative electrode and 1 M Na_2SO_4 (aq.) as the electrolyte. The device showed a specific capacitance of 160.6 F g^{-1} (@5 mV s^{-1}), energy density of 118 W h kg^{-1} (@923 W kg^{-1}) and power density of 12 351 W kg^{-1} (@79 W h kg^{-1}) in the voltage range of 0–2.3 V. To comprehend the effects of GQDs on the capacitance improvement and potential enhancement, the authors proposed a schematic energy band diagram, as shown in Fig. 5. The band-gaps of the GQDs and MnO_2 nanosheets were calculated to be 0.6 and 0.25 eV, respectively, which are inversely dependent on the particle size (Fig. 5(d)). Typically, in the GQD/MnO_2 heterostructure, an electric field is generated because of their different work-functions (GQDs: 5.2 eV and MnO_2: 4.4 eV), and hence, the free electrons will transfer from MnO_2 to the GQDs at the interface until the Fermi levels are aligned (Fig. 5(e)). Therefore, the accumulated free electrons on the surface of the GQDs (especially the near edges, shown in Fig. 5(f)) create additional electrostatic attractions with electrolyte ions, which improve the specific capacitances of the heterostructures. The bending of the valence and conduction bands of the GQDs and MnO_2 at the interface of the heterostructure generates a potential gradient,[74] which counteracts the external electric fields and broadens the potential window for supercapacitors.

Another promising and industrially scalable route for enhancing the electrochemical performance of MnO_2-based electrodes is the tuning of Mn point defects and the ratios of Mn^{3+}/Mn^{4+}. In the mid-1980s, P. Ruetschi first developed a comprehensive scheme to correlate cation vacancies with charge storage characteristics for intergrowth MnO_2 phases.[75–77] It was observed that the cation vacancies reduced the activation energy barrier for proton transport through the lattice, which improved the thermodynamic activity of the materials. In reality, cation vacancies are inherently present in all MnO_2 solids, which are synthesized in the aqueous phase either *via* chemical oxidation–precipitation or electrolysis. Gao *et al.*[78] analysed the supercapacitive performances of three different δ-MnO_2 nanosheet samples, namely protonated MnO_2 (H_xMnO_2, surface area: 4.5 m^2 g^{-1}), reassembled MnO_2-pH 2 (surface area: 120 m^2 g^{-1}) and reassembled MnO_2-pH 4 (surface area: 144 m^2 g^{-1}), with varying Mn vacancies and average oxidation states of Mn. The reassembled MnO_2-pH 2 and reassembled MnO_2-pH 4 samples were produced by equilibration at pH 2 and pH 4, respectively, for the intentional introduction of Mn vacancies into the nanosheets. The X-ray absorption near edge structure (XANES) spectra provided the average oxidation state of Mn in the three samples, which was determined to be 3.57, 3.24 and 3.36 in the protonated MnO_2, reassembled MnO_2-pH 2 and reassembled MnO_2-pH 4, respectively (Fig. 6(a–d)). Consequently, the corresponding content of Mn vacancies was elucidated to be 18.3%, 26.5% and 19.9%, while, the respective ratios of Mn^{3+}/Mn^{4+} were detected as 41 : 59, 76 : 24 and 64 : 36, respectively. It was observed that an improved specific capacitance and lower charge transfer resistance were achieved when the content of Mn vacancies was higher (Fig. 6(e–g)). Moreover, following the same trend, the reassembled MnO_2-pH 2 sample showed superior durability compared to the reassembled MnO_2-pH 4, as shown in Fig. 6(h).

Besides MnO_2, Mn_2O_3 (ref. 79) and Mn_3O_4 (ref. 80) have also been reported for supercapacitor applications. Li *et al.*[79] synthesized crystalline porous Mn_2O_3 nanocubes (surface area: 54.5 m^2 g^{-1} and average pore size: 12.4 nm) *via* a facile hydrothermal method followed by calcination, which exhibited a specific capacitance of 191.1 F g^{-1} at 100 mA g^{-1} in the voltage range of 0–0.8 V *vs.* SCE in 0.5 M Na_2SO_4 (aq.) electrolyte. The symmetric full cell showed a specific capacitance of 53.2 F g^{-1} (@5 mV s^{-1}) and good cycling performance (92.1% capacitance retention over 3000 cycles @ 50 mV s^{-1}) in the voltage range of 0–1.2 V window. Mn_3O_4 nanodots loaded on nitrogen-doped graphene sheets (Mn_3O_4 NDs@NG) were synthesized by Liu and co-workers[80] through a one-pot solvothermal method in the presence of octylamine as a surfactant. The composite material demonstrated a specific capacitance of 158.9 F g^{-1} at 0.5 A g^{-1} in the voltage range of −1.6 to 0.4 V *vs.* Ag/AgCl in 1-ethyl-3-methylimidazolium tetrafluoroborate ($EMIMBF_4$) IL electrolyte at room temperature. An asymmetric device was assembled with activated polyaniline-derived carbon as the positive electrode, Mn_3O_4 NDs@NG as the negative electrode and ($EMIMBF_4$) as the electrolyte. This asymmetric device delivered a specific capacitance of 56 F g^{-1} (@0.5 A g^{-1}), energy density of 124.4 W h kg^{-1} (@999.3 W kg^{-1}) and power density of 29.9 kW kg^{-1} (@55.8 W h kg^{-1}) in the voltage range of 0–4 V window. A poor cycling performance (57.9% capacitance retention @ 2 A g^{-1} over 10 000 cycles) is observed in the voltage window of 0–4 V, while the capacitance retention values reached at 68.4% and 78.9% for that of 0–3.8 V and 0–3.5 V, respectively.

On a different note, Mn^{3+} species spontaneously disproportionate (eqn (24)) into Mn^{2+} species and MnO_2, while soluble Mn^{2+} species dissolve in the electrolyte and insoluble MnO_2 remains in the electrode.[81]

$$2Mn^{3+} + 2H_2O \rightarrow Mn^{2+} + MnO_2 + 4H^+ \quad (24)$$

The experimental evidence indicates that this disproportion reaction is greatly catalyzed in acidic media.[81,82] This parasitic reaction reduces the cycling stability of supercapacitors due to the structural disintegration of manganese oxide-based positive active materials. Moreover, the adverse effects of the cross-communication of soluble Mn-species on the negative electrode cannot be ignored.[83] However, to prevent the dissolution of Mn, different chemical measures such as elemental doping[81] and surface coating[84] are extensively carried out on manganese oxides. Notably, most transition metal-based electrodes undergo structural degradation by metal ion dissolution *via* acid leaching in acidic media; however the extent of Mn dissolution is truly high.[85] Therefore, discarding acidic electrolytes

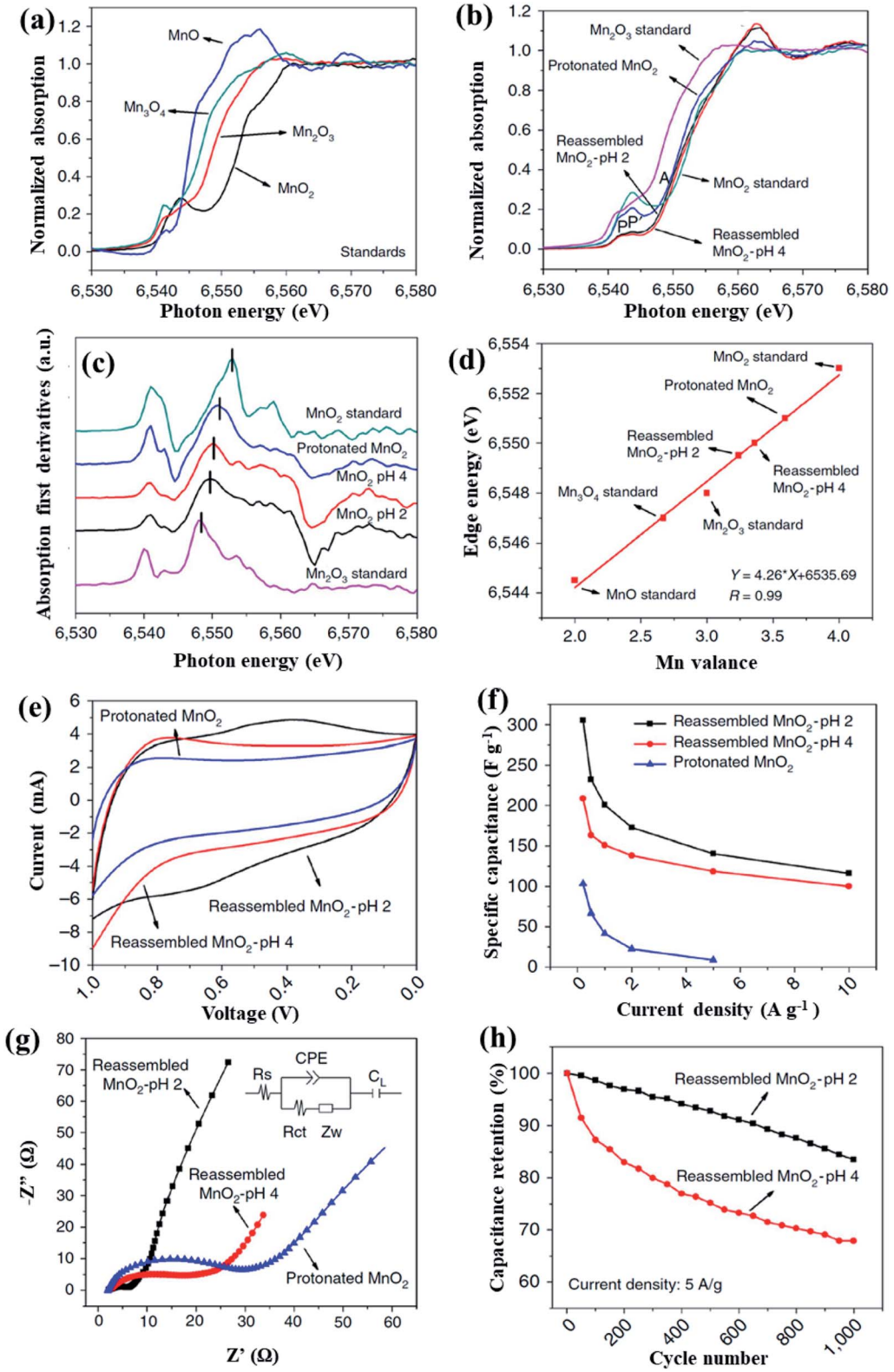

Fig. 6 (a) XANES spectra of MnO, Mn_3O_4, Mn_2O_3 and MnO_2 as reference materials. (b) XANES spectra of protonated MnO_2, reassembled MnO_2-pH 2 and reassembled MnO_2-pH 4 together with Mn_2O_3 and MnO_2 as reference materials. (c) First derivative profiles corresponding to the samples shown in (b). (d) Average oxidation state of Mn for the mentioned samples derived from the K-edge energy. (e) CV analysis in 1 M Na_2SO_4 (aq.) electrolyte for the mentioned samples at 50 mV s^{-1} ion a three-electrode cell assembly with Ag/AgCl as the reference electrode. (f) Comparison of the specific capacitance (0–1 V *vs.* Ag/AgCl) for the mentioned samples as a function of current density. (g) Nyquist plots of the mentioned samples within 0.1 Hz to 100 kHz at an open circuit potential of 5 mV (inset shows the electrical equivalent circuit used for fitting the impedance spectra) and (h) durability test under 0–1 V *vs.* Ag/AgCl voltage regime. Figure reproduced from ref. 78.

(adverse effects: acid leaching and accelerating Mn^{3+} disproportionation) and applying neutral electrolytes are preferable for manganese oxide-based energy storage devices.

4.1.3. Iron oxides and composites. Iron oxides including Fe_2O_3, Fe_3O_4, FeOOH, and Fe_xO_y have been identified as potential supercapacitive materials considering their broad voltage window as negative electrodes, ideal theoretical specific capacitance (Fe_2O_3: >3500 F g^{-1}, Fe_3O_4: >2500 F g^{-1}, and FeOOH: >2500 F g^{-1}),[86] abundant availability, and eco-friendliness. The preliminary evaluations revealed that low electrical conductivity and poor cycling stability restrict the practical applications of iron oxide-based supercapacitors.[87] Nevertheless, nanostructuring and forming various composites with conductive matrices can mitigate the abovementioned limitations. Among the various iron oxides, Fe_2O_3 has attracted considerable interest. Four different crystal structures, namely, α-Fe_2O_3, β-Fe_2O_3, γ-Fe_2O_3, and ε-Fe_2O_3, are available for Fe_2O_3, where α-Fe_2O_3 is the most thermodynamically stable phase.[88] Through an electrochemical and successive ionic layer adsorption and reaction method, Gund *et al.*[89] synthesized Fe_2O_3 nanoparticle thin films on a flexible stainless steel (SS) substrate. The flexible asymmetric supercapacitor was assembled with the (+)MnO_2//1 M Na_2SO_4–carboxymethyl cellulose (CMC) gel//Fe_2O_3(−) configuration, which exhibited a specific capacitance of 75 F g^{-1} (@1.28 A g^{-1}), energy density of 41.8 W h kg^{-1} (@1276 W kg^{-1}), power density of 5102 W kg^{-1} (@19.4 W h kg^{-1}) and good cycling performance (91% capacitance retention over 3000 scans @ 100 mV s^{-1}) in the operating window of 0–2 V. The EIS test was carried out in the frequency range of 100 MHz to 100 kHz, where the solution resistance (R_s) and charge-transfer resistance (R_{ct}) were calculated to be 0.64 and 28.95 Ω cm^{-2}, respectively. The lower resistive components together with the 70° inclined straight line at lower frequencies indicate good capacitive properties. Guan and co-workers[90] designed a graphite foam (GF)–CNT framework with a surface coating of a thin layer of Fe_2O_3 (GF–CNT@Fe_2O_3). According to the illustration shown in Fig. 7, vertically aligned CNTs were grown on the GF through the chemical vapour deposition (CVD) method, and afterwards, a crystalline Fe_2O_3 layer was deposited on the GF–CNT framework *via* atomic layer deposition (ALD). GF–CNT@Fe_2O_3 showed the areal capacitance of ∼470.5 mF cm^{-2} at 20 mA cm^{-2} in the voltage range of 0 to −1.2 V *vs.* SCE in 2 M KOH electrolyte, which is about 4 times higher than that of the GF–CNT framework (∼93.8 mF cm^{-2}). A two-electrode full cell, namely, (+)GF–$CoMoO_4$//2 M KOH//GF–CNT@Fe_2O_3(−), was constructed, which delivered a specific capacitance of 210 F g^{-1} (@1.75 A g^{-1}), energy density of 74.7 W h kg^{-1} (@1.4 kW kg^{-1}), power density of 11.2 kW kg^{-1} (41.1 W h kg^{-1}) and excellent cycle life (95.4% capacitance retention after 50 000 cycles @ 7 A g^{-1}) in the window of 0–1.6 V. Li *et al.*[91] synthesized Fe_3O_4 nanosheet arrays uniformly grown on nickel foam (NF) using the $Fe(NO_3)_3 \cdot 9H_2O$ precursor by annealing at 350 °C for 2 h. The specific capacitance of the as-synthesized electrode (Fe_3O_4–NF) was observed to be 379.8 F g^{-1} at 2 A g^{-1} in the voltage range of −1 to 0 V *vs.* SCE in 2 M KOH electrolyte. The asymmetric device (+)NF–Co_2AlO_4@MnO_2//PVA–KOH//NF–Fe_3O_4(−) delivered a specific capacitance of 99.13 F g^{-1} (@2 A g^{-1}), energy density of 35.25 W h kg^{-1} (@800.1 W kg^{-1}), power density of 8033 W kg^{-1} (@24.11 W h kg^{-1}) and good cycling performance (92.4% capacitance retention after 5000 cycles @ 5 A g^{-1}) in the window of 1–1.6 V window. A supercapacitor bank with two series connected devices illuminated a green LED (1.8 V) for 120 s after being charged for 10.8 s. Kumar and co-workers[92] developed an Fe_3O_4-composite (3D Fe_3O_4/rGO) *via* a one-pot microwave approach, where the Fe_3O_4 nanoparticles (50–200 nm) were entrapped and well-dispersed in the interconnected rGO network (2630 m^2 g^{-1}). The 3D Fe_3O_4/rGO composite electrode showed a specific capacitance of 455 F g^{-1} (@3.6 A g^{-1}), energy density of 124 W h kg^{-1} (@2.06 kW kg^{-1}), power density of 2.74 kW kg^{-1} (@80.9 W h kg^{-1}) and impressive cycling stability (∼8.5% loss after 9500 cycles @ 3.8 A g^{-1}) in the window of −0.4 to 1 V *vs.* Ag/AgCl in 2 M KOH

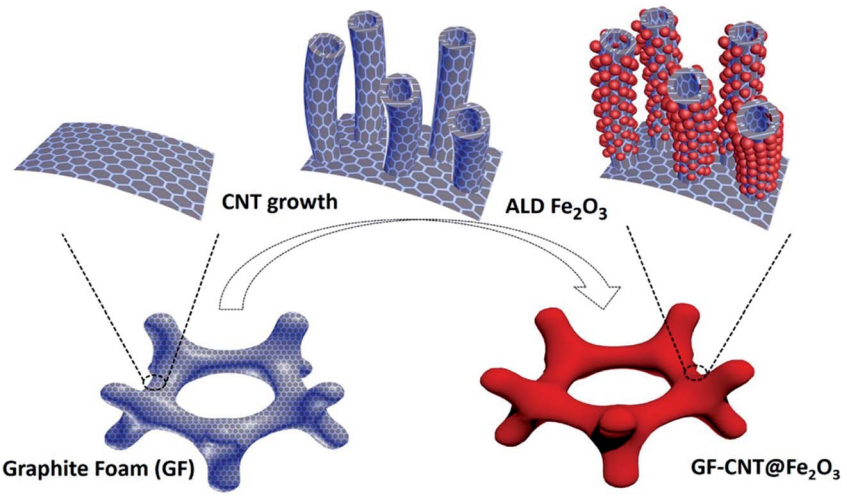

Fig. 7 Schematic illustration of the growth procedure of GF–CNT@Fe_2O_3 from graphite foam. Figure reproduced from ref. 90 with permission Copyright (2015) from the American Chemical Society.

electrolyte. Long *et al.*[93] synthesized an FeOOH/graphene-nanosheet/CNT composite (FeOOH/GNS/CNT) *via* the direct hydrolysis of Fe^{3+} on the surface of GNS-supported and CNT-bridged frameworks. The as-prepared FeOOH/GNS/CNT nanocomposite demonstrated the Li^+ ion intercalation/deintercalation reaction in 1 M Li_2SO_4 (aq.) solution, as follows:

$$FeOOH + xLi^+ + xe^- \leftrightarrow FeOOHLi_x \quad (25)$$

The FeOOH/GNS/CNT composite electrode exhibited a specific capacitance of 267 F g^{-1} at 0.5 A g^{-1} in the window of −0.85 to −0.1 V *vs.* SCE in 1 M Li_2SO_4 medium, which was considerably higher than that of FeOOH/GNS (210 F g^{-1}) and pristine FeOOH (148 F g^{-1}). A two-electrode asymmetric device was assembled as (+)MnO_2/GNS//1 M Li_2SO_4 (aq.)//FeOOH/GNS/CNTs(−), which demonstrated a specific capacitance of 77 F g^{-1} (@0.2 A g^{-1}), energy density of 30.4 W h kg^{-1} (@237.6 W kg^{-1}), power density of 8600 W kg^{-1} (@7.4 W h kg^{-1}) and good cycling stability (89% capacitance retention 1000 cycles @ 100 mV s^{-1}) in the voltage range of 0–1.7 V. Liu and co-workers[94] reported a nitrogen-doped graphene/FeO_x hybrid electrode with a 3D nanoporous architecture (NP NDG/FeO_x), which exhibited a low internal resistance (5.4 Ω) and high specific capacity (∼409 mA h g^{-1} @ 5 mV s^{-1} in the voltage range of −1.2 V to 0 V *vs.* SCE in 1 M KOH). An asymmetric device was assembled with the (+)$Ni(OH)_2$//1 M KOH//NP NDG/FeO_x(−) configuration, which exhibited a specific capacity of 187 mA h g^{-1} (@5 mV s^{-1}), energy density of 142 W h kg^{-1} (@1.4 kW kg^{-1}), power density of 23 kW kg^{-1} (@53 W h kg^{-1}) and good cycling stability (91% capacity retention after 10 000 cycles @ 9 A g^{-1}) in the voltage range of 0–1.7 V.

4.1.4. Nickel oxide and composites. NiO is well studied for supercapacitor electrodes due to its good theoretical capacitance (2584 F g^{-1} @ 0.5 V potential window),[95] impressive reversible redox reactions (Ni^{2+}/Ni^{3+}) and easy availability. The surface faradaic reaction of NiO in alkaline electrolyte is as follows:[96]

$$NiO + OH^- \leftrightarrow NiOOH + e^- \quad (26)$$

According to a different theory, initially, NiO is converted to $Ni(OH)_2$ in alkaline medium, and then redox reactions occur between $Ni(OH)_2$ and NiOOH as follows:[95]

$$Ni(OH)_2 + OH^- \leftrightarrow NiOOH + H_2O + e^- \quad (27)$$

However, both theories arrive at the consensus that Ni^{2+} is oxidized to NiOOH, which is responsible for supercapacitive charge storage. In reality, a high theoretical capacitance has not been achieved because of its poor conductivity (0.01–0.32 S m^{-1}),[97] and simultaneously, poor durability is observed due to the excessive volume change upon charge/discharge. Nevertheless, some modifications of the active materials may improve the experimental specific capacitance and cycling stability,[98] such as, preparing composites with conductive matrices, nanostructuring and developing suitable morphologies to buffer the internal strain. Wu and co-workers[99] anodically electrodeposited NiO nanoflakes using a polystyrene sphere monolayer as a template. The resulting NiO films consisted of interconnected nanoflakes (thickness: 12–16 nm) with open macropores (diameter: 200 nm), where the macropores were generated from the removal of the polystyrene sphere template. The resulting macropores facilitated fast electrolyte infiltration and enhanced the electrochemical performances by maximizing the active material utilization. The specific capacitance of the NiO film with macropores was found to be 351 F g^{-1} at 10 mV s^{-1} in the voltage range of 0–0.45 V *vs.* Ag/AgCl in 1 M KOH, while under the same conditions, the NiO film without micropores exhibited only 140 F g^{-1}. This study clearly indicates the necessity of electrode modification for achieving considerable supercapacitive performances. Liu *et al.*[100] synthesized a hierarchical NiO/C hollow sphere composite (NiO/C-HS) *via* semi-sacrificial template-assisted hydrothermal and calcination methods, where well-dispersed NiO nanosheets were supported by carbon hollow spheres. The NiO/C-HS electrode exhibited a specific capacitance of 686 F g^{-1} at 1 A g^{-1} in the voltage range of 0–0.45 V *vs.* Ag/AgCl in 2 M KOH electrolyte, which is much greater than that of the NiO-HS electrode (182 F g^{-1}). A (+)NiO/C-HS//2 M KOH//AC(−) device was assembled, which delivered a specific capacitance of 99 F g^{-1} (@0.25 A g^{-1}) and energy density of 30.5 W h kg^{-1} (@193 W kg^{-1}) in the voltage range of 0–1.5 V. In the durability test, the (+)NiO/C-HS//AC(−) device maintained 100% of its initial capacitance at 1 A g^{-1} after 5000 cycles, while 83% capacitance retention was observed in NiO-HS//AC under similar working conditions. The improved performances of NiO/C-HS are attributed to: (i) synergistic effect between the conductive C-HS and NiO nanosheets; (ii) the formation of an integrated composite, which affords buffer space to accommodate volume changes; (iii) direct growth of NiO nanosheets on C-HS, which minimizes the aggregation of the NiO nanosheets; (iv) nanostructuring provides a high surface area and facile electrolyte diffusion; and (v) additional EDL contribution for C-HS. Chen and co-workers[101] prepared a graphene/NiO (G/NiO) composite *via* hydrothermal synthesis from an aqueous mixture of graphene and $Ni(NO_3)_2$ followed by microwave irradiation of the hydrothermally synthesized product. Scanning electron microscopy (SEM) and transmission electron microscopy (TEM) depicted that 20–50 nm-sized NiO particles were homogeneously distributed on the graphene substrate. The two-electrode symmetric button cell with the G/NiO composite exhibited the specific capacitance of 617 F g^{-1} at 1 A g^{-1} in the voltage range of 0–0.8 V in 5 M NaOH electrolyte, while the pristine graphene-based cell showed only 265 F g^{-1}. Since the larger space between the adjacent graphene sheets provided a buffer for volume changes in the NiO particles, the G/NiO composite material showed excellent cycling stability (99.4% capacitance retention @ 1 A g^{-1} for 5000 cycles).

4.1.5. Cobalt oxides and composites. Cobalt oxides have received considerable interest in supercapacitor applications due to their high theoretical capacitances (CoO: >4000 F g^{-1} and Co_3O_4: >3500 F g^{-1}),[102,103] easy synthesis, and environmentally friendly nature. Similar to NiO, cobalt oxides are nonconducting in nature and encounter excessive volume changes during repetitive charge/discharge processes. Various

morphological modifications and the preparation of composites with conductive matrices have been extensively carried out to achieve good supercapacitive performances. Porous Co_3O_4 nanocubes (Co_3O_4 NCs, surface area: 61.5 $m^2\ g^{-1}$ and average particle size: 50–60 nm) were synthesized by Jang *et al.*[104] *via* simple and cost-effective hydrothermal method. The CV curves of the Co_3O_4 NCs in 6 M KOH medium showed two pairs of redox peaks in the voltage range of −0.4 to 1 V *vs.* Ag/AgCl, which indicate the following pseudocapacitive reactions.

$$Co_3O_4 + OH^- + H_2O \leftrightarrow 3CoOOH + e^- \quad (28)$$

$$CoOOH + OH^- \leftrightarrow CoO_2 + H_2O + e^- \quad (29)$$

The specific capacitance of the Co_3O_4 NCs electrode was found to be 430.6 F g^{-1} at 10 mV s^{-1}, and it retained 85% of this value after 1000 charge/discharge cycles. Liu and co-workers[105] developed Co_3O_4/nitrogen-doped hollow carbon spheres (Co_3O_4/NHCSs) with hierarchical structures *via* the hydrothermal method and subsequent calcination treatment, where the NHCSs act as a hard template to generate Co_3O_4 nanosheets on their surface. Co_3O_4/NHCSs showed a specific capacitance of 581 F g^{-1} at 1 A g^{-1} in the voltage range of 0–0.45 V *vs.* Ag/AgCl in 2 M KOH, which was higher than that of the pristine Co_3O_4 nanorods (NRs) (318 F g^{-1}). An asymmetric device (+)Co_3O_4/NHCSs//2 M KOH//AC(−) was assembled, which demonstrated a specific capacitance of 111 F g^{-1} (@1 A g^{-1}), energy density of 34.5 W h kg^{-1} (@753 W kg^{-1}) and power density of 3807 W kg^{-1} (@29.0 W h kg^{-1}) in the voltage window of 0–1.5 V. Moreover, the device displayed 100% capacitance retention at 5 A g^{-1} after 5000 cycles, while under similar circumstances (+)Co_3O_4-NRs// 2 M KOH//AC(−) exhibited only 78% capacitance retention. The Co_3O_4/NHCS-based device achieved excellent durability due to the presence of highly conductive NHCSs, which inhibited the agglomeration and degradation of Co_3O_4 under recitative cycling. Deng *et al.*[106] synthesized a CoO/graphene foam (CoO/GFs) composite material *via* a hydrothermal process and subsequent thermal treatment, where CoO nanowalls were well dispersed and separated by GFs with robust adhesion. The composite electrode showed a specific capacitance of 139.47 F g^{-1} (*i.e.*, 231.87 F g^{-1} scaled to the mass of CoO) at 1 A g^{-1} in the voltage range of 0–0.6 V *vs.* Hg/HgO in 3 M NaOH and retained 98% of its initial capacitance after 1000 cycles at 7 A g^{-1}. Sun and co-workers[107] developed a 1.8 V asymmetric supercapacitor based on an ultrathin carbon shell-entrapped Co-doped CoO heterostructure (CoO/Co@C) as the positive electrode, AC as the negative electrode and 2 M KOH as the electrolyte. The CoO/Co@C heterostructure (surface area: 38.9 $m^2\ g^{-1}$) exhibited a specific capacitance of 1985.1 F g^{-1} at 2 A g^{-1} in the voltage range of 0–0.6 V *vs.* Ag/AgCl in 2 M KOH. However, the full cell delivered a specific capacitance of 325.2 F g^{-1} (@2 A g^{-1}), energy density of 146.3 W h kg^{-1} (@1800 W kg^{-1}), power density of 27 000 W kg^{-1} (@63.0 W h kg^{-1}) and splendid cycling performance (98.1% capacitance retention after 15 000 cycles @ 30 A g^{-1}) in the voltage range of 0–1.8 V.

4.1.6. Other metal oxides and composites. The above-discussed Ru, Mn, Fe, Ni and Co-based oxides and their composites are widely applied for chemical supercapacitors, but various other metal oxides, such as, ZnO,[108] TiO_2,[109] CuO,[110] SnO_2,[111] MoO_3,[112] CrO_3,[113] PbO,[114] PbO_2,[115] $W_{18}O_{49}$,[116] V_2O_5,[117] Bi_2O_3,[118] In_2O_3,[119] and their composites are also envisaged. Heng *et al.*[120] reported an asymmetric supercapacitor with AC as the positive electrode and TiO_2 nanoparticles as the negative electrode in 1 M KOH electrolyte. The asymmetric device delivered a specific capacitance of 121 F g^{-1} (@0.4 A g^{-1}), energy density of 35.38 W h kg^{-1} (@408.23 W kg^{-1}) and moderate cycle life (80.4% capacitance retention after 3000 cycles @ 0.5 A g^{-1}) in the voltage window of 0–1.45 V. Barik *et al.*[121] developed a (+) AC//PVA/KOH//SnO_2@CNF(−) device, which exhibited a specific capacitance of 2.12 F g^{-1} (@0.2 A g^{-1}), energy density of 4.71 W h kg^{-1} (@3200 W kg^{-1}) and good cycling performance (92% capacitance retention after 2000 cycles @ 0.2 A g^{-1}) in the voltage range of 0–2 V. Karade *et al.*[122] constructed a symmetric device with the (+)V_2O_5//1 M $LiClO_4$ (aq.)//V_2O_5(−) configuration, which showed a specific capacitance of 172 F g^{-1} (@1.9 A g^{-1}), energy density of 23.9 W h kg^{-1} (@937 W kg^{-1}), power density of 6250 W kg^{-1} (@17 W h kg^{-1}) and excellent cycling stability (94.3% capacitance retention after 10 000 cycles @ 3.1 A g^{-1}) in the voltage window of 0–1 V. Banerjee *et al.*[115,123–125] designed and developed hybrid supercapacitors (rated energy density: ∼2 W h kg^{-1} and rated power density: ∼1000 W kg^{-1} based on device mass) by assembling a battery (lead-acid)-type PbO_2 positive electrode and supercapacitor-type AC negative electrode in 6 M H_2SO_4–silica gel electrolyte. In this study, Planté-type substrate integrated thin film PbO_2 electrodes (∼300 μm) were used instead of a commercial grade-thick pasted-type positive electrode (∼1 mm) for improving power capability.[126] The stand-alone energy systems were designed with 12 V prototype devices (100–250 F range) and required power-electronics[127] for real-life applications, for example, powering 30 W portable medical gadgets (electrocardiogram machine)[128] and solar energy storage.[129] To characterize the device performance under a solar charging schedule, a year-round test was designed with charging in the day (9 am to 6 pm) through a 10 W_p photovoltaic panel and discharging at night (6 pm onwards) through a 1 W LED.[129] It was observed that the monthly average for the charging energy input (kJ) data was well synchronized with the average solar insolation (kW h m^{-2}) data for the respective month (Fig. 8(a)). Further, Fig. 8(b and c) depict the profiles of supercapacitor charging power (W) and solar insolation (W m^{-2}) as a function of real time (Indian Standard Time) for one cloudy and one sunny representative day, respectively. It is apparent that the charging profile for the supercapacitor followed the trend of the solar insolation profile pretty accurately when the solar insolation was limited (in a cloudy day). In the case of a sunny day, the device charging phenomenon was completed, and became saturated. These experimental findings indicate the efficient charging characteristics of the hybrid device due to its excellent power capability. In the year-round test, the device did not show any performance degradation, which was established by the undiminished discharge time (except seasonal variation) of the device for a 1 W LED load (Fig. 8(d)). Among the ocean of supercapacitors, limited systems attain the level of

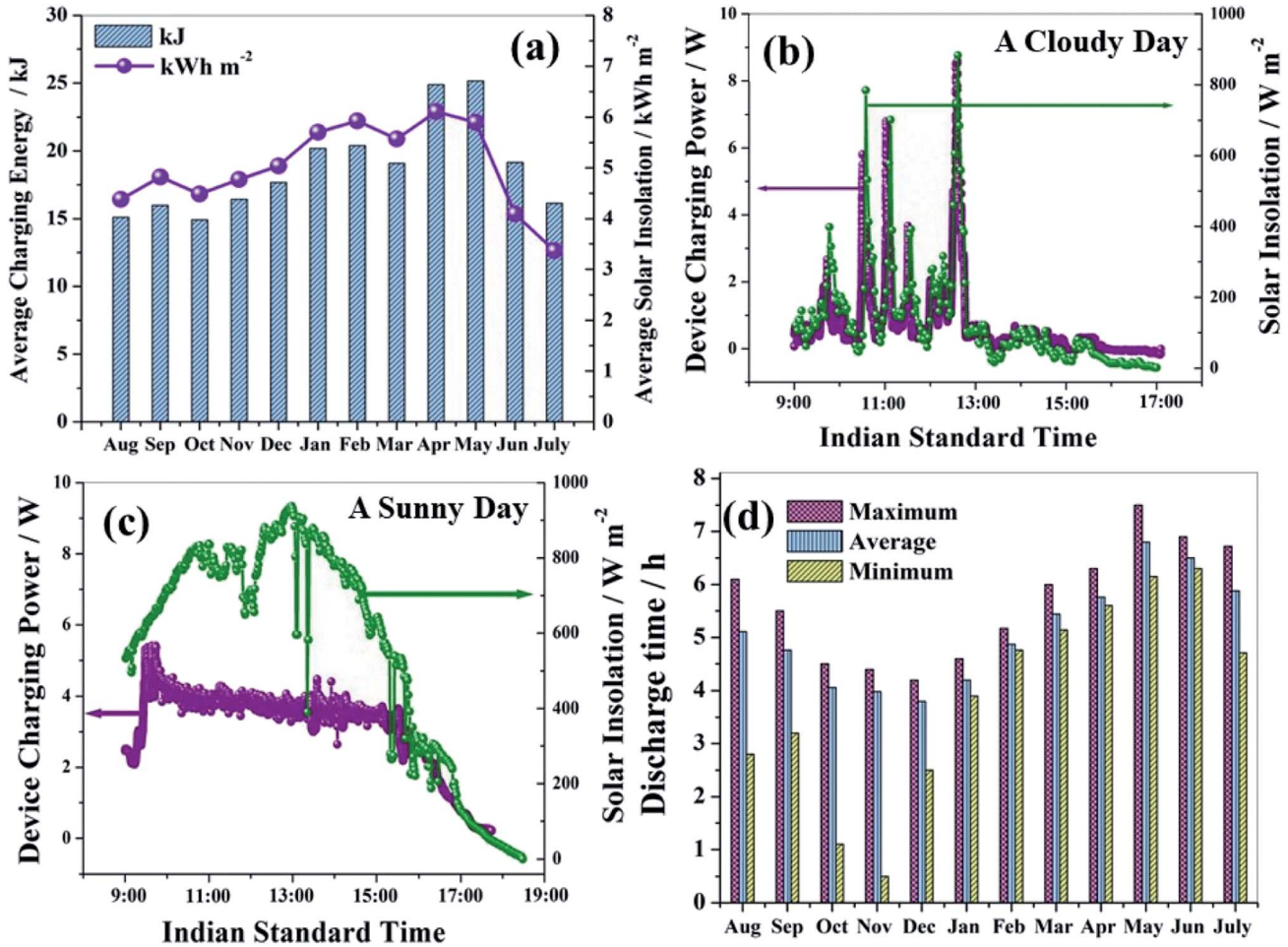

Fig. 8 (a) Monthly distribution of average charging energy (input) of the supercapacitor with respect to solar insolation. (b and c) Synchronization of charging power with solar insolation as a function of real time and (d) monthly analysis for discharge time under 1 W LED load. Figure reproduced from ref. 129.

commercialization, where the (+)PbO_2//6 M H_2SO_4–silica gel//AC(−) system is one of them.

4.1.7. Mixed metal oxides and their composites. Most metal oxides are either insulating or semiconducting, and hence, pristine monometallic oxides are not suitable active materials for advanced supercapacitors. On the one hand, the morphological evolutions, nanostructuring and composite formations are elaborated in the previous sections with different representative examples. On the other hand, the mixed metallic oxides are truly promising for enhanced specific capacitance due to the synergistic effect of multiple redox active metallic sites. This synergistic effect[18,130] includes (i) better charge storage capability due to improved utilization of electroactive materials; (ii) superior structural integrity, and consequently, the retention of crystal phases during repetitive charge/discharge cycles; and (iii) enhanced electrical conductivity, and concomitant faster electron transport. Li *et al.*[131] synthesized an Fe_3O_4@TiO_2 core–shell nanorod array through uniform ALD-TiO_2 coating on an Fe_3O_4 electrode, where the TiO_2 shell is not only buffered the inner volume change of Fe_3O_4, but also provided additional capacitance through the surface intercalation/deintercalation of Li^+ ions in 1 M Li_2SO_4 (aq.) electrolyte and helped to alleviate the water splitting potential. The Fe_3O_4@TiO_2 composite electrode showed superior cycling stability compared to the pristine Fe_3O_4 electrode, such as 405.6% capacity retention (initial capacity improved through activation) was observed for former, while the latter exhibited only 49.4% retention at 50 mV s^{-1} after 30 000 cycles in the voltage range of −1.2 to 0 V *vs.* SCE at 1 M Li_2SO_4 (aq.) electrolyte. A flexible quasi-solid-state hybrid device, namely, (+)V_2O_3@C//PVA–LiCl hydrogel//Fe_3O_4@TiO_2(−) was assembled, which delivered an energy density of 2.23 mW h cm^{-3} (@29 mW cm^{-3}) and power density of 1090 mW cm^{-3} (@0.24 mW h cm^{-3}) in the operating window of 0–2 V. The authors also elucidated the relative contributions of surface-controlled and diffusion-controlled charge storage processes to the total capacity at 100 mV s^{-1}, and reported 66% surface contribution, which is in good accordance with the characteristics of hybrid supercapacitors. Deshmukh *et al.*[132] developed a polygonal structure of $(Fe,Cr)_2O_3$ oxide layer on SS mesh (SS/$(Fe,Cr)_2O_3$) *via* the thermal oxidation of the SS-substrate in ambient atmosphere, which exhibited a specific capacitance of 7 mF cm^{-2} at 0.5 mA

cm^{-2} in the voltage range of −1 to 0 V *vs.* Ag/AgCl in 1 M KOH electrolyte. A flexible symmetric device was assembled with SS/$(Fe,Cr)_2O_3$ electrodes in PVA–KOH gel electrolyte, which demonstrated a specific capacitance of 1.62 mF cm^{-2} (@0.5 mA cm^{-2}), energy density of 0.57 mW h cm^{-2} (@200 mW cm^{-2}) and power density of 400 mW cm^{-2} (@0.42 mW h cm^{-2}) in the voltage window of 0–1.6 V. Moreover, the flexible symmetric device showed 90% capacitance retention over 2000 scans at 100 mV s^{-1} under both bending and twisting modes. Sarma and co-workers[133] prepared an NiO and Co_2O_3-based mixed oxide (Ni–NiO/Co_2O_3) *via* the electrodeposition of Co_2O_3 on an NiO substrate, while NiO was formed on the Ni substrate by air oxidation. The Ni–NiO/Co_2O_3 composite electrode achieved a high specific capacitance of 412 F g^{-1} at 20 mV s^{-1} in the voltage range of 0–0.5 V *vs.* Ag/AgCl in 1 M KOH electrolyte, which was ~20% higher than that of the Ni-foil/Co_2O_3 electrode. The improved performances of the Ni–NiO/Co_2O_3 electrode are mostly due to the synergistic effect of its two oxide phases (NiO and Co_2O_3). Feng *et al.*[134] prepared a 3D hierarchical $MnMoO_4$/$NiWO_4$ microsphere composite (surface area: 37.6 m^2 g^{-1}) electrode *via* a one-pot hydrothermal method, where the composite was composed of self-assembled $MnMoO_4$ nanoflakes and $NiWO_4$ nanoparticles. The CV curves of the $MnMoO_4$/$NiWO_4$ composite showed significant redox peaks in 2 M KOH medium in the potential range of 0–0.4 V *vs.* SCE, which are attributed to the faradaic reactions of the Ni^{2+}/Ni^{3+} and Mn^{2+}/Mn^{3+} couples. The composite electrode achieved a specific capacitance of 598 F g^{-1} at 1 A g^{-1} in the voltage range of 0–0.4 V, and retained 82% of its initial capacitance over 5000 charge/discharge cycles. The 3D hierarchical structures have many open spaces for the penetration of the electrolyte, which enhances their supercapacitive performances by maximizing the active material utilization. Further, 3D hierarchical $MnMoO_4$/$NiWO_4$ microspheres exhibited a robust morphological structure due to the uniform growth of $NiWO_4$ nanoparticles on the $MnMoO_4$ nanosheet backbones. Thus, this sturdy morphology of the composite improved the structural integrity of the electrodes, resulting in superior cycling stability.

4.2. Metal hydroxides and composites

The hydroxides of Ni, Co and Fe together with LDHs are mostly employed in chemical supercapacitors. Hexagonal layer-structured $Ni(OH)_2$ has two polymorphs, namely, α- and β-$Ni(OH)_2$, which oxidise to γ- and β-NiOOH,[135] respectively, and Fig. 9 shows the transformations among the various phases of $Ni(OH)_2$ and NiOOH (Bode diagram). Structurally, α-$Ni(OH)_2$ is a hydroxyl-deficient phase with inter-layered anions and water molecules, while β-$Ni(OH)_2$ has a brucite structure without water molecules. The α-$Ni(OH)_2$/γ-NiOOH couple exhibits a higher specific capacitance than that of the β-$Ni(OH)_2$/β-NiOOH couple due to the greater change in valence.[136] Even though it is not noticeable from the commonly used formulation, the γ-phase of NiOOH has a higher average oxidation state of Ni (3.3–3.7) compared with that of the β-phase due to the presence of Ni^{4+} ions.[137–139] The theoretical specific capacitance of $Ni(OH)_2$ is greater than 3500 F g^{-1}, but the experimental values only reach the range of 500–600 F g^{-1} for powder materials due to their poor conductivity.[136,140] Thus, modification of the morphology of materials promote higher specific capacitances by improving the utilization of the active materials. Yang *et al.*[141] reported a high specific capacitance of 3152 F g^{-1} at 4 A g^{-1} in the voltage range of −0.05 to 0.45 V *vs.* SCE in 3% aqueous KOH electrolyte for porous α-$Ni(OH)_2$ electrodeposited on Ni foam. The high specific capacitance is due to the loosely dispersed $Ni(OH)_2$ particles on the Ni foam. Nevertheless, a poor rate capability (91.1% capacitance degradation by 4 times increment in current density) and poor cycling stability (48% capacitance loss after 300 cycles @ 4 A g^{-1}) were observed because of the intrinsic lower conductivity. Thus, to overcome these limitations, nanostructuring and fabrication of composites are highly required. Wang and co-workers[142] synthesized $Ni(OH)_2$ hexagonal nanocrystals grown on electrically conducting graphene sheets (GS), which exhibited specific capacitances of 1335 and 953 F g^{-1} at current densities of 2.8 and 45.7 A g^{-1}, respectively, in the voltage range of −0.05 to 0.50 V *vs.* Ag/AgCl in 1 M KOH electrolyte. Together with the good rate capability, an appreciable energy density of 37 W h kg^{-1} (@10 kW kg^{-1}) and excellent cycling stability (100% capacitance retention after 2000 cycles @ 28.6 A g^{-1}) were demonstrated by the $Ni(OH)_2$/GS electrode. Similar to $Ni(OH)_2$, $Co(OH)_2$ possesses a hexagonal-layered structure together with α- and β-polymorphs, where α-$Co(OH)_2$ exhibits a better supercapacitive performance. Eqn (30) and then eqn (29) demonstrate the supercapacitive redox reactions of $Co(OH)_2$.

$$Co(OH)_2 + OH^- \leftrightarrow CoOOH + H_2O + e^- \quad (30)$$

The theoretical specific capacitance of $Co(OH)_2$ is above 3600 F g^{-1}, but in reality, a considerably lower capacitance together with poor rate capability and cycle life are observed due to its low conductivity. As described for $Ni(OH)_2$, similar strategies have to be employed to improve the performance of $Co(OH)_2$-based supercapacitors. Jagadale *et al.*[143] synthesized α-$Co(OH)_2$ nanoflakes, which were uniformly loaded on highly conducting flexible carbon fiber (CF) paper, showing a specific capacitance of 386.5 F g^{-1} at 1 mA cm^{-2} in the voltage range of 0–0.5 V *vs.* Ag/AgCl in 1 M LiOH. The composite electrode demonstrated 92% capacitance retention over 2000 charge/discharge cycles at 10 mA cm^{-2}. Furthermore, a flexible solid-state symmetric

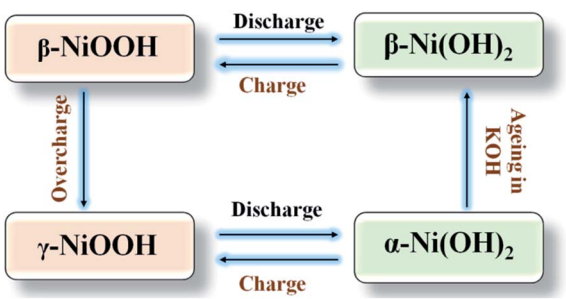

Fig. 9 Bode diagram: transformation between NiOOH and $Ni(OH)_2$.

device was assembled with PVA/LiOH polymer gel electrolyte, which delivered an energy density of 4.3 W h kg^{-1} at a power density of 424 W kg^{-1} in the voltage window of 0–1 V. On the other hand, $Fe(OH)_2$ (redox couple: Fe^{2+}/Fe^{3+})[144] and $Fe(OH)_3$ (redox couple: Fe^0/Fe^{3+})[145] are also promising supercapacitive materials through the following surface redox reactions.

$$Fe(OH)_2 + OH^- \leftrightarrow FeOOH + H_2O + e^- \quad (31)$$

$$Fe + 3OH^- \leftrightarrow Fe(OH)_3 + 3e^- \quad (32)$$

Owusu and co-workers[144] reported an asymmetric supercapacitor with the (+)$NiMoO_4$//2 M KOH//$Fe(OH)_2$/FeOOH(−) configuration, where the $Fe(OH)_2$/FeOOH negative electrode exhibited a high specific capacitance (1066 F g^{-1} @ 1 A g^{-1} in the voltage range of −1.2 to 0 V *vs.* SCE), good rate capability (74.6% capacitance retention from 1–30 A g^{-1}) and outstanding cycling stability (91% capacitance retention @ 30 A g^{-1} after 10 000 cycles). The asymmetric device delivered a specific capacitance of 273 F g^{-1} (@1.5 A g^{-1}), energy density of 104.3 W h kg^{-1} (@1.27 kW kg^{-1}), power density of 10.94 kW kg^{-1} (@31 W h kg^{-1}) and good cycling stability (80.8% capacitance retention after 10 000 cycles @ 22.5 A g^{-1}) in the voltage window of 0–1.7 V. Fan *et al.*[145] synthesized an $Fe(OH)_3$ film on Fe foam ($Fe(OH)_3$@Fe) as the negative electrode of supercapacitors, where $Fe(OH)_3$@Fe achieved areal capacitances in the range of 5.55–3.94 F cm^{-2} in the current range of 20–200 mA cm^{-2} and voltage window of −1.4 to 0 V *vs.* Ag/AgCl in KOH–NaCl electrolyte. The fabricated asymmetric device, namely, (+) Co_3O_4@Ni//KOH–NaCl//$Fe(OH)_3$@Fe(−), demonstrated a specific capacitance of 3.40 F cm^{-2} (@20 mA cm^{-2}), energy density of 11.64 W h m^{-2} (@157 W m^{-2}) and power density of 1461 W m^{-2} (@7.43 W h m^{-2}) in the voltage window of 0–2 V.

LDHs[146] have attained great interest as supercapacitive materials due to the facile tunability of their composition, structure and morphology. Basically, LDHs are 2D multi-metal clay materials, which are comprised of brucite layers of metal cations octahedrally enclosed by hydroxyls, forming $M^{2+}(OH)_6$/$M^{3+/4+}(OH)_6$ octahedra.[147] The general formula of LDHs is $[M_{1-x}{}^{2+}N_x{}^{3+}(HO^-)_2]^{x+}[(X^{n-})_{x/n}\cdot yH_2O]^{x-}$, where X^{n-} is the intercalating anion(s). Xie *et al.*[148] reported an asymmetric supercapacitor based on the (+)AC//6 M KOH//CoNi-LDH(−) configuration, where the CoNi-LDH negative electrode (Co/Ni = 1 : 1, surface area: 109.8 m^2 g^{-1}) exhibited a specific capacitance of 2614 F g^{-1} at 1 A g^{-1} in the voltage range of 0–0.5 V *vs.* Hg/HgO. The asymmetric device exhibited a specific capacitance of 149 F g^{-1} (@142.8 mA g^{-1}), energy density of 46.3 W h kg^{-1} (@102.3 W kg^{-1}), power density of 1704.5 W kg^{-1} (@25.6 W h kg^{-1}) and moderate cycling performance (84.5% capacitance retention after 1000 cycles @ 476 mA g^{-1}) in the voltage window of 0–1.5 V. By contrast, with mono- and bi-active metal hydroxides, multi-active metal hydroxides provide better utilization of the redox active sites due to the multi-valence synergistic effect. Sivakumar *et al.*[149] reported a hexagonal nanoplate-like architecture of NiCoMn-ternary-component-LDH (NCM-LDH; Ni : Co : Mn = 2.01 : 0.50 : 0.49) with a controlled size and composition through a one-pot hydrothermal process, which showed a specific capacitance of 1188 F g^{-1} at 1 A g^{-1} in the voltage window of 0–0.5 V *vs.* Hg/HgO in 6 M KOH medium. The full cell with the (+)NCM-LDH//6 M KOH//AC(−) configuration delivered a specific capacitance of 136.2 F g^{-1} (@1 A g^{-1}), energy density of 42.56 W h kg^{-1} (@726.17 W kg^{-1}), power density of 17 791.56 W kg^{-1} (@24.71 W h kg^{-1}), and good cycling stability (78.8% capacitance retention over 50 000 cycles at 10 A g^{-1}) in the voltage window of 0–1.5 V. To further improve the supercapacitive performances, various composites of LDHs have also been reported in the literature.[146,150,151]

Notably, there is appreciable controversy on the charge storage mechanism (whether pseudo-faradaic or faradaic) for oxides/hydroxides of Ni, Co and Fe in alkaline electrolyte, while unambiguously, compounds of Ru and Mn exhibit the pseudo-faradaic mechanism in acidic and neutral electrolyte, respectively.[152,153] According to the definition given by Conway, a pseudocapacitive electrode always shows a linear function of the stored charge with the width of the voltage window ($C = dq/dV$), but the origin of charge storage mechanism is faradaic in nature. In practice, oxides/hydroxides of Ni, Co and Fe exhibit prominent redox waves in their cyclic voltammogram, and corresponding voltage plateaus in their constant-current charge/discharge curves are observed, which are typical battery-like faradaic in nature, and far from the ideal pseudocapacitive characteristics (quasi-rectangular cyclic voltammogram and quasi-triangular constant-current charge/discharge profile). Consequently, nonlinear functions of charge storage *vs.* voltage window are obtained. By contrast, several researchers also reported pseudocapacitive characteristics in oxides/hydroxides of Ni, Co and Fe in their pristine[141,154] and carbon-composite forms.[142,143] Researchers who described battery-like faradaic and capacitor-like pseudo-faradaic processes estimated the capacity (in coulomb or A h unit) and capacitance (in F unit), respectively, of these materials. However, the controversy originates in the pseudo-faradaic mechanism since it is intermediate in nature between non-faradaic (purely capacitor-like) and faradaic (purely battery-like) processes.[155] Nevertheless, we do not justify any side, only clarify this important concern for readers.

4.3. Metal carbides and composites

Recently, 2D carbides, namely MXenes,[156,157] have been intensively studied in energy storage applications due to their good electrical conductivities, mechanical stability, thermal stability, high melting point, good corrosion resistance and hydrophilic surface. Metal carbides are special metallic structures in which carbon atoms are dispersed in the interstitial voids of densely packed host lattices, which is the origin of their higher electronic conductivity.[158–160] The MXene family is comprised of several carbides, including, Ti_2CT_x, $(Ti_{0.5}Nb_{0.5})_2CT_x$, Nb_2CT_x, Ti_3CNT_x, V_2CT_x, $Ti_3C_2T_x$, $(V_{0.5}Cr_{0.5})_3C_2T_x$, $Ta_4C_3T_x$ and $Nb_4C_3T_x$, among which, $Ti_3C_2T_x$ has been intensively studied.[161,162] Besides the MXene family, other types of carbides, such as WC, Ti_xC_y, Mn_3C, Co_3C, Co_2C and Co_3ZnC, have also been reported in the literature for supercapacitor applications.[163]

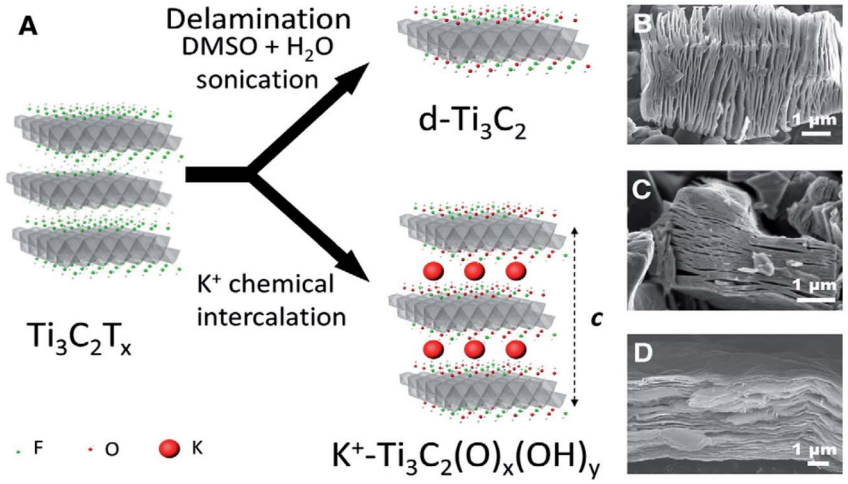

Fig. 10 (A) Schematic routes for the modifications of $Ti_3C_2T_x$: delamination and intercalation. SEM images of (B) $Ti_3C_2T_x$, (C) KOH–Ti_3C_2 and (D) d-Ti_3C_2. Figure reproduced from ref. 163 with permission Copyright (2014) from Elsevier B.V.

Dall'Agnese[163] reported the supercapacitive behaviour of $Ti_3C_2T_x$ in 1 M H_2SO_4 electrolyte, where $Ti_3C_2T_x$ was modified by delamination or intercalation treatment to achieve a high surface area and advanced surface properties towards improved performance. Fig. 10 depicts the modification routes of $Ti_3C_2T_x$, *i.e.* (i) delamination through the insertion of dimethyl sulfoxide (DMSO) solvent (d-Ti_3C_2) and (ii) chemical intercalation of K^+ ions between $Ti_3C_2T_x$ layers by KOH treatment (KOH–Ti_3C_2). Through both modification routes, the F-terminations of $Ti_3C_2T_x$ were mostly replaced by hydroxyl groups. In the case of the delamination process, the surface area increased from 23 to 98 $m^2\ g^{-1}$, and consequently, d-Ti_3C_2 demonstrated a higher specific capacitance (415 F cm^{-3} @ 5 A g^{-1} in the voltage window of −0.4 to 0.2 V *vs.* Ag/AgCl) compared to that of KOH–Ti_3C_2 (215 F cm^{-3}). Moreover, both modified species (d-Ti_3C_2 and KOH–Ti_3C_2) showed a better capacitance than $Ti_3C_2T_x$ due to the change in their surface chemistries. Both d-Ti_3C_2 and KOH–Ti_3C_2 exhibited a stable cycling performance at 5 A g^{-1} over 10 000 cycles. Morishita and co-workers[164] synthesized porous carbon-coated WC and Mo_2C *via* the heat treatment of K_2WO_4 and K_2MoO_4 with hydroxy propyl cellulose, respectively. WC and Mo_2C were converted into their respective hydroxides during the first charge/discharge cycle in aqueous H_2SO_4 medium, which exhibited the respective redox reactions in further cycles. The carbon-coated WC and Mo_2C demonstrated stable specific capacitances of 350 F cm^{-3} (over 300 cycles) and 730 F cm^{-3} (over 500 cycles), respectively, at 50 mA g^{-1} in the voltage range of 0–1 V *vs.* Ag/AgCl in 1 M H_2SO_4 electrolyte, which are much higher than that of porous carbons without metal carbides (140 F cm^{-3}). The beneficial effects of carbon coating on metal carbides are multi-directional, such as (i) restricts the growth of carbide particles during their formation, where small-sized particles facilitate the complete transformation of carbides to hydroxides in the first charge/discharge cycle, (ii) prevent the agglomeration of metal hydroxides upon further cycling, and (iii) contribute additional capacitance through the formation of EDLs with electrolyte ions. Kim and Kim[165] constructed a high voltage asymmetric supercapacitor using SiC–MnO_2 nanoneedles (SiC–MnO_2) as the positive electrode, thermally functionalized AC (with oxygen containing groups) as the negative electrode and 1 M Na_2SO_4 (aq.) as the electrolyte. In the SiC–MnO_2 composite (MnO_2/SiC feeding ratio of 5 : 1), the MnO_2 nanoneedles were homogeneously decorated on the SiC surface due to the anchoring of the MnO_2 nanostructures by the SiC surface functionalities (epoxy and hydroxyl groups). This nanostructure provided a larger specific surface area together with facile pathways for electrolyte ion diffusion. The SiC–MnO_2 nanocomposite showed a specific capacitance of 273.2 F g^{-1} at 10 mV s^{-1} in the voltage range of −0.1 to 0.9 V *vs.* Ag/AgCl in 1 M Na_2SO_4 (aq.), which is much higher than that of pristine SiC (72.4 F g^{-1}). The asymmetric device delivered a specific capacitance of 59.9 F g^{-1} (@2 mV s^{-1}), energy density of 30.06 W h kg^{-1} (@113.92 W kg^{-1}) and superb cycling stability (3.1% capacitance decay after 1000 cycles @ 50 mV s^{-1}) in the voltage window of 0–1.9 V. Shan *et al.*[166] reported the electrochemical performances of delaminated V_2C MXene in three different aqueous electrolytes, namely, 1 M H_2SO_4, 1 M $MgSO_4$ and 1 M KOH. The specific capacitances achieved were 487 F g^{-1} (−1.1 to −0.3 *vs.* Hg/$HgSO_4$) in 1 M H_2SO_4, 225 F g^{-1} (−1.2 to 0 V *vs.* Ag) in 1 M $MgSO_4$, and 184 F g^{-1} (−1.2 to −0.6 V *vs.* Ag) in 1 M KOH medium at a scan rate of 2 mV s^{-1}. Moreover, the capacitance retention was observed to be 83%, 99% and 94% in 1 M H_2SO_4, 1 M $MgSO_4$ and 1 M KOH, respectively, at 10 A g^{-1} after 10 000 cycles within the respective voltage ranges mentioned above. The poor cycling stability in 1 M H_2SO_4 medium is attributed to the V-dissolution in electrolyte, which was experimentally detected by inductively coupled plasma (ICP) spectrometry. However, the state-of-the-art capacitance and durability of metal carbides do not satisfy commercial benchmarks, which can be improved by controlling the material morphology (nanoscale particles, composites, *etc.*) and electrode architecture (thin and porous structure).[167]

4.4. Metal nitrides and composites

In 1998, Conway and his group[168] reported the pseudocapacitive characteristics of Mo_xN (MoN and Mo_2N) during their search for low-cost alternatives to RuO_2. The Mo_xN film deposited by CVD showed similar pseudocapacitive behaviour to RuO_2, but a lower operating voltage (0.7 V *vs.* RHE) was obtained compared to that of the RuO_2 film (1.35 V *vs.* RHE) in H_2SO_4 medium. Beyond the positive potentials of 0.7 V, an over-charged faradaic current was observed, even below the potential of oxygen evolution reaction, which indicates the anodic decomposition of the Mo_xN film and probable formation of non-stoichiometric MoO_2. In recent years, metal nitrides (MN, M = V, Ti, Mo, W, Ga, Nb, Ta, Cr, Mn, Fe, Co, Ni, *etc.*)[19,169,170] have been widely applied in chemical supercapacitors due to their well-defined pseudocapacitive surface-redox behaviours and high electronic conductivities. Several researchers are focused on VN due to its high theoretical capacity (>41 000 F g^{-1}), metal-like conductivity, fast and reversible redox response in the various oxidation states (+2 to +5) of vanadium, and high overpotential for the hydrogen evolution reaction.[171–173] Cheng *et al.*[174] synthesized nanocrystalline VN (surface area: 56.8 m^2 g^{-1} and electronic conductivity: ~5.8 × 10^3 Ω^{-1} m^{-1}) through the melamine reduction of V_2O_5 xerogel, and its performance was tested in various aqueous electrolytes. The specific capacitances achieved were 114 F g^{-1} (−0.5 to 0.5 V *vs.* SCE), 45.7 F g^{-1} (−0.7 to 0.3 V *vs.* SCE) and 273 F g^{-1} (−1.1 to 0 V *vs.* Hg/HgO) in 0.5 M H_2SO_4, 2.0 M $NaNO_3$ and 1.0 M KOH solutions, respectively, at a scan rate of 30 mV s^{-1}. The operating capacitive and pseudocapacitive processes of VN in H_2SO_4, $NaNO_3$ and KOH media are presented in eqn (33)–(35), respectively.

$$VN_xO_y + SO_4^{2-} + H_2O \leftrightarrow VN_xO_y||SO_4^{2-} + VN_xO_y\text{–}OH + H^+ \quad (33)$$

$$VN_xO_y + NO_3^- \leftrightarrow VN_xO_y||NO_3^- \quad (34)$$

$$VN_xO_y + OH^- \leftrightarrow VN_xO_y||OH^- + VN_xO_y\text{–}OH \quad (35)$$

Herein, $VN_xO_y||SO_4^{2-}$, $VN_xO_y||NO_3^-$ and $VN_xO_y||OH^-$ correspond to the EDLs, while VN_xO_y–OH represents the redox pseudocapacitance. Therefore, it can be concluded that the charge storage mechanisms of VN depend on the nature of the electrolyte. On a different note, the presence of oxygen on the surface of VN was detected by Fourier-transform infrared spectroscopy (FTIR) and X-ray photoelectron spectroscopy (XPS), while its composition was determined to be $VN_{1.02}O_{0.1}$. It is a common problem for metal nitrides that they are not stable in aqueous solution due to the irreversible formation of oxides layers on their surface, which are partially soluble in electrolyte. An *et al.*[175] proposed novel VN encapsulated carbon fibre networks (VN/CF), in which carbon encapsulation restricted the direct contact between VN and the aqueous electrolyte, and

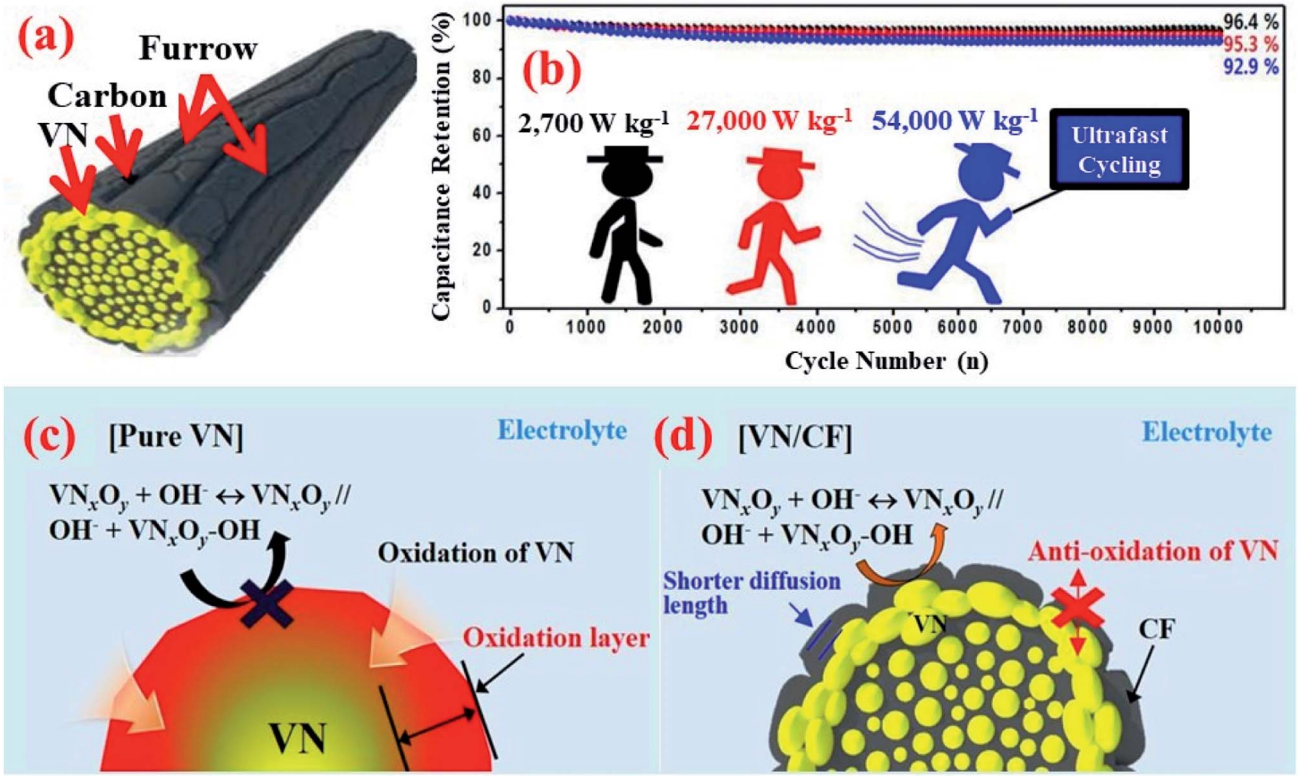

Fig. 11 (a) Schematic drawing of VN/CF composite. (b) Durability test of (+)$Ni(OH)_2$//VN/CF(−) full cell. Schematic illustration of supercapacitive processes, $VN_xO_y + OH^- \leftrightarrow VN_xO_y||OH^- + VN_xO_y$–OH for (c) pristine VN and (d) VN/CF. Figure reproduced from ref. 175 with permission Copyright (2017) from The Royal Society of Chemistry.

consequently, the surface oxidation of VN was minimized. Hence, the VN/CF composite (~5.3 nm thick continuous carbon layer on 35–41 nm sized VN particles; Fig. 11(a)) electrodes exhibited a higher specific capacitance (800 F g^{-1}) compared to commercial pristine VN (43 F g^{-1}) at 4 A g^{-1} in the voltage range of −1.2 to 0 V *vs.* Ag/AgCl in 6 M KOH electrolyte. The full cell with the (+)$Ni(OH)_2$//6 M KOH//VN/CF(−) configuration demonstrated a specific capacitance of 188 F g^{-1} (@4 A g^{-1}), energy density of 53.1 W h kg^{-1} (@2700 W kg^{-1}) and power density of 54 000 W kg^{-1} (@36 W h kg^{-1}) in the voltage range of 0–1.6 V. The asymmetric full cell exhibited excellent capacitance retentions of 96.4%, 95.3% and 92.9% over 10 000 cycles at current densities of 4 A g^{-1} (2700 W kg^{-1}), 40 A g^{-1} (27 000 W kg^{-1}), and 80 A g^{-1} (54 000 W kg^{-1}), respectively (Fig. 11(b)). The carbon encapsulation prevented the surface oxidation of VN, and hence, maintained an excellent cycle life together with high specific capacitance, which is schematically shown in Fig. 11(c and d). Similar to VN, TiN (bulk electrical conductivity: ~5×10^6 S m^{-1}) also encounters irreversible surface oxidation according to the following reactions.

$$TiN + 2H_2O \rightarrow TiO_2 + 0.5N_2 + 4H^+ + 4e^- \quad (36)$$

$$2TiN + O_2 \rightarrow TiO_2 + N_2 \quad (37)$$

Nevertheless, carbon or polymer coating, thermal annealing for nitrogen diffusion from the bulk to surface, *etc.* may improve the performances of TiN compared to that of pristine TiN. Grote *et al.*[176] synthesized self-supported carbon-coated TiN nanotube arrays (C-TiN) *via* a conformal carbon coating technique. The C-TiN nanotube array showed specific capacitances of 167 and 95 F g^{-1} at 1 and 50 A g^{-1}, respectively, while that of the pristine TiN nanotube array was 140 and 61 F g^{-1} at respective current densities under −1 to 0 V *vs.* Ag/AgCl in 1 M KOH electrolyte. The C-TiN and pristine TiN electrodes demonstrated 70% and 15% capacitance retention, respectively, at 10 A g^{-1} over 6000 cycles. The long cycle life and high capacitance of C-TiN were achieved due to the effective protection from surface oxidation and EDL contribution from carbon. Achour *et al.*[177] studied nitrogen (β-N) doping in the oxidized surface of TiN films (diffusion from bulk to surface) *via* a vacuum annealing method and its effects on their supercapacitive performances. XPS analysis depicted that the annealing of the TiN film facilitated the diffusion of β-N from the sub-surface to the oxidized surface, and accordingly, an N-substituted TiO_x layer was formed. This phenomenon prevented the further oxidation of the TiN film surface. It was noticed that the β-N content in the TiN film surface increased by increasing the annealing temperature, and concomitantly, the specific capacitance of the TiN film improved. This is due to the generation of more pseudocapacitive active sites with an increase in surface oxygen vacancies, which are correlated with the β-N content in the surface. Notably, TiN films were deposited on Si wafers by the DC reactive magnetron sputtering technique, where Ar (99.999%) and N_2 (99.999%) were employed as the sputtering and reactive gases, respectively. The N_2 excess during deposition led to an increase in the N-content at the TiN surface. However, the annealed TiN film (@550 °C) exhibited a specific capacitance of 8.2 mF cm^{-2} at 2 mV s^{-1} within −0.2 to 0.5 V *vs.* Ag/AgCl in 0.5 M K_2SO_4 (aq.) electrolyte, which is ~3 times higher than that of the unannealed TiN film. However, MN (M = V or Ti) are promising candidates for negative electrodes in asymmetric supercapacitors in alkaline media. Kartachova *et al.*[178] elucidated the supercapacitive characteristics of WN (composition: $W_{0.75}$(N,O), where O/N varied between 0.3 and 1 and surface area: 42 m^2 g^{-1}) in different aqueous electrolytes including 1 M H_2SO_4 (~67 F g^{-1}, −0.4 to 0.5 V *vs.* Ag/AgCl), 1 M KOH (~57 F g^{-1}, −1.1 to 0.3 V *vs.* Hg/HgO), 3 M KCl (~18 F g^{-1}, −0.9 to 0.5 V *vs.* Ag/AgCl), 3 M NaCl (~16 F g^{-1}, −0.9 to 0.5 V *vs.* Ag/AgCl), 1 M LiCl (~28 F g^{-1}, −0.9 to 0.5 V *vs.* Ag/AgCl) and 1 M $CaCl_2$ (~39 F g^{-1}, −0.9 to 0.5 V *vs.* Ag/AgCl) at 0.5 A g^{-1} current density. By contrary, the best cycling stability of WN was observed in 1 M KOH medium. This is attributed to the unfeasibility of the bulk intercalation of protons or cations into WN, where pseudocapacitive ion adsorption will be the probable supercapacitive mechanism. In a different study,[179] the specific capacitances for NbN and γ-Mo_2N crystallites were found to be 73 F g^{-1} (−1.0 to −0.7 V *vs.* Hg/HgO) and 111 F g^{-1} (−1.1 to −0.2 V *vs.* Hg/HgO), respectively, at 2 mV s^{-1} in 1 M KOH electrolyte. Wang and group[180] fabricated a single-crystal GaN mesoporous membrane (GaNMM; surface area: 23.2 m^2 g^{-1} and pore size ~20 nm; electrical conductivity: 44.19 S cm^{-1}) through an electrochemical etching process and electrochemically characterized in two different aqueous electrolytes, namely, 1 M H_2SO_4 and 1 M Na_2SO_4. The specific capacitances achieved were 23 mF cm^{-2} in 1 M H_2SO_4 and 18 mF cm^{-2} in 1 M Na_2SO_4 at 0.5 mA cm^{-2} within −0.5 to 0.4 V *vs.* Hg/Hg_2SO_4. This result indicates that protons enhance the pseudocapacitance of GaN through the pseudo-faradaic reaction with surface oxynitride thin films, as shown in eqn (38).

$$GaN_{1-x}O_x + 2yH^+ + 2ye^- \leftrightarrow GaN_{1-x-y}O_{x-y} + yH_2O \quad (38)$$

However, the symmetric supercapacitor based on GaNMM delivered a specific capacitance of 23.11 mF cm^{-2} (@0.5 mA cm^{-2}), energy density of 0.65 μW h cm^{-2} (@0.5 mA cm^{-2}) and power density of 45 mW cm^{-2} (@100 mA cm^{-2}) in the voltage window of 0–0.9 V. The capacitance retentions were observed to be 98% (@10 mA cm^{-2}) and 98.8% (@5 mA cm^{-2}) for the first 30 000 and last 20 000 cycles, respectively. Wei *et al.*[181] fabricated a CrN thin film using reactive DC magnetron sputtering and tested it in a symmetric full cell in 0.5 M H_2SO_4 medium. The symmetric device delivered a specific capacitance of 6.5 mF cm^{-2} (@1.0 mA cm^{-2}), energy density of 8.2 mW h cm^{-3} (@0.7 W cm^{-3}) and good cycling stability (10% capacitance loss after 20 000 @ 2.0 mA cm^{-2}) in the voltage window of 0–0.8 V. Cui and co-workers[182] synthesized N-doped carbon-coated Nb_4N_5 (Nb_4N_5@NC) nanochannels and characterized them in a symmetric full cell using 1 M H_2SO_4 electrolyte. The device showed a specific capacitance of 116.45 mF cm^{-2} (@0.5 mA cm^{-2}), energy density of 4.66 mW h cm^{-3} (@24.56 W cm^{-3}) and power density of 25.21 W cm^{-3} (@2.93 mW h cm^{-3}) in the voltage window of 0–1 V. Besides the various binary metal

nitrides, ternary metal nitrides (such as TiVN)[183] and composites of two binary metal nitrides (such as TiN/VN)[184] are also envisaged for chemical supercapacitor applications.

4.5. Metal phosphides, phosphates, phosphites and composites

In recent years, phosphorous-based metal compounds, such as phosphides, phosphates and phosphites, have been widely used in chemical supercapacitors due to their greater ionic cum electronic conductivity and open nano/meso porous framework structures. Phosphorus reacts with several elements and forms versatile phosphide compounds with metalloid characteristics, high chemical stability and mechanically sturdy flexible architectures. Du *et al.*[185] constructed symmetric and asymmetric supercapacitor cells based on Ni_2P nanoparticles in 3 M KOH medium. The symmetric device exhibited a specific capacitance of 1.70 F g^{-1} (@0.2 mA cm^{-2}), energy density of 0.24 W h kg^{-1} (@42 W kg^{-1}) and power density of 170 W kg^{-1} (@0.09 W h kg^{-1}) in the voltage range of 0–1 V. In contrast, the asymmetric (+)Ni_2P//AC(−) device delivered a specific capacitance of 237.4 F g^{-1} (@1 mA cm^{-2}), energy density of 64.6 W h kg^{-1} (@1029 W kg^{-1}) and power density of 20 580 W kg^{-1} (34.3 W h kg^{-1}) in the voltage range of 0–1.5 V. Lu *et al.*[186] synthesized Ni_2P particles, which were homogenously coated (thickness: 20–30 nm) with amorphous Ni *via* an electroless plating process. The Ni_2P/Ni composite electrode showed a high specific capacitance of 581 F g^{-1} at 1 A g^{-1} in the voltage window of 0–0.55 V *vs.* Hg/HgO in 2 M LiOH electrolyte and 19% capacitance reduction at 40 A g^{-1}, whereas the respective data for the pristine Ni_2P electrode was 418 F g^{-1} and 22%. The large surface area of the Ni flake coating led to an enhancement in the ion and electron transport, which was responsible for the improved specific capacitance of composite over the pristine electrode. The Ni_2P/Ni composite electrode delivered an energy density of 83.6 W h kg^{-1} (@2.7 kW kg^{-1}) and power density of 10.9 kW kg^{-1} (70.2 W h kg^{-1}), whereas the Ni_2P pristine electrode shows about half of this energy density at a similar power density. In the durability test at 2 A g^{-1}, initial capacitance enhancements were observed for both Ni_2P/Ni and Ni_2P due to the activation processes of the electrodes, which reached the maximum near the 500th cycle. Thereafter, the Ni_2P/Ni electrode lost only 7.7% of its maximum capacitance over the next 2500 cycles, while the capacitance degradation was much higher for the pristine Ni_2P electrode. To overcome the short-term cycling stability, Elshahawy and co-workers[187] synthesized sulfur-doped CoP nanotube arrays aligned on carbon cloth (Co(P,S)/CC), which exhibited overall improved electrochemical performances than that of the pristine CoP. Co(P,S)/CC and CoP/CC displayed the specific capacitances of 610 and 342.8 F g^{-1} at 1 A g^{-1} in the voltage range of −0.2 to 0.4 V *vs.* Ag/AgCl in 6 M KOH electrolyte, and retained 56% and 46% of their initial capacitance with an increase in the current density to 20 A g^{-1}, respectively. The improved rate capability of the Co(P,S)/CC electrode is attributed to its lower ESR value (∼0.4 Ω) compared to that of CoP/CC (∼0.51 Ω). Subsequently, 99% and 70% capacitance retention was observed for Co(P,S)/CC and CoP/CC, respectively, at 10 A g^{-1} current density after 10 000 cycles. The poor cycling stability of the pristine CoP/CC electrode is due to the formation of a passivating oxy-hydroxide phase on the surface, and consequently, a reduction in the electrode conductivity and active material utilization are unavoidable. Herein, sulfur doping effectively prevented the formation of passivation layers on the electrode surface and improved the cycling performances. An asymmetric supercapacitor was assembled by employing Co(P,S)/CC as the positive electrode, porous carbon polyhedron (PCP)/rGO hydrogel as the negative electrode and 6 M KOH as the electrolyte. It delivered a specific capacitance of 109.5 F g^{-1} (@1 A g^{-1}), energy density of 39 W h kg^{-1} (@0.8 kW kg^{-1}), power density of 30.6 kW kg^{-1} (@18.7 W h kg^{-1}) and excellent cycling performance (92.6% capacitance retention after 30 000 cycles at 10 A g^{-1}) in the voltage range of 0–1.6 V.

Li *et al.*[188] synthesized hierarchical 3D cobalt phosphate octahydrate ($Co_3(PO_4)_2 \cdot 8H_2O$) *via* a room temperature precipitation method without employing any surfactants. The as-synthesized flower-like structure with interconnecting 2D microsheets provided a high surface area and open channels for electrolyte infiltration, and consequently, demonstrated good pseudocapacitive performances. $Co_3(PO_4)_2 \cdot 8H_2O$ attained a specific capacitance of 350 F g^{-1} (@1 A g^{-1}), good rate capability (227 F g^{-1} @ 10 A g^{-1}) and excellent durability (102% capacitance retention over 1000 cycles @ 1 A g^{-1}) in the voltage range of 0–0.45 V *vs.* Ag/AgCl in 3 M KOH electrolyte. Zhao and co-workers[189] developed a novel hybridized NH_4–Ni–Co phosphate *via* a hydrothermal sacrificial template method, which was comprised of $(Ni,Co)_3(PO_4)_2 \cdot 8H_2O$ nanoslices (∼1 nm) and single crystal $(NH_4)(Ni,Co)PO_4 \cdot 0.67H_2O$ microplatelets. The mixed-phase material exhibited a high specific capacitance of 1128 F g^{-1} at 0.5 A g^{-1} in the voltage range of 0–0.45 V *vs.* Hg/HgO in 6 M KOH. R_s and R_{ct} were estimated from the Nyquist plot in EIS, and the respective values were determined to be 1.29 and 1.38 Ω. The lower resistive characteristics are attributed due to the novel structural properties of the hybridized NH_4–Ni–Co phosphate. In particular, the single crystal $(NH_4)(Ni,Co)PO_4 \cdot 0.67H_2O$ microplatelets provide an electronic pathway by bridging the $(Ni,Co)_3(PO_4)_2 \cdot 8H_2O$ nanoslices, and the channels generated between the microplate and nanoslices offer a facile ionic movement (Fig. 12(a)). The synergistic effect between the two phases boosts the supercapacitive behaviours for the NH_4–Ni–Co phosphate, and the associated pseudo-faradaic reactions are presented as follows:

$$(NH_4)(Ni,Co)PO_4 \cdot 0.67H_2O + OH^- \leftrightarrow (NH_4)(Ni,Co)(OH)PO_4 + e^- \quad (39)$$

$$(Ni,Co)_3(PO_4)_2 \cdot 8H_2O + 3OH^- \leftrightarrow (Ni,Co)_3(OH)_3(PO_4)_2 \cdot 8H_2O + 3e^- \quad (40)$$

The microplatelet $(NH_4)(Ni,Co)PO_4 \cdot 0.67H_2O$ phase with a large interlayer distance (0.875 nm) facilitated the diffusion of electrolyte ions and electrons. Hence, the enhanced electronic conductivity and fast ion diffusion kinetics enabled the facile

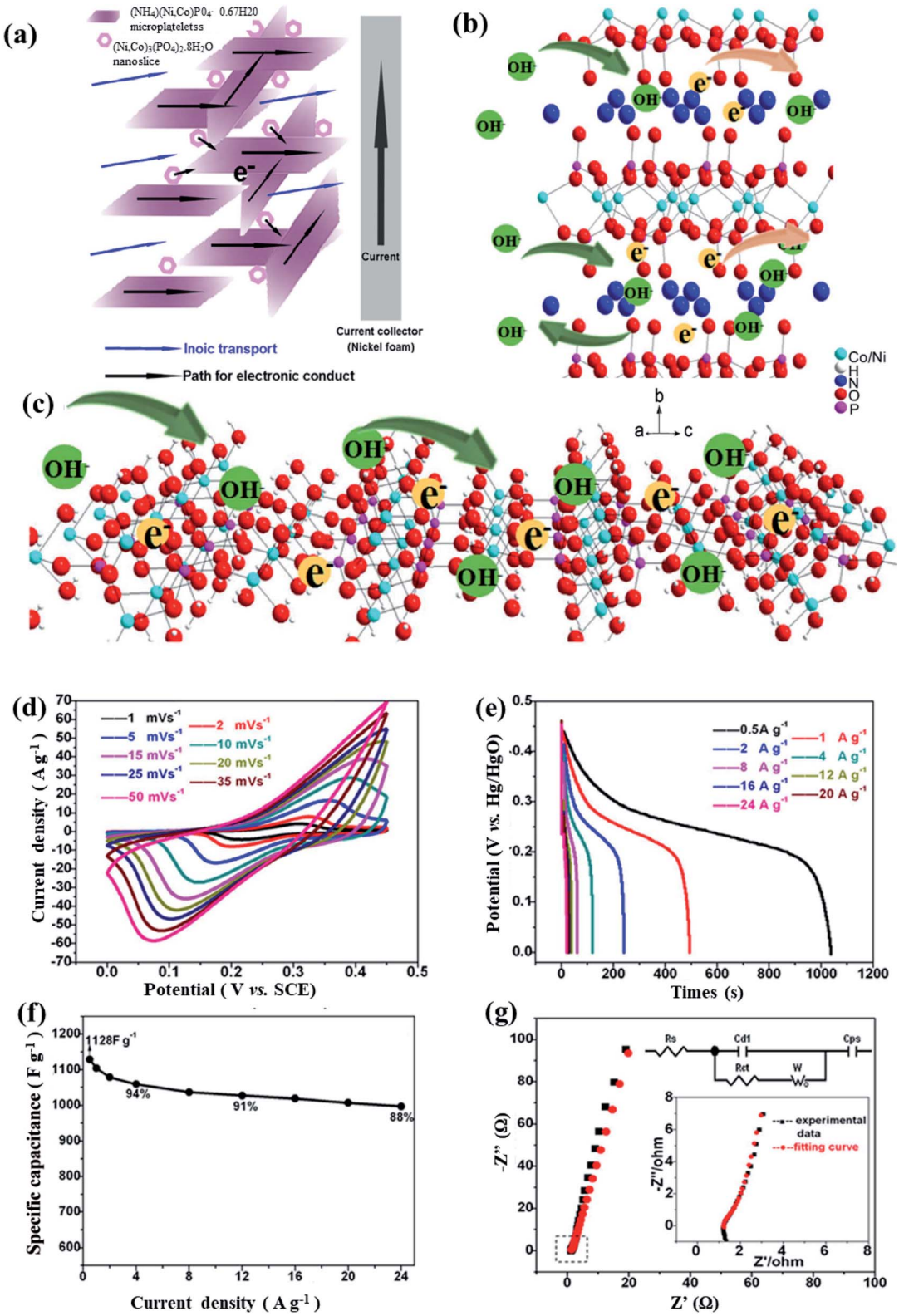

Fig. 12 Schematic drawing for (a) ionic and electronic conduction pathways in the hybrid structure, (b) intercalation/deintercalation of hydroxyl ions, and (c) redox-pseudocapacitance through surface redox reactions. Electrochemical performances of the hybrid material: (d) CV profiles at different scan rates, (e) GCD profiles at different current densities, (f) rate capability characteristics, and (g) Nyquist plots with the fitting curve. Figure reproduced from ref. 189.

intercalation/deintercalation of the hydroxyl ions between the atomic layers (Fig. 12(b)). On the other hand, the nanoslice $(Ni,Co)_3(PO_4)_2 \cdot 8H_2O$ phase provided a large amount of electroactive surface redox sites (Fig. 12(c)) for redox-pseudocapacitance. Fig. 12(d–g) provide the CV characteristics, GCD profiles, rate capability behaviour and EIS analysis, respectively, for the hybrid material. An asymmetric device was assembled in 6 M KOH with NH_4–Ni–Co phosphate as the positive electrode and hierarchical porous carbon (HPC) as the negative electrode. This device exhibited a specific capacitance of 77 F g^{-1} (@0.1 A g^{-1}), energy density of 35.3 W h kg^{-1} (@101 W kg^{-1}), power density of 4400 W kg^{-1} (@30.9 W h kg^{-1}) and outstanding cycling stability (95.6% capacitance retention over 5000 @ 1 A g^{-1}) in the voltage window of 0–1.65 V window. Chen and co-workers[190] reported the improved specific capacitance of amorphous $Ni_{0.8}Co_{0.2}$-pyrophosphate (1259 F g^{-1}) compared to Ni-pyrophosphate (945 F g^{-1}) and Co-pyrophosphate (358 F g^{-1}) at 1.5 A g^{-1} in the voltage range of 0 to 0.55 V *vs.* Hg/HgO in 3 M KOH medium. In $Ni_{0.8}Co_{0.2}$-pyrophosphate, electroactive centers are participated in the surface-redox reactions from valence interchange accompanied with charge hopping between the Ni and Co cations. Therefore, rational tuning of the Ni/Co ratio is truly critical for achieving optimized supercapacitive performances. The (+)$Ni_{0.8}Co_{0.2}$-pyrophosphate//3 M KOH//AC(−) full cell demonstrated a specific capacitance of 119 F g^{-1} (@1 A g^{-1}), energy density of 42.4 W h kg^{-1} (@1 A g^{-1}), power density of 5.6 kW kg^{-1} (@7 A g^{-1}) and moderate cycling performance (80% capacitance retention with ∼96% coulombic efficiency over 2000 cycles @ 1.5 A g^{-1}) in the voltage range of 0–1.6 V. A sea-urchin-like bimetallic phosphide/phosphate composite (Ni–Co–P/PO_x; Ni/Co = 1 : 1) was synthesized by Chen *et al.*[191] *via* a low-temperature phosphating method, in which the crystalline phosphide nanoparticles were distributed in the matrix of the amorphous phosphate phase. The asymmetric supercapacitor with the configuration of (+)Ni–Co–P/PO_x//6 M KOH//rGO(−) delivered a specific capacity of 182 C g^{-1} (@1 A g^{-1}), energy density of 36.84 W h kg^{-1} (@727.8 W kg^{-1}), power density of 5.67 kW kg^{-1} (@19.87 W h kg^{-1}) and moderate cycle life (86% of capacitance retention after 7000 cycles @ 3 A g^{-1}) in the voltage window of 0–1.5 V.

Wang *et al.*[192] synthesized $NiHPO_3 \cdot H_2O$ nanorods with high electrical conductivity and a hierarchical pore structure *via* a one-step hydrothermal method. The CV analysis with varying scan rate produced the *b*-value of 0.71 and 0.64 for the cathodic and anodic peak potentials, respectively, which that signifies the simultaneous diffusion-controlled and surface-controlled processes are associated with Ni^{2+} and Ni^{3+} interconversion. The $NiHPO_3 \cdot H_2O$ (surface area: 22.4 m^2 g^{-1}) electrode showed a high specific capacitance of 1405.6 F g^{-1} at 1 A g^{-1} in the voltage range of 0–0.45 V *vs.* Hg/HgO in 2 M KOH electrolyte together with excellent rate capability (64.2% capacitance retention at 10 A g^{-1}) and good cycling stability (77.3% capacitance retention @ 10 A g^{-1} after 5000 cycles). An asymmetric supercapacitor based on the $NiHPO_3 \cdot H_2O$ positive electrode and hierarchical porous carbon derived from pine pollen as the negative electrode was constructed, which exhibited a specific capacity of 120.2 F g^{-1} (@0.5 A g^{-1}), energy density of 42.6 W h kg^{-1} (@449.1 W kg^{-1}), power density of 8384 W kg^{-1} (@20 W h kg^{-1}) and good cycling performance (84.7% capacitance retention after 20 000 cycles @ 5 A g^{-1}) in the voltage range of 0–1.6 V window. Further, microporous $Ni_{11}(HPO_3)_8(OH)_6$ nanocrystals were prepared by Gao and co-workers[193] *via* hydrothermal route and employed in a flexible solid-state asymmetric supercapacitor as the positive electrode. The hydrophosphite (surface area: 398 m^2 g^{-1}) showed a good specific capacitance of 558 F g^{-1} at 0.5 A g^{-1} in the voltage range of 0–0.5 V *vs.* Hg/HgO in 3 M KOH electrolyte, which degraded to 545 F g^{-1} after 10 000 cycles. The (+)$Ni_{11}(HPO_3)_8(OH)_6$//3 M KOH//graphene(−) system demonstrated the specific capacitance of 1.64 F cm^{-3} (@0.5 mA cm^{-2}), energy density of 0.45 mW h cm^{-3} (@0.5 mA cm^{-2}) and power density of 33 mW cm^{-3} (@5 mA cm^{-2}) in the voltage window of 0–1.4 V. The device also demonstrated 100% and 93.3% capacitance retention after 2000 and 10 000 cycles, respectively, at a current density of 0.5 mA cm^{-2}.

4.6. Metal chalcogenides and composites

The 2D metal chalcogenides,[194,195] mainly sulfides, are attracting immense attention in chemical supercapacitors due to their (i) high electrical conductivity, (ii) high electrochemical, mechanical and thermal stabilities, (iii) quantum-sized effects, and (iv) structural flexibility. The structures and properties of metal chalcogenides are similar to that of pristine graphene, except for their band-gap.[14] In the case of pristine graphene, its band-gap is close to zero, while that depends on the elemental combination, number of layers and amount of doping atoms for metal chalcogenides. Hence, the band-gap values of metal chalcogenides exist in the range of 0 to 2 eV, and because of these variations, different tunable structures can be achieved.[12] The metal chalcogenides exist in two crystallographic phases, namely, semiconducting 2H and conducting 1T phases.[196] The excellent electrochemical activities of metal chalcogenides originate from the edge planes of the 2D layers in their anisotropic crystal structures.[197,198] However, despite their appealing properties, monolithic electrodes of metal chalcogenides show a low surface area and excessive volume change upon cycling due to the re-stacking of their 2D nanosheets. Thus, exfoliation or delamination of the nanosheets provide a higher electroactive surface area towards electrolytes and also renders sufficient buffer regions to accommodate the volume change. Nonetheless, an exfoliated sheet-like morphology with sub-atomic thickness, high surface area and active edge sites in the 2D sheets of metal chalcogenides are pivotal to form hybrid nanostructures with other functional materials. Kandula *et al.*[199] designed a 3D hierarchical Co_9S_8/α-MnS@NC@MoS_2 nanowire structure from the conversion of a binary metal oxide ($MnCo_2O_4$) core to individual metal sulfide (Co_9S_8/α-MnS) core together with the simultaneous formation of an outer metal sulfide shell (MoS_2) *via* a hydrothermal sulfurization reaction, where N-doped carbon (NC) was located between the core and shell as the interlayer. The hybrid structure provided the following synergism; (i) the mesoporous Co_9S_8/α-MnS core

improved the electrical conductivity due to the lower band-gap and more covalent nature of metal–sulfide bonds, (ii) the conducting intermediate NC layer provides a facile pathway for electron and ion transport, (iii) the intermediate NC layer is beneficial for the homogeneous deposition of a porous MoS_2 shell on the Co_9S_8/α-MnS core, (iv) the porous MoS_2 shell protects the electroactive core and facilitates electrolyte diffusion through the porous channels, and (v) the MoS_2 shell accommodates the volume change of the Co_9S_8/α-MnS core upon repetitive cycling. Thus, this hybrid material (surface area: 71.3 $m^2\ g^{-1}$) showed a greater specific capacitance (1938 F g^{-1} @ 1 A g^{-1} in the voltage range of −0.1 to 0.5 V *vs.* Ag/AgCl in 2 M KOH) compared to its oxide precursors ($MnCo_2O_4$@NC: 1096 F g^{-1} and $MnCo_2O_4$: 472 F g^{-1}). The asymmetric supercapacitor, (+)Co_9S_8/α-MnS@NC@MoS_2//2 M KOH//N-doped graphene(−), demonstrated a specific capacity of 80.2 mA h g^{-1} (@1 A g^{-1}), energy density of 64.2 W h kg^{-1} (@729.2 W kg^{-1}), power density of 11.3 kW kg^{-1} (@23.5 W h kg^{-1}) and good cycling stability (8.1% capacitance loss after 10 000 cycles @ 5 A g^{-1}) in the voltage window of 0–1.6 V. Cai and co-workers[200] synthesized graphene a fiber–$NiCo_2S_4$ nanocomposite (GF/$NiCo_2S_4$) by coating $NiCo_2S_4$ on lightweight (0.24 g cm^{-3}), highly conductive (39 S cm^{-1}) and mechanically robust (221 MPa) graphene fibers *via* the solvothermal deposition method. Well-defined redox characteristics were observed in three-electrode CV by employing 2 M KOH electrolyte in the voltage range of 0–0.5 V *vs.* Ag/AgCl. The pseudocapacitive redox reactions (Ni^{2+}/Ni^{3+} and $Co^{2+}/Co^{3+}/Co^{4+}$) are as follows:

$$NiS + OH^- \leftrightarrow NiSOH + e^- \quad (41)$$

$$CoS + OH^- \leftrightarrow CoSOH + e^- \quad (42)$$

$$CoSOH + OH^- \leftrightarrow CoSO + H_2O + e^- \quad (43)$$

The flexible asymmetric (+)GF/$NiCo_2S_4$//2 M KOH//GF(−) device delivered a specific capacitance of 300 F cm^{-3} (@175.7 mA cm^{-3}) and power density of 1600 mW cm^{-3} (@12.3 mW h cm^{-3}) together with excellent cycling stability (92% capacitance retention over 2000 cycles @ 0.4 A cm^{-3}) within the 0–1.5 V range. Choudhary *et al.*[201] developed flexible supercapacitors based on vertically decorated nanowires (1D-WO_3-core/2D-WS_2-shell) on a W-substrate *via* the spontaneous oxidation/sulfurization of W foil. In this design, all the components, namely, the core, shell and current-collector, were converted from a single material (W). This "one-body" supercapacitor with seamless interfaces demonstrated the following performance benefits: (i) enhanced surface area and improved diffusion kinetics due to vertically aligned nanowires, (ii) efficient carrier transport through the highly conductive and single-crystalline WO_3 core, (iii) facile electrolyte ion adsorption on WS_2 nanowire shells within the sub-nanometer physical gaps (van der Waals gaps) between the individual 2D layers, and (iv) high structural integrity because the core/shell and nanowire/current-collector interfaces were chemically self-assembled without any binder materials. Fig. 13(a) schematically demonstrates the synergistic effect of the "one-body" construction. This supercapacitor electrode exhibited a specific capacitance of 47.5 mF cm^{-2} at 5 mV s^{-1} in the voltage range of −0.3 V to 0.5 V *vs.* SCE in 1 M Na_2SO_4 (aq.) electrolyte through Na^+ ion-intercalation into the van der Waals gaps of 2D WS_2. The various valence states of W permit the following intercalation/deintercalation mechanism.

$$WS_2 + Na^+ + e^- \leftrightarrow WS\text{–}Na^+ \quad (44)$$

The durability test on this electrode showed an increment in the specific capacitance up to 74.25 mF cm^{-2} (@5 mV s^{-1}) during 2500 cycles due to the activation process, and a nearly constant value was maintained over the next 27 500 scans at a rate of 100 mV s^{-1}. Fig. 13(b–f) exhibit the electrochemical characterization (CV, rate capability, GCD, durability, and EIS, respectively) of the composite electrode. Moreover, a flexible solid-state supercapacitor was assembled with Na_2SO_4 gel electrolyte in a symmetric configuration, which delivered a specific capacitance and energy density of 18.3 mF cm^{-2} and 0.06 W h cm^{-3}, respectively, at 5 mV s^{-1} in the voltage window of 0–0.8 V. Patil and co-workers[202] prepared a lanthanum sulfide (La_2S_3) electrode *via* a low cost and room temperature chemical route, which was tested for application in supercapacitors in 1 M Na_2SO_4 electrolyte. The La_2S_3 electrode demonstrated the Na^+ ion-intercalation/deintercalation mechanism and showed a specific capacitance of 208 F g^{-1} (@1 mA cm^{-2}), energy density of 35 W h kg^{-1} (@1 mA cm^{-2}), power density of 1.26 kW kg^{-1} (@1 mA cm^{-2}), and moderate cycle life (78% capacitance retention over 1000 cycles @ 50 mV s^{-1}) in the voltage window of −1.1 to −0.3 V *vs.* SCE.

Although metal selenides are not widely utilized for pseudocapacitive applications, such as sulfides, a few reports are available in the literature. For example Peng *et al.*[203] fabricated an asymmetric supercapacitor based on petal-like cobalt selenide ($Co_{0.85}Se$) nanosheets as the positive electrode and nitrogen-doped porous carbon networks (N-PCNs) as the negative electrode in 2 M KOH electrolyte. The cobalt selenide showed two pairs of redox peaks in three-electrode CV at scan rates ranging from 5 to 30 mV s^{-1} in the voltage range of in the voltage range of −0.1 to 0.65 V *vs.* Hg/HgO due to the following pseudo-faradaic reactions.

$$Co_{0.85}Se + OH^- \leftrightarrow Co_{0.85}SeOH + e^- \quad (45)$$

$$Co_{0.85}SeOH + OH^- \leftrightarrow Co_{0.85}SeO + H_2O + e^- \quad (46)$$

The (+)$Co_{0.85}Se$//2 M KOH//N-PCN(−) full cell delivered a power density of 7947 W kg^{-1} (@13.2 W h kg^{-1}) and energy density of 21.1 W h kg^{-1} (@400 W kg^{-1}), together with good cycling stability (93.8% capacitance retention after 5000 cycles) in the voltage window of 0–1.6 V.

Different chemical supercapacitors based on various metallic compounds are elaborated herein from their historical origins to modern trends. Table 1 depicts a few additional representative examples of metallic compound-based supercapacitors. Furthermore, Fig. 14 demonstrates the comparative

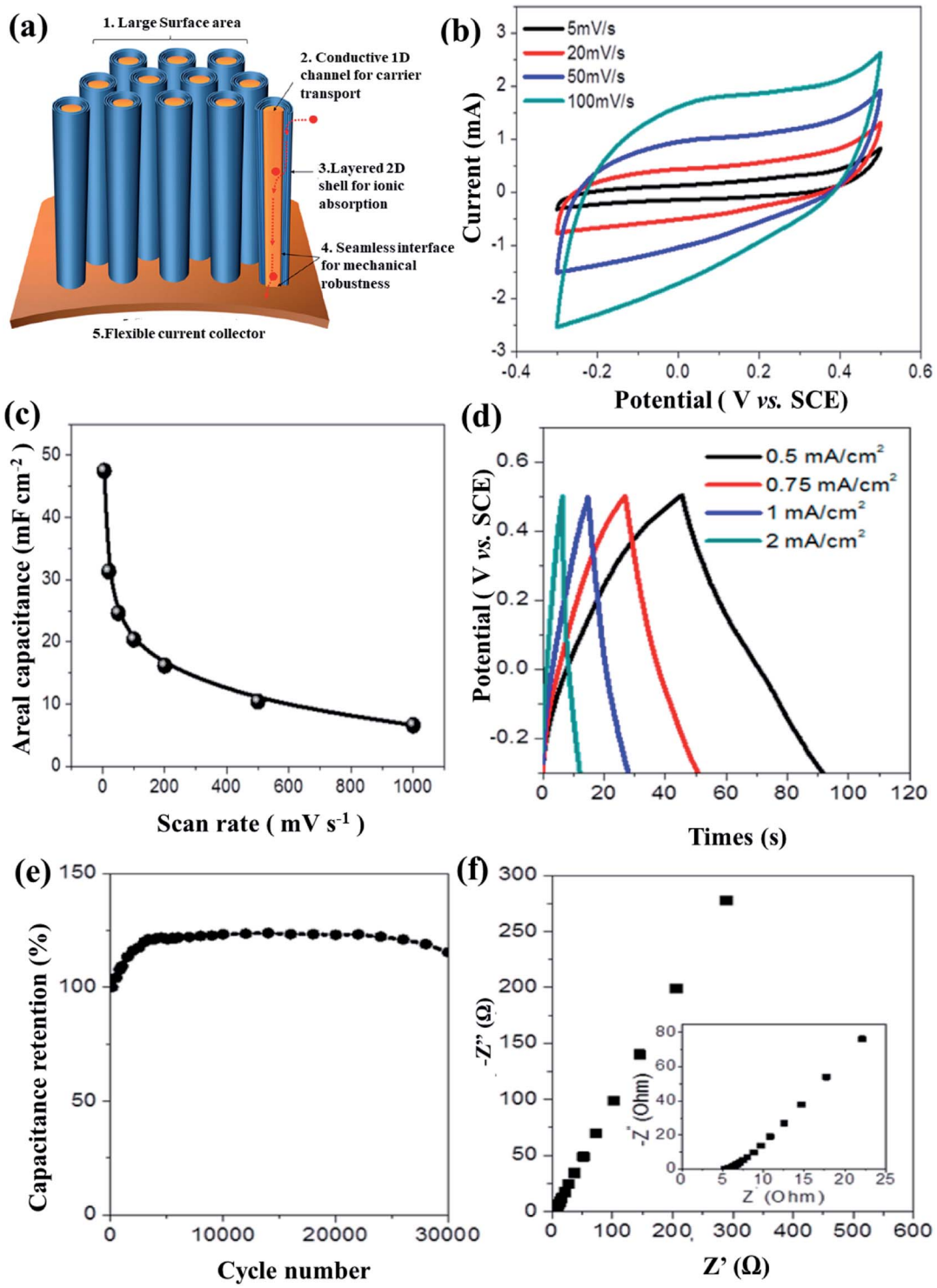

Fig. 13 (a) Schematic drawing of one-body array of core/shell nanowire electrode for supercapacitors. Functionalities of individual components are depicted in the schematic illustration. Electrochemical performances of the composite electrode: (b) CV profiles at different scan rates, (c) rate capability characteristics, (d) GCD profiles at different current densities, (e) cycling performance, and (f) Nyquist plot with corresponding zoomed-in image near $-Z'' = 0\ \Omega$. Figure reproduced from ref. 201 with permission Copyright (2016) from the American Chemical Society.

electrochemical performances of the state-of-the-art metallic compounds and composites for chemical supercapacitors. Indeed, metallic compounds are the most suitable candidates for practical chemical supercapacitors; however, the applications of some of these materials, *i.e.*, compounds of Ru, Ni, Co, Cr, Pb, Mo, W, and In, are restricted for commercial purposes due to their cost and toxicity. The compounds of Ti, Cu, Sn, Bi, *etc.* are considered green-materials, but considering

Table 1 Electrochemical performances of chemical supercapacitors based on various metallic compounds in the two-electrode cell assembly[a]

Sr. no.	Full cell (+)//(−)	Electrolyte	SC (F g^{-1})	[#]Current density or scan rate	Energy density (W h kg^{-1})/@power density (W kg^{-1})	Durability CR(%)/Cy no./current density or scan rate	Ref.
1	CuO//AC	3 M KOH	72.4	1 A g^{-1}	19.7/700	96/3000/15 mA cm^{-2}	204
2	MoO_3//AC	PVA–H_2SO_4 gel	145	2 mV s^{-1}	38.6/374.7	100/1500/10 A g^{-1}	205
3	SnO_2-QD//AC	PVA–H_2SO_4 gel	222	1 A g^{-1}	62/1000	85.8/3000/1 A g^{-1}	206
4	RuO_2//W_5O_{14}	0.5 M H_2SO_4	184.9	0.6 A g^{-1}	50.4/420 & 31.8/4901.8	78/8000/6 A g^{-1}	207
5	V_2O_5//V_2O_5	1 M Na_2SO_4	521	5 mV s^{-1}	247.9/497.1 & 43.2/ 39 900	90/4000/5 A g^{-1}	208
6	AC//Nb_2O_5	1 M Na_2SO_4	366	1 A g^{-1}	86/650 & 58/6500	99.9/3000/1 A g^{-1}	209
7	$NiWO_4$//AC	2 M KOH	71.1	0.25 A g^{-1}	25.3/200 & 15.1/4800	91.4/5000/1 A g^{-1}	210
8	MnO_2//V_2O_5	1 M Na_2SO_4	14.85 F cm^{-3}	1 mA cm^{-2}	8.25 mW h cm^{-3}/0.28 W cm^{-3} & 5.44 mW h cm^{-3}/1.12 W cm^{-3}	90.7/8000/40 mA cm^{-2}	211
9	$CoFe_2O_4$@MnO_2//AC	3 M KOH	103.86	5 mA cm^{-2}	37/470 & 15.3/4800	91.5/2250/41 mA cm^{-2}	212
10	$Zn_{0.7}Cu_{0.3}Co_2O_4$// $Zn_{0.7}Cu_{0.3}Co_2O_4$	PVA–KOH gel	175	3.5 A g^{-1}	55/2621 & 37/4629	72/5000/10 A g^{-1}	213
11	$Nd(OH)_3$//AC	6 M KOH	53	1 A g^{-1}	18.8/796	84/3000/1 A g^{-1}	214
12	K^+-doped-$Mn(OH)_4$//AC	3 M Na_2SO_4	399	0.4 A g^{-1}	41.38/143.3	107.3/6000/2 A g^{-1}	215
13	$Cd(OH)_2$//$Cd(OH)_2$	1 M NaOH	51	5 mV s^{-1}	11.09/799	117/1000/200 mV s^{-1}	216
14	CoFe hydroxides//AC	PVA–KOH	33.7	1 A g^{-1}	28.3/512 & 12.2/8784	81/1000/20 mV s^{-1}	217
15	SiC/$NiCo_2O_4$/$Ni(OH)_2$// SiC/Fe_2O_3	2 M KOH	242	4 A g^{-1}	103/3500 & 45/26 100	86.6/5000/9 A g^{-1}	218
16	SiC//SiC	1 M Na_2SO_4	72	1.43 A g^{-1}	31.43/2500 & 17.76/ 18 800	97.05/30 000/ 10.71 A g^{-1}	219
17	Ti_2CT_x//Ti_2CT_x	1 M KOH	220 F cm^{-3}	20 A g^{-1}	35 mW h cm^{-3}/0.49 W cm^{-3} & 17 mW h cm^{-3}/ 191 W cm^{-3}	100/3000/20 A g^{-1}	220
18	AC//Nb_2CT_x/CNT	1 M H_2SO_4	51	2 mV s^{-1}	16.5/375.2 & 10.1/7484.3	73.3/2000/5 A g^{-1}	221
19	Mo_2C/NCF//Mo_2C/NCF	PVA–KOH gel	75	0.5 A g^{-1}	54/1080 & 12/21 000	100/5000/5 A g^{-1}	222
20	RuO_2//$Ti_3C_2T_x$	1 M H_2SO_4	78	1000 mV s^{-1}	37 μW h cm^{-2} & 40 mW cm^{-2}	86/20 000/20 A g^{-1}	223
21	W_2N//W_2N	1 M H_2SO_4	80	1 mA cm^{-2}	12.92/646	[$]90.62/10 000/1, 5, 10 mA cm^{-2}	224
22	$NiCo_2N$@NG// NiFeN@NG	PVA–KOH gel	114 mA h g^{-1}	3 A g^{-1}	94.93/790	97.4/25 000/20 A g^{-1}	225
23	Ni_3N/rGO//DEG/rGO	6 M KOH	142.1	1 A g^{-1}	50.5/800 & 31.5/16 000	89.8/5000/5 A g^{-1}	226
24	Ni/Co–N//PC	1 M KOH	93.05	2 mA cm^{-2}	29.08/980 & 20.40/9850	82.4/5000/50 mV s^{-1}	227
25	NCFN@FG//AC	6 M KOH	163.3	1 A g^{-1}	56.3/374.6 & 39.5/7484.2	88.5/10 000/4 A g^{-1}	228
26	Graphene//Co_2P	6 M KOH	76.8	0.4 A g^{-1}	24/300 & 8.8/6000	97/6000/0.8 A g^{-1}	229
27	NiP//AC	2 M KOH	105	5 mV s^{-1}	29.2/400 & 11.8/8000	84.5/1000/20 mA	230
28	$NaNi_{0.33}Co_{0.67}PO_4 \cdot H_2O$// graphene	1 M KOH	95.52	0.5 A g^{-1}	29.85/374.95 & 24.37/ 7500	76.9/10 000/5 A g^{-1}	231
29	$Co_3(PO_4)_2 \cdot 8H_2O$//CuS	1 M KOH	163	2 mA cm^{-2}	58.12/1759 & 43.96/3517	94/3000/5 mA cm^{-2}	232
30	Co,doped-$Ni_{11}(HPO_3)_8(OH)_6$//AC	3 M KOH	77.4 mF cm^{-2}	1 mA cm^{-2}	15.48 mW h cm^{-2}/600 mW cm^{-2}	94/5000/2 mA cm^{-2}	233
31	$NiCo_2S_4$/NiS//AC	3 M KOH	123	1 mA cm^{-2}	43.7/160	94.8/3000/1 mA cm^{-2}	234
32	CoS_2//FeS_2	PAAS/KOH gel	151.5	1 A g^{-1}	64/271.2	91/5000/15 A g^{-1}	235
33	Ni_3S_4–MoS_2//AC	3 M KOH	120	1 A g^{-1}	58.43/385.95 & 18.75/ 7500	86.2/10 000/10 A g^{-1}	236
34	AC//$NiSe_2$	4 M KOH	104	1 A g^{-1}	44.8/969.7 & 17.4/17 200	87.4/20 000/5 A g^{-1}	237
35	$CoFe_2Se_4$–$CoNiSe_2$// $CoFe_2Se_4$–$CoNiSe_2$	3 M KOH	577.4	1 A g^{-1}	80.2/1000 & 75.8/9995.6	97.02/3000/5 A g^{-1}	238

[a] SC: specific capacitance; [#]SC (F g^{-1}) @ scan rate/current density; CR: capacitance retention; Cy: cycle number; QD: quantum dots; NCF: nitrogen-doped carbon flowers; DEG: diethylene glycol; NG: nitrogen-doped graphene; PC: porous carbon; NCFN@FG: NiCoFe-nitride@fluorinated graphene; PAAS: sodium polyacrylate; and [$]1 mA cm^{-2} for 1–2000 & 8000–10 000 cycles, 5 mA cm^{-2} for 2000–4000 & 6000–8000 cycles, 10 mA cm^{-2} for 4000–6000 cycles.

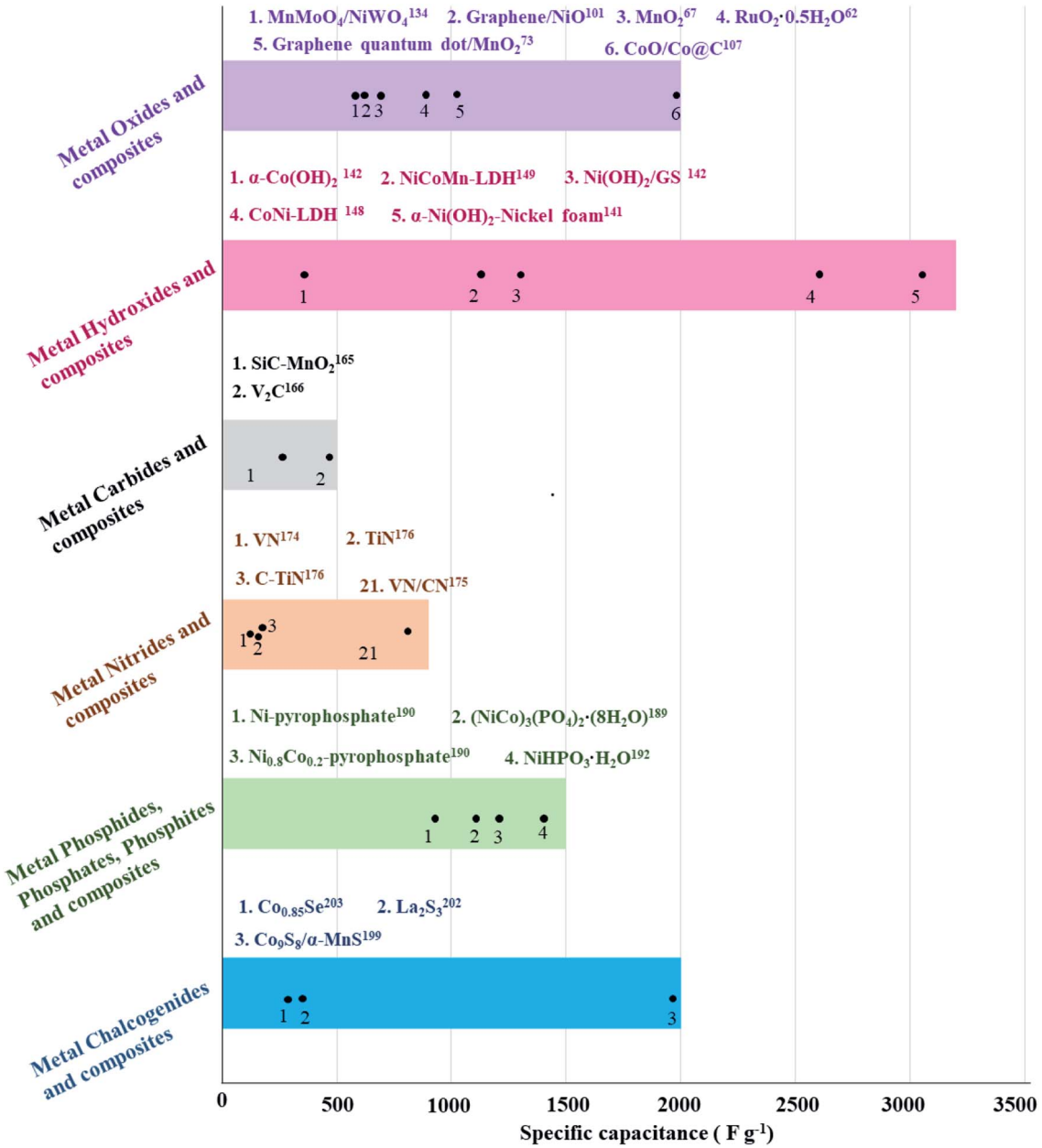

Fig. 14 Comparative electrochemical performances of the state-of-the-art metallic compounds and composites for supercapacitor applications.

the cost these materials, they have limited utility in commercial products. On the other hand, compounds of Mn, Fe, V, Zn, *etc.* are the most favourable for commercial devices due to their low cost and environmental-friendly nature.

5. Chemical supercapacitors based on conducting polymers

Way back in 1963, Weiss *et al.*[239–241] from Australia first reported the conductivity of conducting polymers (CP), and in the mid-1990s, the first CP-based supercapacitors were realized.[242–244] However a few years before, Gottesfeld (1987)[245] and Conway (1990)[246] first described the prospect of employing CPs in supercapacitors as pseudocapacitive materials. The conductivity of CP is attributed to the conjugated bond system throughout the polymer backbone. CPs can be synthesized *via* chemical or electrochemical oxidation/reduction of the monomers.[247,248] The oxidation/reduction of the monomer and polymer are accomplished with the insertion of dopants (counter ions).[249] CPs are p-doped during oxidation (dedoped at reduction) with counter anions, and n-doped during reduction (dedoped at oxidation) with counter cations, as follows:

$$\mathrm{CP} \leftrightarrow \mathrm{CP}^{n+}(\mathrm{A}^{-})_n + ne^{-}\ \text{(p-doping/dedoping)}\ [\mathrm{A}^{-}\text{: anion}] \quad (47)$$

$$CP + ne^- \leftrightarrow (C^+)_nCP^{n-}\ \text{(n-doping/dedoping)}\ [C^+\text{: cation}] \quad (48)$$

Among the various CPs (Fig. 15), PANI, PPy, PTh and derivatives of PTh are attractive for supercapacitive applications.[244,250] PANI and PPy are in the p-doped category, and n-doping is not possible due to the requirement of higher negative potentials, which limit the use of molecular solvent-based electrolytes.[251] The possible n-dopable materials are PTh and its derivatives. However, n-doping is not possible in PTh itself in acetonitrile (AN) solvent due its large negative potential (−2 V *vs.* Ag/AgCl), which is responsible for solvent breakdown.[252,253] Derivatives of PTh with 3-position substitution are n-dopable due to their more positive n-doping potential. Nevertheless, these n-doped CPs show lower conductivity and characterized by lower capacitance in this potential region. The physical and electrochemical properties of different CPs and p/n-doping characteristics of various PTh derivatives are shown in Tables 2 (ref. 247 and 254–256) and 3,[257] respectively.

CPs are attractive materials for supercapacitors due to their (i) pseudocapacitive properties, (ii) good conductivity, (iii) lower band-gap (1–3 eV) compare to conventional polymers (∼10 eV),[247] (iv) fast doping/dedoping processes, (v) suitable morphology, (vi) film-forming plastic properties, (vii) low cost, and (viii) environmental safety. In comparison to carbon-based EDLCs, CP-based supercapacitors exhibit a higher energy density (∼10 W h kg^{-1} *vs.* ∼5 W h kg^{-1}) due to pseudo-faradaic charge storage and lower power density (∼2 kW kg^{-1} *vs.* ∼4 kW kg^{-1}) because of the slower diffusion of ions into the bulk of the electrode.[258] The internal resistance, self-discharge rate and cycling stability are inferior in CP-based supercapacitors than

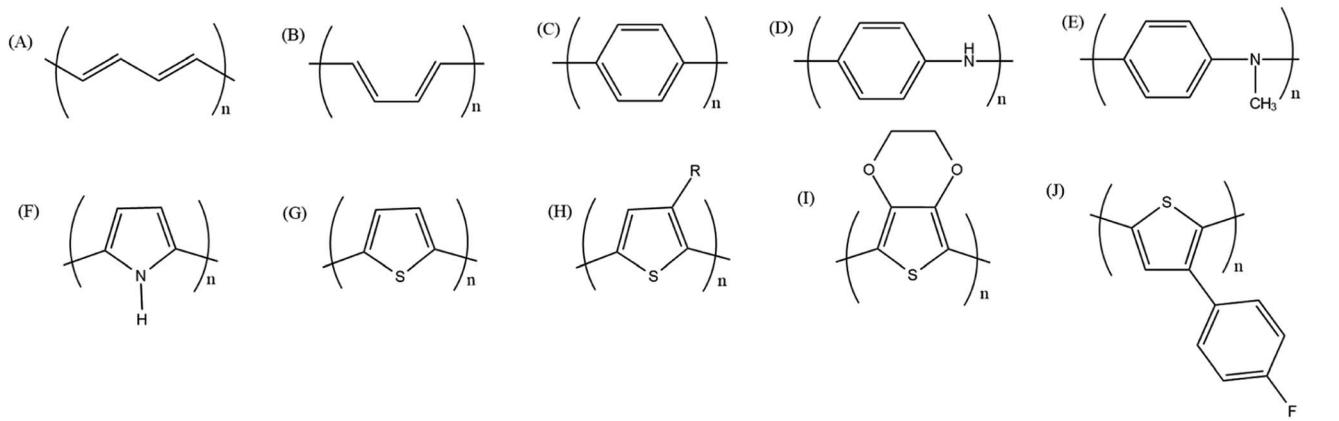

Fig. 15 Chemical structure of various conducting polymers: (A) *trans*-poly(acetylene), (B) *cis*-poly(acetylene), (C) poly(*p*-phenylene), (D) polyaniline (PANI), (E) poly(*n*-methylaniline) (PNMA), (F) polypyrrole (PPy), (G) polythiophene (PTh), (H) 3-substituted polythiophene, (I) poly(3,4-ethylenedioxythiophene) (PEDOT), and (J) poly(3-(4-fluorophenyl)thiophene) (PFPT).

Table 2 Physical and electrochemical properties of different conducting polymers

CP	[a]MW/g mol^{-1}	Dopant level	Voltage range/V	Conductivity/S cm^{-1}	Theoretical specific capacitance/F g^{-1}	Measured specific capacitance/F g^{-1} (ref. 254)
PANI	93	0.5	0.7	0.1–5 (ref. 255)	750	240
PPy	67	0.33	0.8	10–15 (ref. 256)	620	530
PTh	84	0.33	0.8	300–400 (ref. 247)	484	—
PEDOT	142	0.33	1.2	300–500 (ref. 247)	210	92

[a] MW: molecular weight per unit monomer (g mol^{-1}).

Table 3 The p- and n-doping of various polythiophene (PTh) derivatives[a257]

	p-Doping		n-Doping	
CP	Voltage limit/V *vs.* SCE	Capacitance/F g^{-1}	Voltage limit/V *vs.* SCE	Capacitance/F g^{-1}
PFPT	−0.2 to 1.0	95	−1.7 to −1.0	80
PDTT	−0.2 to 1.0	110	−1.5 to −0.2	75
PMeT	−0.2 to 1.15	220	−2.0 to −1.0	165

[a] PDTT: poly(ditheno(3,4-*b*:3′,4′-*d*)thiophene), PMeT: poly(3-methyl thiophene).

carbon-based EDLCs. Additionally, supercapacitors with the EDLC mechanism demonstrate more than half million of charge/discharge cycles, whereas CP-based devices start to degrade before a thousand cycles due to the disintegration of their polymeric network structures upon repetitive intercalation/deintercalation (doping/dedoping) of ions.[258,259] High energy density is achieved in CP-based devices by increasing the doping level, which accelerates the structural degradation through the higher extent of doping/dedoping, resulting in a volume change.[260] Hence, simultaneously achieving high energy density and long cycle life in pristine CP-based supercapacitors is not trivial. CP-based devices in ILs display superior cyclic performances.[261,262] Nevertheless, the improvement of the operational life for CP-based devices can be possible by increasing the robustness of their polymeric moieties. A smart way to accomplish this is by designing composite electrodes by combining CPs with carbonaceous materials (AC, CB, graphite, graphene, CNTs, CNFs, GO, rGO, *etc.*) and metallic compounds (oxides, hydroxides, carbides, nitrides, chalcogenides, *etc.*).[244,250] Composite electrodes have been synthesized not only to combine the properties of individual materials, but also to achieve a synergistic effect as a whole. Therefore, a prolonged operational life along with higher energy density can be achieved in CP-based systems. The opportunities and challenges of CP-based chemical supercapacitors are reviewed below.

5.1. Polyaniline and composites

Fig. 16 shows the three redox states of PANI, namely, fully reduced leucoemeraldine, partially oxidized emeraldine, and fully oxidized pernigraniline.[263] Among the three states, emeraldine salt is conducting and electrochemically active, while the other two states are insulating even after protonation. In practice, a mixture of three states is present in the PANI electrode, and best electrochemical performance is expected when the proportion of emeraldine salt is the highest. The synthesis of PANI can be carried out *via* the oxidation of aniline monomers either *via* chemical or electrochemical routes.[264] In the chemical oxidation method, different morphologies, such as nanofibers, nanorods, nanotubes, nanoflakes, nanospheres, and nanoflowers, can be achieved through the accurate control of oxidants or/and addition of additives.[265] On the other hand, the electrochemical method is fast and free of oxidants or additives. Using this method, binder-free film electrodes are fabricated on conducting substrates,[248] but only limited morphologies, such as nanofibers, nanogranules and thin films can be achieved.

In the early 2000s, Ryu *et al.*[266] reported an $LiPF_6$-doped PANI electrode in a two-electrode symmetric supercapacitor with 1 M Et_4NBF_4/AN electrolyte, which demonstrated a decline in specific capacitance from 100 to 70 F g^{-1} over 5000 cycles at 2 mA cm^{-2} in the voltage window of 0–1 V. In another study,[255] the same group reported PANI-HCl (H-doped) and PANI-$LiPF_6$ (Li-doped) electrodes for symmetric supercapacitors in 1 M Et_4NBF_4/AN electrolyte. PANI-HCl showed an initial capacitance of 70 F g^{-1}, which degraded to 40 F g^{-1} within ~400 cycles and then remained stable up to 1000 cycles at 1.25 mA cm^{-2} in the voltage window of 0.1–1.0 V. On the other hand, under the same operating conditions, PANI-$LiPF_6$ exhibited an initial capacitance of 107 F g^{-1}, which decreased to 84 F g^{-1} after 9000 cycles. In 2002, Park and Park[260] developed an alkaline aqueous asymmetric supercapacitor with the (+)PANI//6 M KOH//AC(−) configuration, which showed a specific capacitance of 380 F g^{-1} (@0.5 mA cm^{-2}), energy density of 18 W h kg^{-1} (@0.5 mA cm^{-2}) and power density of 1.25 kW kg^{-1} (@20 mA cm^{-2}) in the voltage window of 1–1.6 V. The device exhibited excellent

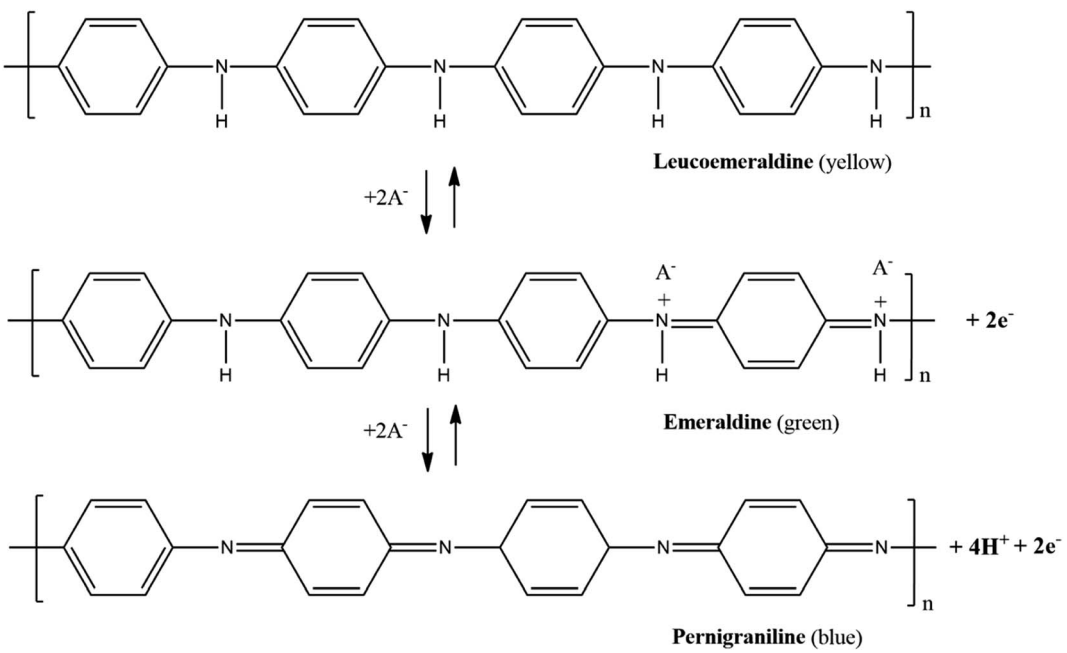

Fig. 16 Three redox forms of PANI: fully reduced leucoemeraldine, partially oxidized emeraldine and fully oxidized pernigraniline.

cycling stability, *i.e.*, ~20% loss of initial capacitance in the first 300 cycles, and thereafter maintained a steady capacitance of up to 4000 cycles at 50 mV s^{-1} in the voltage window of 0.8–1.6 V. In 2004, Sivakkumar and Saraswathi[267] reported PANI-derivatives, namely, poly(*n*-methyl aniline) (PNMA), for energy storage systems. Due to the blocking the proton exchange sites by the methyl group, this polymer showed greater chemical stability and superior redox activity. The (+)PNMA//Li(−) device with 1 M $LiClO_4$ in ethylene carbonate/dimethyl carbonate (EC/DMC) electrolyte achieved a capacity of 52 mA h g^{-1} at 100 μA cm^{-2} in the voltage window of 2.5–3.6 V. In 2005, Zhou and co-workers[268] electrochemically polymerized aniline on an SS substrate *via* the pulse galvanostatic method (PGM) and galvanostatic method (GM) in 0.5 M H_2SO_4 electrolyte. Herein, the authors demonstrated different morphologies of PANI and their performances by altering the electrodeposition methods. Eventually, the nanofibrous morphology was achieved by PGM, while GM provided a granular morphology. The experimental results indicate the superior performances of the nanofibrous PANI compared to the granular morphology because of the larger surface area and ionic conductivity of the former. The symmetrical supercapacitor based on nanofibrous PANI in 1 M $NaClO_4$/1 M $HClO_4$ (aq.) electrolyte delivered a specific capacitance of 609 F g^{-1} (@1.5 mA cm^{-2}), energy density of 26.8 W h kg^{-1} (@1.5 mA cm^{-2}) and moderate cycling performance (12% capacitance loss after 1000 cycles @ 2.5 mA cm^{-2}) in the voltage window of 0–0.75 V. In 2009, Li *et al.*[269] firstly estimated the theoretical mass specific capacitance of PANI by considering the EDLC and pseudocapacitive effects, and compared it with experimental data. The maximum specific capacitance was calculated to be 2.0×10^3 F g^{-1} by assuming 100% of the PANI is oxidized or reduced in the charge/discharge processes. The PANI nanofiber-deposited SS electrodes in 1 M H_2SO_4 electrolyte were used for CV (in three-electrode cell), EIS (in three-electrode cell) and GCD (in two-electrode cell) analysis to determine the experimental specific capacitance of PANI. Consequently, the specific capacitances achieved were 608, 445, and 524.9 F g^{-1} in CV, EIS and GCD, which are only 30%, 22% and 26% of the theoretical value, respectively. This mismatch indicates the lower utilization of PANI in the charge/discharge operations. The lower extent of PANI utilization is attributed to the slower diffusion of dopants (counter anions) and the conductivity of PANI. In reality, the dopants can intercalate/deintercalate in/from the outer surface of the PANI fiber (shell) at an appreciable rate, but the slower diffusion is unavoidable in the inner core of fiber due to the inaccessibility of the dopants. On the other hand, the conductivity of PANI regulates the electron transfer rate and influences the extent of the redox reaction. Therefore, designing an advanced morphology (capable of fast ion diffusion) and improving the electrode conductivity may increase the experimental specific capacitance of PANI. As an example of an advance morphology design, Wang *et al.*[270] developed vertically aligned PANI nanowire arrays on an Au substrate, and tested its performance in

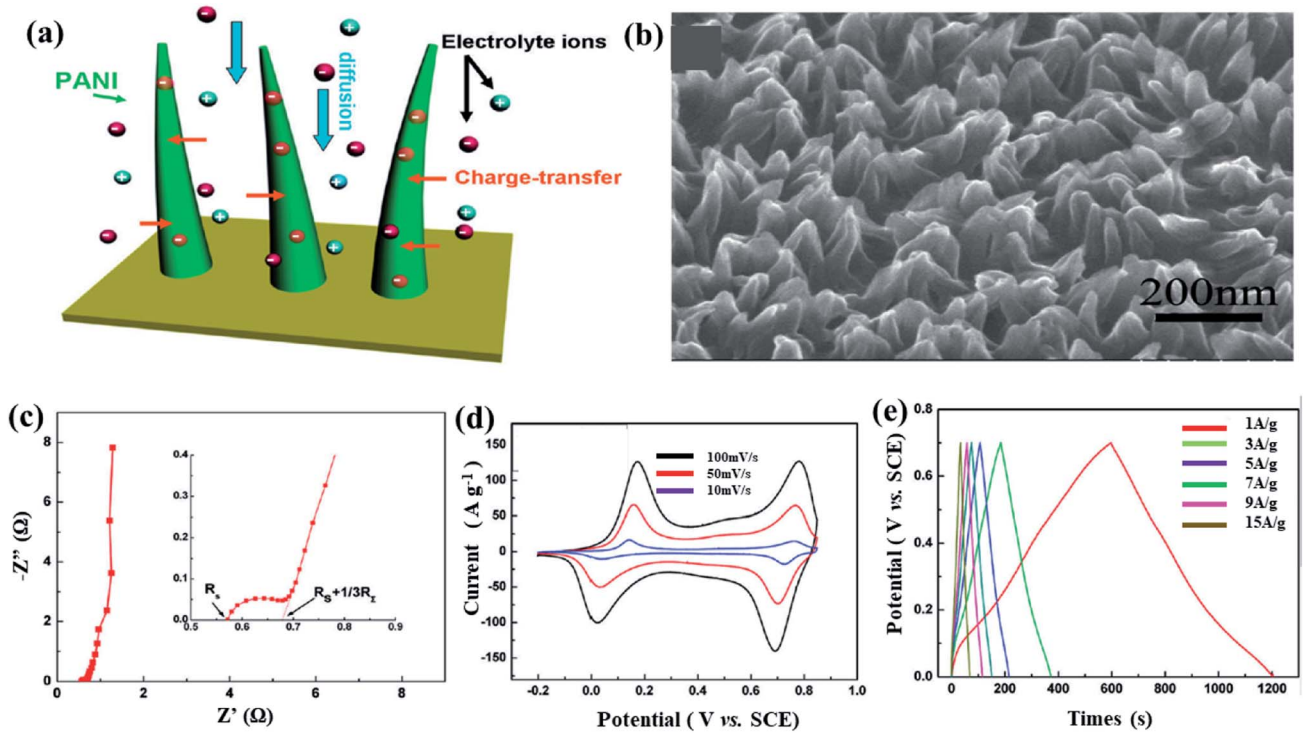

Fig. 17 (a) Schematic illustration of electrolyte ion diffusion pathways in vertically aligned PANI nanowire arrays and (b) SEM image of PANI nanowire arrays. (c) Nyquist plot in the frequency range of 20 kHz to 1 Hz (the inset is an enlarged curve of the high frequency region). (d) CV profiles at different scan rates and (e) GCD profiles at several current densities. Figure reproduced from ref. 270 with permission Copyright (2010) from the American Chemical Society.

1 M $HClO_4$ (aq.) electrolyte in a three-electrode cell configuration. The as-prepared vertical arrays of PANI nanowires (Fig. 17(a and b)) with narrow diameters (~50 nm) facilitated fast ion diffusion under supercapacitive operations. The Nyquist plot in EIS (Fig. 17(c)) showed the solution resistance, ion diffusion resistance and charge transfer resistance of 0.6, 0.39 and 0.12 Ω, respectively, which indicate the fast kinetics of the PANI nanowire array electrode. Fig. 17(d and e) depict the CV and GCD profiles, respectively, for the PANI nanowires. However, the PANI electrode exhibits a specific capacitance of 950 F g^{-1} (@1 A g^{-1}), an energy density of 130 W h kg^{-1} (@700 W kg^{-1}), a power density of 28 000 W kg^{-1} (@100 W h kg^{-1}) and moderate cycling stability (16% capacitance loss at 300 cycles followed by 6% capacitance loss in subsequent 400 cycles @ 20 A g^{-1}) in the voltage range of 0–0.7 V *vs.* SCE.

Beyond the pure PANI electrode, binary composites including PANI/carbon or PANI/metallic compounds are promising candidates for supercapacitors. Liu *et al.*[271] synthesized a SWCNT/PANI (core/shell) composite through *in situ* electrochemical polymerization cycles in 1 M H_2SO_4 medium. In this process, a free-standing SWCNT/PANI composite was prepared, where PANI was deposited on SWCNT bucky paper and generated a tubular structure with a diameter of about 50–100 nm. The composite electrode prepared by 90 polymerization cycles demonstrated the highest specific capacitance of 501.8 F g^{-1} at 5 mV s^{-1} in the voltage range of 0–0.75 V *vs.* SCE, which increases up to 706.7 F g^{-1} by 5 cycles of controlled electrodegradation. The off-laying disordered PANI was dissolved and polycrystalline PANI regions were exposed to the electrolyte by controlled electrodegradation, which is responsible for the improved capacitance. However, the overall higher capacitance value achieved here is due to the synergism between SWCNT and PANI. Specifically, π–π interactions exist between the π-bonded surface of the SWCNT and the conjugated structure of PANI, which control the morphology of PANI deposited. On the other hand, the SWCNT network acts as a template and accelerates the nucleation/growth kinetics of PANI. Moreover, the strong π–π interactions increase the coefficient of charge transfer from the PANI redox active sites to SWCNTs, and thus the utilization of active material becomes maximum. This synergistic effect is attributed to improving the electrochemical performances of the SWCNT/PANI composite compared to the individual component. Lu and co-workers[272] synthesized highly ordered 3D α-Fe_2O_3@PANI core–shell nanowire arrays through a simple cost effective electrodeposition method (Fig. 18(a)), and assembled a (+)PANI@CC//1 M Na_2SO_4 (aq.)//α-Fe_2O_3@PANI(−) asymmetric device (Fig. 18(b)). This asymmetric device delivered a specific capacitance of 2.02 mF cm^{-3} (@5 mV s^{-1}), energy density of 0.35 mW h cm^{-3} (@120.51 mW cm^{-3}) and excellent cycling performance (95.77% capacitance retention over 10 000 cycles @ 50 mV s^{-1}) in the voltage window of 0–1.5 V. Fig. 18(c–e) presents the CV profiles of the individual electrode, full cell CV and full cell GCD, respectively, for the asymmetric device. This superb electrochemical performance of the asymmetric device is ascribed to the hierarchical 3D core–shell nanowire arrays of PANI/α-Fe_2O_3, which provide a large redox active surface area, fast ion and electron transfer with good structural stability. Zhang *et al.*[273] synthesized a PANI/$Ni(OH)_2$ composite *via* a two-step

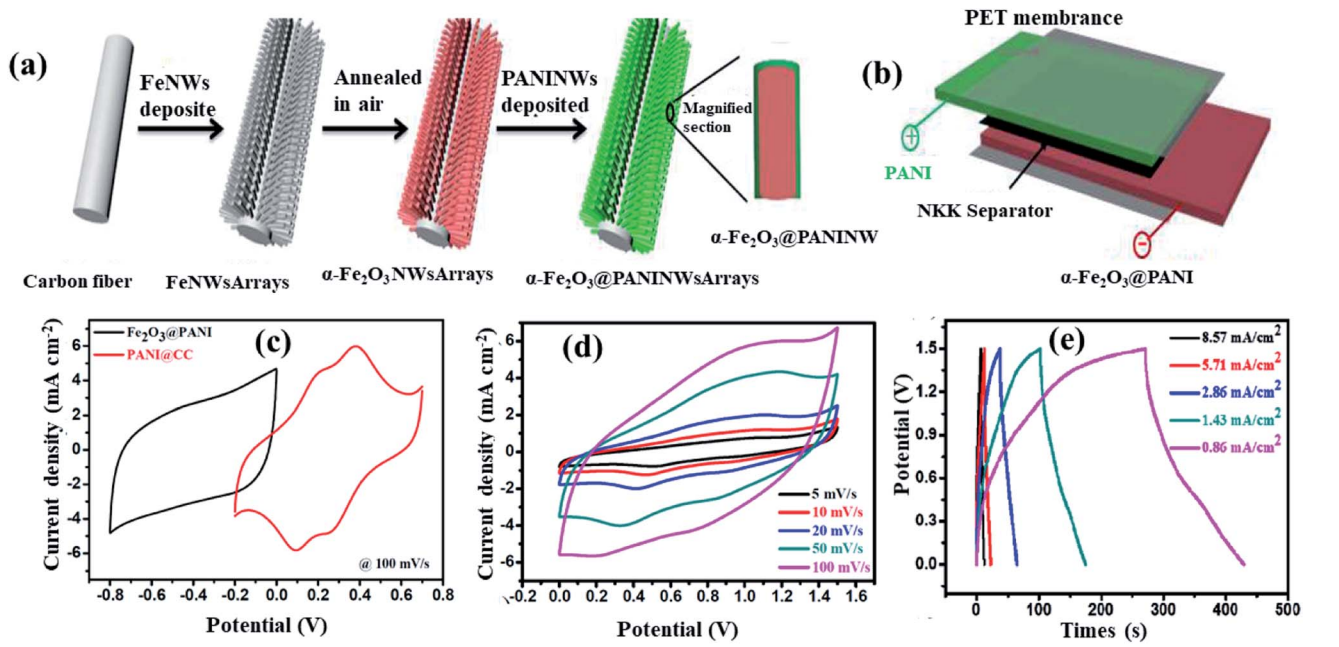

Fig. 18 (a) Schematic illustration of the preparation of α-Fe_2O_3@PANI core–shell nanowires (NWs). (b) Structure of asymmetric device with two electrodes separated by the TF45 (NKK) membrane (separator). (c) Individual CV profiles of the α-Fe_2O_3@PANI and PANI electrodes at 100 mV s^{-1} in a three-electrode system. Electrochemical characteristics of the asymmetric device: (d) CV profiles at different scan rates; and (e) GCD profiles at different current densities. Figure reproduced from ref. 272 with permission Copyright (2015) from the American Chemical Society.

hydrothermal route, where 1D fiber-like PANI was decorated with 3D flower-like $Ni(OH)_2$. In this synthetic route, PANI acted as a crystal growth modifier for $Ni(OH)_2$, and hence, the β- to α-phase conversion of $Ni(OH)_2$ was accomplished. Therefore, the morphology of was $Ni(OH)_2$ converted from nano-plate to 3D flower-like structure, which facilitated the charge transfer kinetics and improved the contacts between $Ni(OH)_2$ and PANI. Consequently, the utilization of the active material improved drastically. The PANI/$Ni(OH)_2$ composite electrode showed a good specific capacity (55.50 C g^{-1} @ 0.5 mA cm^{-2}), high rate capability (74.18% capacity retention from 0.5 to 2.5 mA cm^{-2}) and moderate cycle life (79.49% capacity retention after 2500 cycles @ 1.5 mA cm^{-2}) in the voltage range of −0.5 to 0.5 V *vs.* SCE in 0.5 M Na_2SO_4 (aq.) electrolyte. Zhu and co-workers[274] demonstrated a facile way to produce a multi-component architecture by combining thin MoS_2 nanosheets and PANI nanoneedle arrays *via* an ice-reaction process. This binary PANI/MoS_2 composite provided a high surface area (114 m^2 g^{-1}, whereas 10 and 75 m^2 g^{-1} for branched PANI and exfoliated MoS_2, respectively), good electrical conductivity and fast ionic diffusion, which led to higher energy and power densities. The PANI/MoS_2-based symmetric device with 0.5 M H_2SO_4 electrolyte delivered specific capacitances of 669, 821 and 853 F g^{-1} at 1 A g^{-1} in the voltage window of ±0.6, ±0.8 and ±1.0 V, respectively, which are higher than that of the pristine PANI (capacitance: 397, 457 and 433 F g^{-1}) and exfoliated MoS_2 (capacitance: 250, 322 and 341 F g^{-1}), respectively. Furthermore, the device displayed 91% capacitance retention after 4000 cycles at 10 A g^{-1} within the window of ±0.6 V. The composite electrode achieved enhanced performances due to the following advanced features: (i) thin MoS_2 nanosheet facilitates ion diffusion and the interlayer acts as an ion reservoir, (ii) the PANI nanoneedle allows the effective insertion of proton into the bulk and improves the electron transport, (iii) its flexible structure easily accommodates the volume change, which is associated with proton intercalation/deintercalation, and (iv) nanostructuring reduces the diffusion length of the electrolyte ions, and hence, high power capability is expected.

Ternary composites including PANI, carbonaceous materials, and metallic compounds open a new direction for next-generation chemical supercapacitors. As an example, Das *et al.*[275] synthesized a PANI/MoO_3/graphene nanoplate ternary composite (PMG) *via* the *in situ* polymerization of aniline in the presence of MoO_3 and graphene nanoplatelets (GNP). The morphological analysis through SEM and TEM demonstrated a fibrillar PANI coating on the MoO_3/GNP composite. The measured surface area for the pristine PANI, GNP, PANI/GNP and PMG was 91.698, 148.089, 113.331 and 78.055 m^2 g^{-1}, with the corresponding total pore volume of 1.460, 0.477, 0.937 and 0.543 cm^3 g^{-1} at $P/P_0 = 0.999341$, respectively. The as-prepared PMG composite was semiconductor in nature, which was identified by its non-linear current–voltage characteristics. Additionally, the conductivity values of PANI, PANI/GNP and PMG were estimated to be 1.940×10^{-5}, 1.605×10^{-4} and 1.216×10^{-4} S m^{-1}, respectively, from the current–voltage profiles. This result indicates that highly conducting GNP improves the conductivity of the PANI/GNP composite compared to the pristine PANI, while, nonconducting MoO_3 decreases the conductivity of PMG compared to that PANI/GNP to a small extent. The specific capacitances of PANI, PANI/GNP and PMG were estimated to be 295, 442 and 593 F g^{-1}, respectively, at 1 A g^{-1} in the voltage window of −0.3 to 0.8 V *vs.* Hg/Hg_2SO_4 in 1 M H_2SO_4 electrolyte. The highest specific capacitance of the PMG composite over PANI and PANI/GNP is primarily attributed to the higher extent of pseudocapacitive reactions in the MoO_3 component. The PMG composite delivered the energy and power densities of 99.68 W h kg^{-1} (@1 A g^{-1}) and 1678.99 W kg^{-1} (@3 A g^{-1}), respectively. The PMG electrode showed greater cycling stability (92.4% capacitance retention after 1000 cycles at 1 A g^{-1}) compared to the PANI (85.84%) and PANI/GNP composite (89.37%). The EIS analysis revealed that the PMG composite showed the lowest charge transfer resistance compared to the pristine PANI and PANI/GNP composite, which is due to excellent synergistic effect in the ternary composite.

5.2. Polypyrrole and composites

PPy is an important CP for supercapacitor electrodes due to its advantages, including easy synthesis, great flexibility, high capacitance and good cycling stability. The density of PPy is high, and consequently high volumetric capacitances (400–500 F cm^{-3}) are expected.[276] However, slow ion diffusion in the bulk of the electrode is unavoidable due to its dense polymeric structure, which limits the gravimetric capacitances (250–350 F g^{-1}) especially for a thicker coating on electrodes.[250] PPy is generally doped with single-charged anions (Cl^-, ClO_4^-, SO_3^-, *etc.*), but doping with multi-charged anions, such as SO_4^{2-}, creates cross-linked polymers.[249] Suematsu *et al.*[249] mentioned that high diffusivity and high capacitance are expected from cross-linked PPy due to its greater porosity in the polymeric growth. However, this group reported the volumetric capacitance of 100–230 F cm^{-3} in the electrode potential range of −0.6 to 0.4 V *vs.* Ag/AgCl, which are much lower than that typically reported (400–500 F cm^{-3}) for dense PPy electrodes. In 2003, Iroh and Levine[277] reported the improved charge storage properties of PPy by polyimide (a dopant with high molecular weight) doping, which is due to the protection of PPy from oxidative degradation by the polyimide matrix. It is noteworthy that PPy is anodically electroactive and polyimide is cathodically electroactive. The authors analysed the capacitance characteristics of the PPy/polyimide electrode in 0.01 M KPF_6/AN electrolyte through an EIS study, where the anode and cathode capacitances were in the range of about 1.5–1.9 mF and 1.5–0.4 mF in the voltage range of 0–0.9 V and 0–1.2 V *vs.* SCE, respectively. In 2015, Yang *et al.*[278] synthesized free-standing PPy films *via* oil/water interfacial polymerization in the presence of surfactants. The morphology of the PPy films depended on the choice of surfactant, for example, porous and vesicular structures were obtained using Tween80 and Span80 surfactants, respectively. Moreover, lowering the polymerization temperature resulted in more and smaller pores or vesicles in the PPy film structures. The PPy films polymerized at 0 °C with Tween80 showed a specific capacitance of 261 F g^{-1} at 25 mV

s^{-1} in the voltage range of 0–0.6 V *vs.* SCE. By keeping the other parameters the same, the specific capacitance was observed to be 149 F g^{-1} when polymerization occurred at 25 °C. This result is attributed for the following reasons: the PPy films with smaller pores (polymerization @ 0 °C) provided higher conductivity than that with larger pores (polymerization @ 25 °C), and their respective conductivity values were 4.7 and 3.5 S cm^{-1}, respectively. However, the optimized PPy film electrode (polymerized at 0 °C with Tween80) exhibited good cycling stability, such as 75% capacitance retention after 1000 cycles at 25 mV s^{-1}. Intrinsic PPy flexible films were prepared by Li and Yang[279] *via* a chemical oxidation method with a methylorange–$FeCl_3$ reactive self-degradable template. Morphological analysis by SEM and TEM confirmed the nanotubular structure of PPy with a diameter of 50–60 nm and length of 5–6 μm when the molar ratio of $FeCl_3$ to monomer was 0.5. The PPy films exhibited a specific capacitance of 576 F g^{-1} at 0.2 A g^{-1} in the voltage range of 0–0.7 V *vs.* SCE in 1 M KCl (aq.) electrolyte and retained 82% of its initial capacitance after 1000 cycles at 3 A g^{-1}. The EIS study demonstrated a lower ESR (0.75 Ω) and charge-transfer resistance (8.9 Ω) of the PPy films, which are the key for fast ion diffusion and improved conductivity of the electrodes. In 2016, Rajesh *et al.*[280] deposited phytic acid-doped PPy films on Ti and SS substrates *via* an electropolymerization method. Fig. 19(a and b) show the chemical structure of phytic acid and phytic acid-doped PPy chain, respectively. The specific capacitance and energy density of the PPy films on Ti achieved were 343 F g^{-1} and 47.64 W h kg^{-1}, respectively, at 5 mV s^{-1} within −0.2 to 0.8 V *vs.* Ag/AgCl in 1 M H_2SO_4 electrolyte. Under similar conditions, PPy films on SS showed the specific capacitance and energy density of 297 F g^{-1} and 41.25 W h kg^{-1}, respectively. Moreover, these PPy film-based electrodes retained 77% and 91% initial capacitance after 4000 cycles at 10 A g^{-1} for Ti and SS substrates, respectively. However, based on the above discussion, it is evident that the microstructure of PPy and its electrochemical performances are greatly influenced by several factors, such as synthesis method, template, dopant, and substrate. Thus, the optimization of these factors may improve the supercapacitive performances of pristine PPy-based electrodes. Nevertheless, investigations on PPy composites with carbonaceous materials and metallic compounds are truly indispensable.

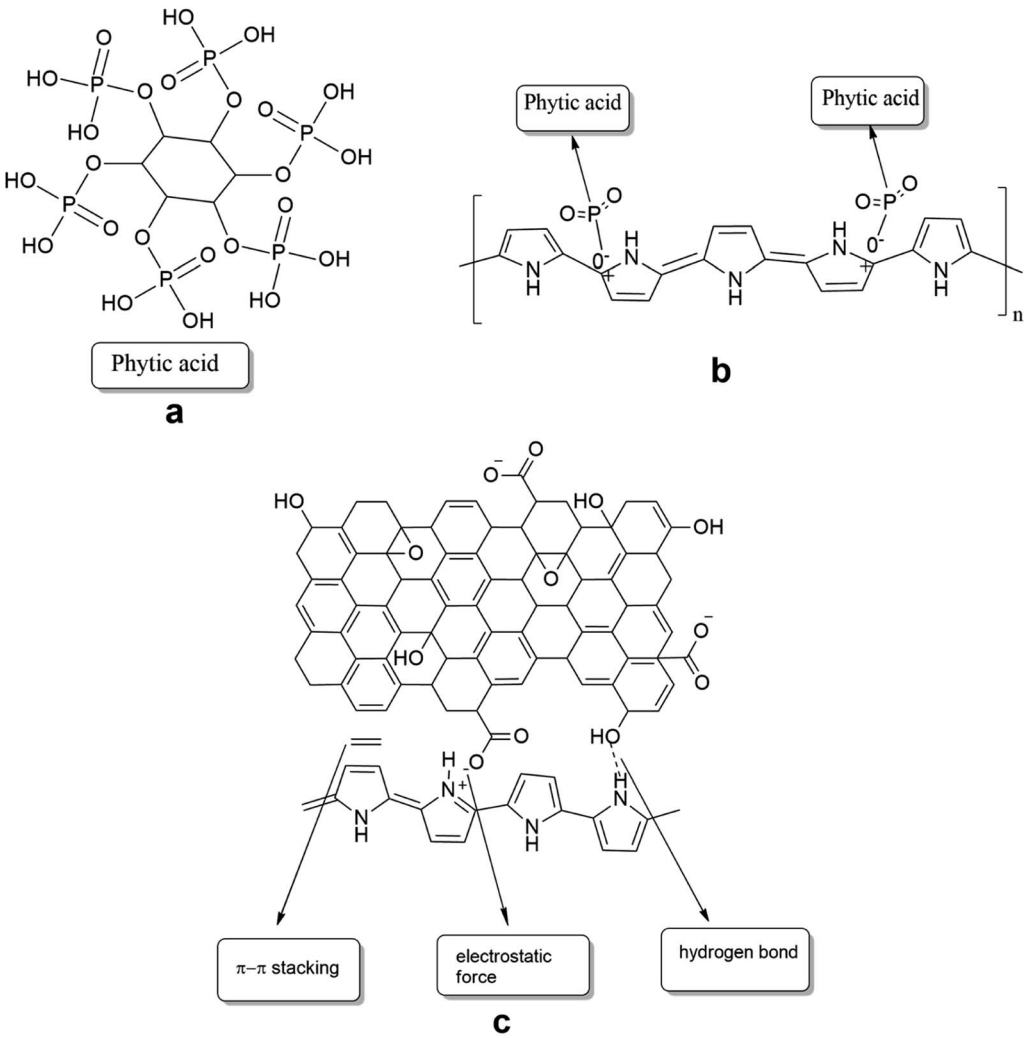

Fig. 19 Chemical structure of (a) phytic acid, (b) phytic acid-doped PPy, and (c) PPy/GO assembly.

A novel core–shell PPy/GO nanocomposite with uniform PPy nanospheres was synthesized by Wu *et al.*[281] through an *in situ* surface-initiated polymerization method. PPy nanospheres (~70 nm) were uniformly grown on GO sheets, which formed a continuous core–shell composite structure. In the composite structure, the possible interactions between PPy and GO are π–π stacking, hydrogen bonding and electrostatic forces, as demonstrated in Fig. 19(c). Furthermore, the composite electrodes were electrochemically tested through EIS, GCD and CV in 1 M H_2SO_4 electrolyte. The EIS study showed lower resistive characteristics for the PPy/GO composite (R_s: 1.81 Ω and R_{ct}: 0.07 Ω) compare to that of pristine PPy (R_s: 2.04 Ω and R_{ct}: 0.11 Ω). In the Nyquist plot, PPy/GO showed a more perpendicular line in the lower frequency region than PPy, which implies the better capacitive behaviour with faster ion diffusion in PPy/GO. Due to its improved resistive behaviour, the PPy/GO composite showed a better specific capacitance of 370 F g^{-1} than that of the pristine PPy (216 F g^{-1}) at 0.5 A g^{-1} in the voltage range of −0.2 to 0.8 V *vs.* SCE. The cycling stabilities of the PPy/GO and PPy electrodes were demonstrated as 91.2% and 57.8% capacitance retention over 4000 CV scans at 100 mV s^{-1}, respectively. The mechanically robust GO impeded the structural degradation of PPy upon repetitive cycling, and hence, improved durability was achieved. Besides employing carbonaceous nanostructures (such as graphene, GO, rGO, CNT, CNF, *etc.*) in PPy composites, PPy/AC,[282] PPy/graphite sheets,[283] PPy/CC,[284] *etc.* are also attractive supercapacitive materials considering large scale production with lower cost. On the other hand, Zhou and co-workers[285] developed well-aligned PPy/CoO hybrid nanowires grown on 3D nickel foam, where PPy was uniformly immobilized or strongly anchored on the surface of the CoO nanowires. The well-aligned mesoporous hybrid nanowires facilitated fast ion migration towards the bulk due to the shorter diffusion pathways through the ordered structures. In 3 M NaOH medium, the composite electrode showed a high specific capacitance of 2223 F g^{-1} (*vs.* 1212 F g^{-1} for pristine CoO) at 1 mA cm^{-2} in the voltage window of −0.2 to 0.5 V *vs.* Ag/AgCl with good cycling stability (99.8% capacitance retention after 2000 cycles at 20 mA cm^{-2}). An asymmetric device (+)PPy/CoO@Ni//3 M NaOH//AC@Ni(−) was fabricated, which delivered an energy density of 43.5 W h kg^{-1} (@87.5 W kg^{-1}), power density of 5500 W kg^{-1} (@11.8 W h kg^{-1}) and excellent cycling performance (91.5% capacitance retention after 20 000 cycles at 25 mA cm^{-2}) in the voltage window of 0–1.8 V. Zhu *et al.*[286] improved the electrochemical performances of PPy films by intercalating them into the interlayer spacing of layered-Ti_3C_2 (l-Ti_3C_2). The homogeneous l-Ti_3C_2 MXene particles were synthesized *via* selective HF-etching of the Al layer in the Ti_3AlC_2 MAX phase and electrophoretically deposited on a fluorine-doped tin oxide (FTO) substrate, and subsequently PPy films were successfully intercalated into l-Ti_3C_2 *via* electrochemical polymerization. Fig. 20(a and b) demonstrate the

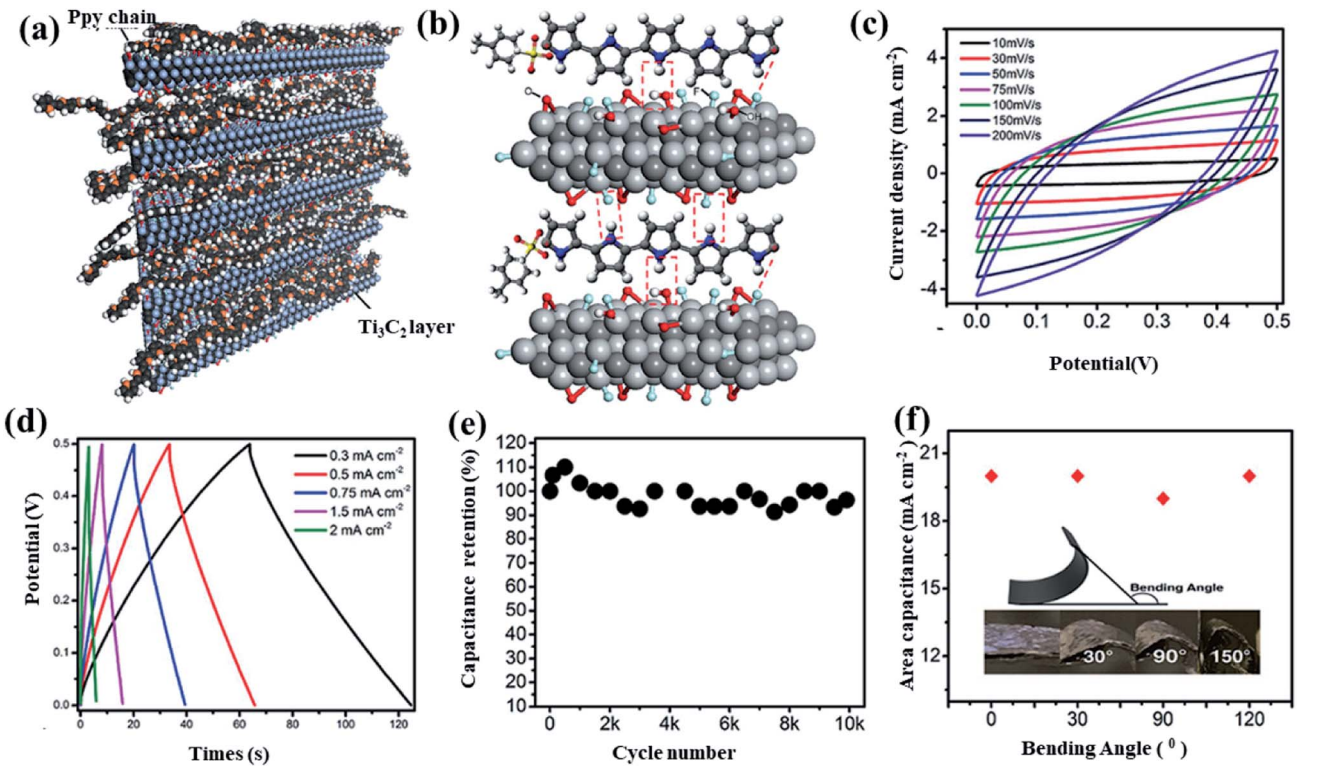

Fig. 20 (a) Schematic drawing of intercalated PPy films in the interlayers of l-Ti_3C_2 and (b) atomic-scale magnification of intercalated PPy films in the interlayers of l-Ti_3C_2. The red dashed rectangles in (b) mark the hydrogen bonds between the N–H groups of the pyrrole rings and the oxygen or fluorine containing terminal groups on the surface of Ti_3C_2. Electrochemical characteristics of the solid-state symmetric device: (c) CV profiles at different scan rates, (d) GCD profiles at different current densities, (e) cycling performances, and (f) performance under bending conditions. Figure reproduced from ref. 286 with permission Copyright (2016) from WILEY-VCH Verlag GmbH & Co. KGaA, Weinheim.

structural characteristics of the PPy/l-Ti_3C_2 composite films, where PPy films are sandwiched between layers of Ti_3C_2. The capacitance of the PPy/l-Ti_3C_2 films achieved was 203 mF cm^{-2} (*i.e.*, 406 F cm^{-3}), which is ~35% higher than that of the pristine PPy film (150 mF cm^{-2}; 300 F cm^{-3}) in 0.5 M H_2SO_4 electrolyte at 1 mA cm^{-2} in the voltage range of 0–0.5 V *vs.* SCE. Moreover, the composite films showed no capacitance loss after 20 000 cycles at the abovementioned current density and voltage window, while the pristine PPy films exhibited ~30% capacitance loss. The improved performances of the composite films are ascribed to the following reasons: (i) dense stacking of PPy is prevented by the distributed l-Ti_3C_2 particles, which boosts the electrolyte infiltration; (ii) the strong interactions between the PPy backbone and Ti_3C_2 surface increase the structural stability of the composite film; and (iii) the intercalated structure improves the diffusion kinetics of charge-carrier transportation. A symmetric solid-state supercapacitor device was assembled, which delivered an energy density of 10 mW h cm^{-3} (@500 mW cm^{-3}) and splendid cycling stability (no capacitance loss after 10 000 cycles @ 0.5 mA cm^{-2}) in the voltage window of 0–0.5 V. Fig. 20(c–e) shows the CV, GCD and cycle life profiles, respectively, for the symmetric full cell. The flexibility of the solid-state device was tested at different bending and relaxed states, which showed no performance variation (Fig. 20(f)). Liu *et al.*[287] fabricated a flexible asymmetric supercapacitor device using graphene foam (GF)/CNT/MnO_2 as the positive electrode and GF/CNT/PPy as the negative electrode in 0.5 M Na_2SO_4 (aq.) electrolyte. The GF/CNT/MnO_2 positive active material was prepared *via* the hydrothermal method, where MnO_2 was deposited on the GF/CNT film. On the other hand, the GF/CNT/PPy negative active material was synthesized *via* the chemical polymerization route. Fig. 21(a) presents the individual CV profiles of the positive and negative electrodes in the voltage window of 0.0–1.0 V and −0.6 to 0.2 V *vs.* Ag/AgCl, respectively. The CV profiles demonstrated the ideal pseudo-faradaic charge storage mechanism for both the positive and negative electrodes. The asymmetric device delivered an energy density of 22.8 W h kg^{-1} (@860 W Kg^{-1}) and a power density of 2700 W kg^{-1} (@6.2 W h kg^{-1}) together with moderate cycling performances (83.5% capacitance retention after 10 000 cycles @ 1.5 mA cm^{-2}) in the voltage window of 0–1.6 V regime. Fig. 21(b–d) provide the characteristics features of the CV, GCD and flexibility (bending) tests for the asymmetric device. Moreover, two full cells connected in series could illuminate three LEDs (1.8 V, 20 mA and 5 mm diameter) after charging for 30 s (Fig. 21(e)).

Zhou and co-workers[288] developed a ternary composite with PPy, CNT and MnO_2, where PPy modified the CNT-surface before encapsulation by MnO_2, and constructed a 3D uniform core–shell nanostructure of CNT–MnO_2. In the 3D hierarchical CNT@PPy@MnO_2 composite, PPy acted as the glue and improved the adhesion between CNT and MnO_2, leading to the high cycling stability of composite electrodes. Moreover, the core–shell CNT@PPy@MnO_2 nanostructures decreased the contact resistance in the electrode/electrolyte and achieved

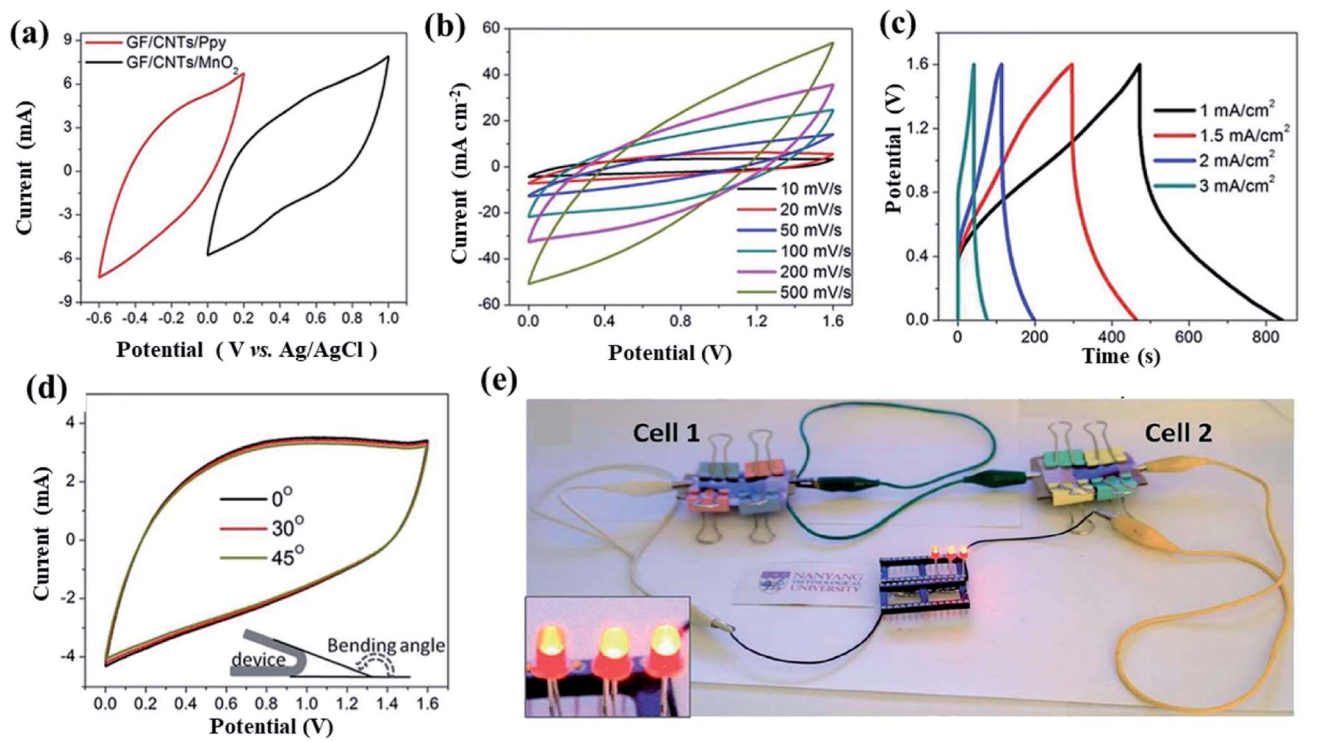

Fig. 21 (a) Individual CV profiles of GF/CNT/MnO_2 and GF/CNT/PPy half cells in 0.5 M Na_2SO_4 (aq.) electrolyte at scan rate of 20 mV s^{-1}. (b) CV profiles of asymmetric device at different scan rates. (c) GCD profiles of asymmetric device at different current densities. (d) CV profiles of flexible asymmetric device at different bending angles and (e) optical image showing two full cells connected in series powering LEDs. Figure reproduced from ref. 287 with permission Copyright (2014) from The Royal Society of Chemistry.

a higher surface area. The specific capacitances of CNT@PPy@MnO_2 and CNT@MnO_2 were determined to be 529.3 and 293.4 F g^{-1} at 0.1 A g^{-1} in the voltage window of 0–1 V *vs.* Ag/AgCl in 1 M Na_2SO_4 (aq.) electrolyte, respectively. In the Nyquist plots, CNT@PPy@MnO_2 and CNT@MnO_2 showed inclination angles of about 60° and 35°, respectively, implying the better capacitive behaviour of the ternary composite than the binary composite. The resistive components were also lower in the ternary composite (R_s: 2.8 Ω) than the binary composite (R_s: 3.2 Ω). These superior results for CNT@PPy@MnO_2 are mainly attributed to the fast charge transfer through the PPy linker and fast ion transfer in the ordered 3D hierarchical nanostructures. The CNT@PPy@MnO_2 electrode exhibited a capacitance retention of ~98.5%, which is much better than that of CNT@MnO_2 (79.6%) at 5 A g^{-1} for 1000 cycles. A symmetric device [(+)CNT@PPy@MnO_2//1 M Na_2SO_4 (aq.)// CNT@PPy@MnO_2(−)] and an asymmetric device [(+) CNT@PPy@MnO_2//1 M Na_2SO_4 (aq.)//AC(−)] were assembled and their performance tested. The symmetric device delivered an energy density of 9.34 W h kg^{-1} (@100 W kg^{-1}), power density of 5000 W kg^{-1} (@5.56 W h kg^{-1}) and good cycle life (87.2% capacitance retention after 2000 cycling @ 5 A g^{-1}) within 1–2 V operating window. It is noteworthy that the binary CNT@MnO_2 composite-based symmetric device showed only 73.7% capacitance retention under similar operating conditions. On the other hand, the asymmetric device demonstrated an energy density of 38.42 W h kg^{-1} (@100 W kg^{-1}), power density of 30 000 W kg^{-1} (@11.11 W h kg^{-1}) and good cycling stability (89.7% capacitance retention over 2000 cycling @ 5 A g^{-1}) in the voltage window of 1–2 V. Further, the flexibility of the asymmetric device was tested through repetitive CV scans at 50 mV s^{-1}, and the result indicates 64.74% capacitance retention after 200 bending (180°) cycles, which recommends appreciable bending stability for flexible operations. Xie and Wang[289] developed a ternary PPy/TiN/PANI coaxial nanotube hybrid *via* the successive loading of PPy and PANI onto a TiN nanotube array through an electropolymerization route. The pulse voltammetric (0.7 to 1.1 V *vs.* SCE) electrodeposition method was applied for synthesizing the binary PPy/TiN nanotube hybrid, while, aniline was electropolymerized on the PPy/TiN nanotubes *via* CV (−0.2 to 1.1 V *vs.* SCE) scans. Here, p-doped PPy and n-doped PANI were smartly integrated with a conducting TiN nanotube substrate as a ternary composite. The specific capacitances observed were 1471.9, 744.8 and 846.1 F g^{-1} for PPy/TiN/PANI, PPy/TiN and PANI/TiN, respectively, at 0.5 A g^{-1} in the voltage window of −2 to 0.6 V *vs.* SCE in 1 M H_2SO_4 electrolyte. The higher capacitance of the ternary nanotube hybrid compared to both binary systems is attributed due to the synergistic effect of PPy and PANI. A poor cycling performance was observed for PPy/TiN/PANI, *i.e.*, 78%, 46.3% and 38.8% capacitance retention after 200, 500 and 1000 cycles at 10 A g^{-1}, respectively. The authors believed that the exfoliation of PANI films and the electrochemical corrosion of TiN in the experimental medium were responsible for its low durability. An all-solid-state symmetric device with the PPy/TiN/PANI composite in H_2SO_4/ethylene glycol (EG)/PVA gel electrolyte was assembled and the device delivers a specific capacitance of 288.4 F g^{-1}, energy density of 129.8 W h kg^{-1} and power density of 0.9 kW kg^{-1} at 1 A g^{-1} in the voltage window of 0–1.8 V. Furthermore, at a current density of 20 A g^{-1}, the values of 187.5 F g^{-1}, 84.4 W h kg^{-1} and 18 kW kg^{-1}, respectively, which indicate its excellent power capability.

5.3. Polythiophene, polythiophene-derivatives and composites

Tables 3 (ref. 257) and 4 (ref. 290) present the electrochemical properties of different p- and n-doped PTh derivatives, and it can be observed that the n-dopable forms deliver a lower specific capacitance than the p-dopable forms, which is mainly due to their lower conductivity. Hence, the applications of n-dopable forms in the negative electrodes of full cells are truly limited. Very few instances are available in the literature, where n-doped PTh or its derivatives were used in negative electrodes. In 1995, Arbizzani *et al.*[291] assembled a symmetric supercapacitor based on PDTT in tetraethylammonium tetrafluoroborate ($TEABF_4$)/propylene carbonate (PC) electrolyte, where p- and n-doped polymers were used as the positive and negative active materials, respectively. The EIS study demonstrated that the specific capacitance of p-doped PDTT is 106.4 mF cm^{-2} at 1.26 MHz, but the n-doped form exhibited only 43.2 mF cm^{-2} at the same frequency. Moreover, n-doped PTh is not stable in air and moisture, while p-doped PTh is quite stable. Consequently, n-doped PTh showed high self-discharge (tendency to oxidize back to the neutral state) and low cycling stability. Thus, to overcome the abovementioned factors, PTh derivatives with a lower band-gap (*i.e.*, n-doping potential becomes less negative) can be designed. The substitution of 3-position in the thiophene ring with phenyl, ethyl and alkoxy groups improves the stability towards air and moisture.[292] The electron withdrawing groups attached with these substitutions further improve the stability of n-doped PTh derivatives.

Table 4 Electrochemical properties of polythiophene (PTh)-derivatives in p-doped state[a][290]

CP	Voltage/V *vs.* Ag/AgCl	Voltammetric charge/C g^{-1}	Specific capacitance/F g^{-1}
P-PFPT	0.3 to 0.9	146	244
P-MPFPT	0.3 to 0.9	127	212
PThCNVEDT	0 to 0.8	173	216
PEDOT	−0.5 to 0.9	144	103

[a] P-MPFPT: poly(3-(3,4-difluorophenyl)thiophene) and PThCNVEDT: poly(1-cyano-2-(2-(3,4-ethylenedioxylthienyl))-1-(2-thienyl)vinylene).

Fig. 15(H) depicts the general structure of 3-substituted PTh derivatives.

Among the various derivatives of PTh, PEDOT has remarkable prospects in CP-based supercapacitors[244,247] due to its (i) low oxidation potential, (ii) wide potential window, (iii) low band-gap (1–3 eV) and highly conducting p-doped state (300–500 S cm^{-1}), (iv) good thermal and chemical stabilities, (v) high charge mobility and fast electrochemical kinetics, and (vi) good film forming property. However, PEDOT has a high molecular weight with lower doping level, and thus delivers a low specific capacitance (Table 2). Lota *et al.*[247] reported a specific capacitance of 180 F g^{-1} for a PEDOT thin film, but the value for a pellet (10–20 mg) was reported to be 80–100 F g^{-1}. In 2004, Ryu and co-workers[293] designed symmetric [(+)PEDOT//PEDOT(−)] and asymmetric [(+)PEDOT//AC(−)] supercapacitors with Et_4NBF_4-PC and $LiPF_6$-EC/DMC electrolytes and tested their performance in the voltage windows of 0–1 V and 0–3 V. In the window of 0–1 V, the symmetric device with Et_4NBF_4-PC and $LiPF_6$-EC/DMC electrolyte showed the specific capacitances of 22 and 27 F g^{-1} at 0.25 mA cm^{-2} after 1000 cycles, respectively. In contrast, that for the asymmetric device was 19 and 50 F g^{-1}, respectively. Similarly, in the voltage window of 0–3 V, the symmetric device exhibited specific capacitances of 20 and 13 F g^{-1} and the asymmetric device delivered 30 and 56 F g^{-1} for the Et_4NBF_4-PC and $LiPF_6$-EC/DMC electrolytes, respectively. PFPT is another promising CP for supercapacitor applications. Laforgue *et al.*[294] reported the fabrication of (+)PFPT//1 M NEt_4BF_4-PC//AC(−) asymmetric devices using 4 and 60 cm^2 electrodes for the test cells and industrial prismatic prototypes, respectively. The test cells delivered the maximum energy density of 48 W h kg^{-1} ($E_{max} = \frac{1}{2}CV_{max}^2$; C = capacitance, and V_{max} = maximum voltage in operating window) and maximum power density of 9 kW kg^{-1} ($P_{max} = V^2/4R$; V = starting discharge voltage excluding ohmic drop, and R = internal resistance) in the voltage window of 1.2–3.0 V window, while the industrial prototypes exhibited the values of 7.5 W h kg^{-1} and 250 W kg^{-1} in the voltage window of 1–3 V, respectively. The initial 2000 F capacitance of the industrial prototype dropped to 1000 F within the first 100 cycles, and remained stable up to 8000 cycles at 5 A current in the voltage window of 1–3 V. Another important PTh derivative is PMeT, and Arbizzani *et al.*[295] developed a (+) PMeT//1 M Et_4NBF_4-PC//AC(−) asymmetric supercapacitor, which showed a specific capacitance of 39 F g^{-1} (@5 mA cm^{-2}), energy density of 30 W h kg^{-1} (@500 W kg^{-1}) and power density of 1810 W kg^{-1} (@19 W h kg^{-1}) in the voltage window of 1–3 V. Pristine PTh and its derivatives show poor supercapacitive performances, and thus it is hard to realize practical devices with these inferior active materials. Accordingly, composite materials can overcome the intrinsic shortcomings of pristine polymers and provide much superior energy materials.

A binary composite of PTh with MWCNTs was prepared by Zhang *et al.*[296] *via* electropolymerization in an oil-in-IL microemulsion, where MWCNTs were homogeneously encapsulated by PTh with a thickness of 2–3 nm. The PTh/MWCNT composite with an interlaced framework morphology was electrochemically characterized in 1 M Na_2SO_4 (aq.) solution by constructing a three-electrode cell assembly. The quasi-rectangular CV at a scan rate of 50 mV s^{-1} in the voltage window of −0.6 to 1 V *vs.* Ag/AgCl indicates the pseudocapacitive behaviours of the PTh/MWCNT composite. Moreover, a higher current response (2.63 A g^{-1}) was observed for PTh/MWCNT compared to the pristine PTh (1.08 A g^{-1}) and pristine MWCNT (1.75 A g^{-1}). Notably, the nucleation and growth of PTh in the oil/IL microemulsion were controlled in such a way that the PTh films were interwoven with the MWCNTs. Consequently, an open framework structure was achieved, which is beneficial for fast ionic transportation. The fast diffusion kinetics together with high surface area and electrical conductivity improved the electrochemical current response in the composite material compared to that of its pristine components. The specific capacitance achieved for the composite material was 216 F g^{-1} with the charge loading of 300 mC at a current density of 1 A g^{-1} in the voltage window of −0.6 to 1 V *vs.* Ag/AgCl, which dropped to below 160 F g^{-1} after 500 repetitive cycles under the same operations. Alabadi and co-workers[297] developed GO/PTCB and graphite/PTCB (PTCB: poly[(thiophene-2,5-diyl)-*co*-(benzylidene)]) composites through non-covalent interactions (van der Waals forces or hydrogen bonds) between PTCB and GO or graphite sheets. The PTCB-modified GO or graphite sheets showed pores and wrinkles surfaces, which enhanced the electrochemically active surface area and the supercapacitive performances. The room temperature electrical conductivity of the GO/PTCB and graphite/PTBC composites was reported to be 33 and 1 S cm^{-1}, respectively, which were much greater than that of the pristine PTh (0.167 S cm^{-1}).[298] However, the specific capacitances of GO/PTCB and graphite/PTCB were 296 and 217 F g^{-1}, respectively, at 0.3 A g^{-1} in the voltage window of −1 to 0 V *vs.* Ag/AgCl window in 2 M KOH electrolyte. The capacitance retention of 91.86% and 75.56% after 4000 cycles at 0.3 A g^{-1} was observed for the GO/PTCB and graphite/PTCB composites, respectively. The GO/PTCB composite delivered an energy density of 148 W h kg^{-1} (@41.6 W kg^{-1}) and power density of 24.8 kW kg^{-1} (@102 W h kg^{-1}) in the abovementioned voltage window. In 2001, Hong *et al.*[299] prepared an RuO_x-deposited PEDOT electrode *via* a dipping-hydrolysis and electrolysis method. The CV and EIS studies depicted that the composite electrode operated under both non-faradaic and pseudo-faradaic mechanisms, and consequently, a high specific capacitance was achieved compared to pristine PEDOT. The optimized composite structure showed a specific capacitance of 420 F g^{-1} at 50 mV s^{-1} in the voltage window of 0–1 V *vs.* SCE in 0.5 M H_2SO_4. The symmetric cells based on PEDOT and PEDOT/RuO_x stored specific capacities of 12.4 and 27.5 mA h g^{-1}, respectively, when the cells were charged in the voltage range of 0–1 V at a current in the range of 100 to 400 mA cm^{-2}. Interestingly, the increase in current density (100–400 mA cm^{-2}) did not reduce the stored capacities. Moreover, the stored energy densities were calculated to be 12.4 and 27.5 W h kg^{-1}, respectively, for the PEDOT and PEDOT/RuO_x-based cells. Ambade and co-workers[300] synthesized a PTh/TiO_2 nanocomposite *via* the controlled electropolymerization of thiophene on TiO_2 nanotubes (TNTs). This synthetic scheme allowed the thiophene monomers to infiltrate into the

Table 5 Electrochemical performances of chemical supercapacitors based on conducting polymers in two-electrode cell assembly[a]

Sr. no.	Full cell (+)//(−)	Electrolyte	SC (F g^{-1})	#Current density or scan rate	Energy density (W h kg^{-1})/@power density (W kg^{-1})	Durability CR(%)/Cy no./current density or scan rate	Ref.
1	PANI//MoO_3	1 M H_2SO_4	518	0.5 A g^{-1}	71.9/254 & 38.9/2500	78/1000/3 A g^{-1}	301
2	Ti_2CT_x/PANI// graphene	1 M H_2SO_4	94.5	1 A g^{-1}	42.3/950 & 25/18 000	94.2/10 000/10 A g^{-1}	302
3	HPC/PANI//HPC	1 M Na_2SO_4	134	1 A g^{-1}	60.3/18 000 & 26/18 000	91.6/5000/1 A g^{-1}	303
4	ACF–PANI//AC	0.5 M H_2SO_4	61	0.5 A g^{-1}	20/2100	90/1000/500 mA g^{-1}	304
5	ACTBs//PANI–ACTBs	1 M H_2SO_4	154	1 A g^{-1}	42/699	86/10 000/20 A g^{-1}	305
6	$NiCo_2S_4$/PANI//AC	PVA–KOH gel	152	1 A g^{-1}	54.06/790 & 15.9/27 100	84.5/5000/8 A g^{-1}	306
7	PANI–$CuCo_2O_4$//AC	1 M KOH	367.5 C g^{-1}	0.4 A g^{-1}	76/599 & 46/3011	94/3000/0.8 A g^{-1}	307
8	NiCoLDHs@CNT/NF//APDC/NF	1 M KOH	210.9	0.5 A g^{-1}	89.7/456.8 & 41.7/8700	78/1200/1 A g^{-1}	308
9	PANI/NiO/SGO//AC	PVA–KOH gel	308.8	1 A g^{-1}	109.8/800 & 39.5/8000	91.5/10 000/1 A g^{-1}	309
10	sGNS/cMWCNT/PANI//aGNS	1 M H_2SO_4	107	1 A g^{-1}	41.5/167 & 20.5/25000	91/5000/1 A g^{-1}	310
11	PPy//PPy	PVDF-HFP–EC/PC (1 : 1), 1 M $LiClO_4$	137	0.12 mA cm^{-2}	19/380 & 15.6/350	100/5000/100 mV s^{-1}	311
12	AC//Ni_3S_2@PPy/NF	2 M KOH	46.39	2.5 mA cm^{-2}	17.54/179.33 & 8.67/3587.41	100/3000/30 mA cm^{-2}	312
13	PEDOT//PPy–GO	Li_2SO_4/PVA	29.8	0.2 mA cm^{-2}	2.98 mW h cm^{-2}/0.12 mW cm^{-2}	99.3/10 000/200 mV s^{-1}	313
14	PPy-NTs//N-CNTs	1 M H_2SO_4	109	1.43 A g^{-1}	28.98/998.56	89.98/2000/1.43 A g^{-1}	314
15	PPy@rGOH//rGOH	PVA–KNO_3 gel	131.8	4 A g^{-1}	46.9/800 & 28.6/2400	94.6/10 000/4 A g^{-1}	315
16	NCO–PPy//AC	2 M KOH	128.3	0.4 A g^{-1}	45.6/362 & 23/3949	85/5000/0.8 A g^{-1}	316
17	PPy/FeO@CVO//GNP	1 M KOH	140.5	1 A g^{-1}	38.2/700 & 22.5/2099	95/5000/1 A g^{-1}	317
18	GNP/SWNTs/PPy//GNP/SWNTs/PPy	PVA–H_2SO_4	324	0.5 A g^{-1}	28.8/1975.22	91/5000/1 A g^{-1}	318
19	CoFeLDH–PPy/GO//AC	PVA–KOH	116 C g^{-1}	1 A g^{-1}	25.7/2800	83.5/10 000/10 A g^{-1}	319
20	PPy/GO/MnO_2//PPy/GO/MnO_2	1 M Na_2SO_4	786.6	25 mV s^{-1}	52.3/1392.9	86.1/1000/100 mV s^{-1}	320
21	PProDOT//CMK-3	$EMIM^+N(CF_3SO_2)_2^-$/PC	294 mF cm^{-2}	0.44 mA cm^{-2}	0.16 mW h cm^{-2}/0.86 mW cm^{-2} & 0.11 mW h cm^{-2}/3.98 mW cm^{-2}	98/5000/2.5 mA cm^{-2}	321
22	PEDOT//PEDOT	1 M H_2SO_4	203	5 mV s^{-1}	4.40/200 & 3.12/40250	86/12 000/10 A g^{-1}	322
23	PTh/50% Al_2O_3//PTh/50% Al_2O_3	PVA–KOH gel	472.8	1 A g^{-1}	58.04/533.02	90.54/5000/100 mV s^{-1}	323
24	CNFs/PEDOT/MnO_2//AC	1 M KCl	148.07	0.3 A g^{-1}	49.4/224.02	81.06/8000/150 mV s^{-1}	324
25	Charcoal//PTHA	PVA–KOH gel	265.14	2 A g^{-1}	42.0/735.86 & 17.70/1276.9	94.6/2000/20 mV s^{-1}	325
26	PTh//C-PTh	6 M KOH	252	5 mV s^{-1}	54.6/1700	93/2000/1 A g^{-1}	326
27	PEDOT-PSS/rGO/Eco//PEDOT-PSS/rGO/Eco	PVA/H_2SO_4	82.4	0.1 A g^{-1}	11.4/131.5 & 4/3947.4	84.4/5000/0.25 A g^{-1}	327
28	Poly(3-methylthiophene)//AC	1 M Et_4NBF_4/PC	35	5 mA cm^{-2}	31/900	99.9/20 000/20 mA cm^{-2}	328
29	e-PTh/Ti-wire//e-PTh/Ti-wire	PVA/H_2SO_4	55.71 mF cm^{-2}	2 μA	23.11 μW h cm^{-2}/90.44 μW cm^{-2}	97/3000/2 μA	329
30	PANI/Au/PEN//PEDOT/Au/PEN	PVA/H_2SO_4	34 F cm^{-3}	0.5 mA cm^{-2}	9 mW h cm^{-3}/2.8 W cm^{-3}	80/10 000/2 mA cm^{-2}	330

[a] SC: specific capacitance; #SC (F g^{-1}) @ scan rate/current density; CR: capacitance retention; Cy: cycle number; HPC: hierarchically porous carbons; ACF: activated carbon fibre; ACTB: activated carbon tube bundles; APDC: activated polyaniline derived carbon; SGO: sulfonated graphene; sGNS: sulfonated graphene nanosheet; cMWCNT: carboxylated multiwalled carbon nanotube; PVDF-HFP: polyvinylidene fluoride-*co*-hexafluoropropylene; rGOH: rGO hydrogel; NCO: $NiCo_2O_4$ nanowires; CVO: cobalt vanadium oxide hydrate; GNP: graphene nanoplate; PProDOT: poly(3,4-propylenedioxythiophene); CMK-3: ordered mesoporous carbon; $EMIM^+N(CF_3SO_2)_2^-$: 1-ethyl-3-methylimidazolium bis(trifluoromethylsulfonyl) imide; PTHA: polythiophene/aluminium oxide; C-PTh: carbonaceous PTh; PEDOT-PSS: poly(3,4-ethylenedioxythiophene)-poly(styrenesulfonate); Eco: Ecoflex™ silicone; Et_4NBF_4: tetraethylammonium tetrafluoroborate; e-PTh: electropolymerized PTh; and PEN: polyethylene naphthalate.

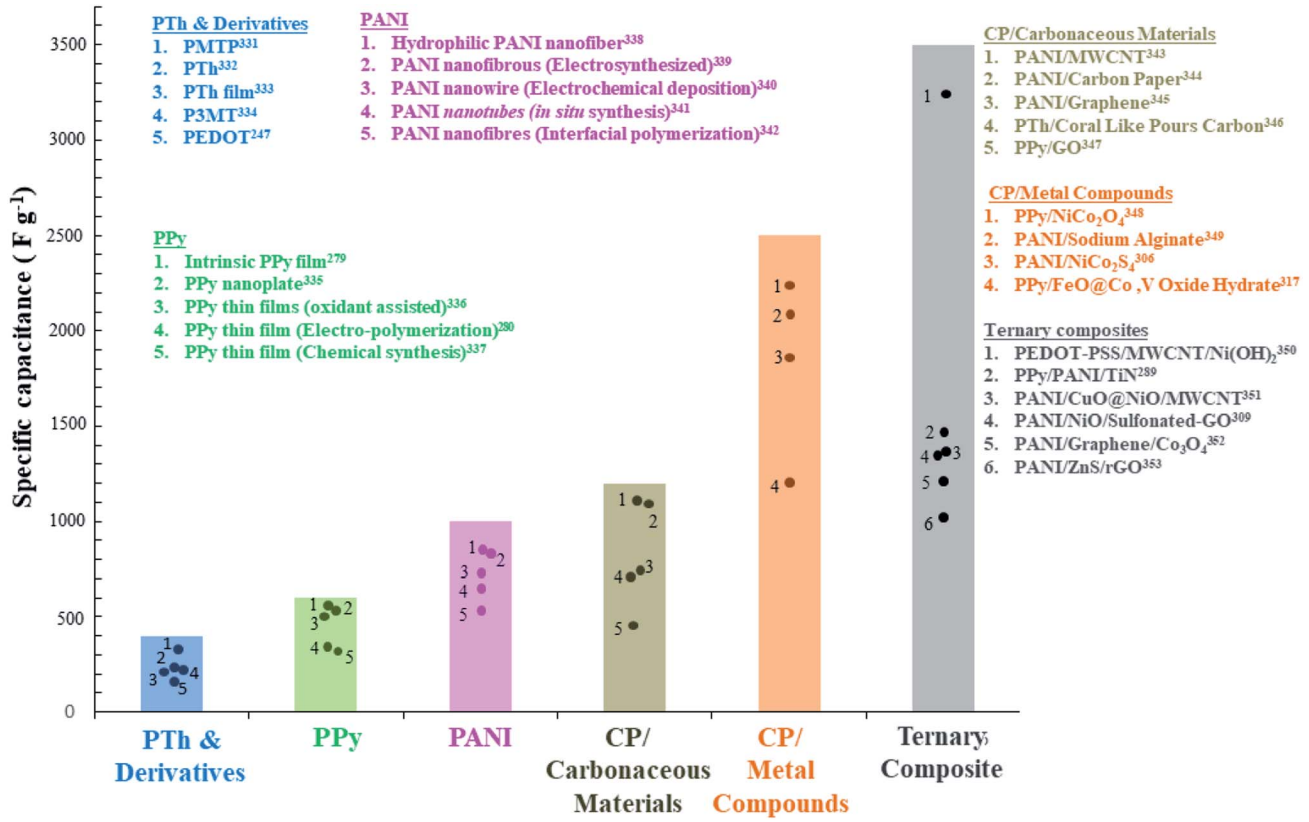

Fig. 22 Performance comparison of different conducting polymers and their composites for supercapacitor applications. Achieving a higher specific capacitance is not the prime objective of ternary composites; rather, improving structural integrity, and consequently, cycling stability is achieved.

nanoporous matrix and deposit on the surface of the TNTs (length: 4–5 μm and diameter: ~100 nm). The specific capacitances of PTh/TiO_2, PTh and TiO_2 were estimated to be 640, 24 and 0.65 F g^{-1} at 5 mV s^{-1} in the voltage window of −0.8 to 0 V *vs.* Ag/AgCl in 1 M H_2SO_4 electrolyte. In the GCD experiment, the PTh/TiO_2 electrode exhibited a specific capacitance of 632 F g^{-1} (@2 A g^{-1}), energy density of 237 W h kg^{-1} (@2100 W kg^{-1}) and moderate cycling stability (89% capacitance retention after 1100 cycles @ 2 A g^{-1}) in the voltage window of 0–0.7 V *vs.* Ag/AgCl. By contrast, the pristine PTh electrode showed 62% capacitance retention after 1100 cycles under a similar cycling schedule. The superior cycling performance of PTh/TiO_2 over the PTh electrode is attributed to the excellent mechanical stability of TNTs, which prevented the structural disintegration of PTh over repetitive doping/dedoping processes. Notably, the specific capacitances of PTh and its derivatives are comparatively lower than that of PANI and PPy, and therefore, the diverse binary and ternary composites of the PTh family are actually limited.

The design, development and electrochemical characterization of chemical supercapacitors based on PANI, PPy, PTh and derivatives of PTh have been consolidated herein. Further detailed literature screening on CP-based supercapacitors is presented in Table 5. In addition, Fig. 22 displays the comparative supercapacitive performances of the most popular CP-based active materials. Besides the PANI, PPy and PTh family, another class of CPs, namely redox CPs, are also reported in the literature, which are functionalized by redox active moieties to enhance their electrochemical performances. Poly(1,5-diaminoanthraquinone) (pDAAQ) with a redox active anthraquinone moiety is an example of a redox CP.[251] Another example is poly(2,2′-dithiodianiline) (pDTDA),[354] which a shows high specific capacity of 238 mA h g^{-1} (@2.3 V voltage window), high conductivity of 0.3–2.0 S cm^{-1} (@−2.0 to 0.8 V) and fast redox kinetics for the simultaneous occurrence of two redox reactions. The symmetric device with pDTDA showed energy and power densities of 25–46 W h kg^{-1} and 10.2–30.5 kW kg^{-1}, respectively, at a discharge rate in the range of 30–90 C. However, the commercial prospects of these polymers are limited due to their complex synthetic routes with high cost. In brief, PANI and PPy show very promising impacts for commercialization due to their environment-friendly synthesis, low cost raw materials, no air and moisture sensitivity, and finally great electrochemical performances.

6. Summary and future directions

This review demonstrated the journey of chemical supercapacitors from the first reported articles to recent developments. Conceptually, chemical supercapacitors originate from capacitors and have developed from EDL-based supercapacitors by incorporating facile surface-faradaic electron transfer processes. Various metallic compounds and conducting

polymers are found to be suitable as the active materials of chemical supercapacitors. Nevertheless, pristine metallic compounds and conducting polymers limit the electrochemical performances of devices due to their inherent drawbacks, which may be overcome by employing different mitigation strategies through unique material engineering, *i.e.*, forming conducting composites, nanostructuring, core/shell structure formation, morphology modification, and surface modulation. Most metal oxides and hydroxides are electronically insulating, which impedes the fast electron transfer between particles, and consequently slow reaction kinetics are observed. The composites with conducting carbons and polymers enhance the overall conductivity of the active materials, resulting in improved kinetic behaviours. Mixed metallic oxides and hydroxides show greater electrical conductivity due to the synergistic effects among multiple metallic sites. Defect modulation through the tuning of metal vacancies in solid crystals also enhances the electrical conductivity. Metal carbides, nitrides, phosphides, phosphates, phosphites, chalcogenides and conducting polymers have higher electrical conductivity compared to oxides and hydroxides, which indicates their better kinetic characteristics. Surface passivation is an important limitation for carbides, nitrides and phosphides in aqueous media, which restricts the performances of the devices. Different surface modulations, such as surface coating and elemental doping, and the optimization of the electrolyte medium are commonly accepted ways to tackle the surface passivation issue. The volume change of the particles upon charge/discharge is a common problem for all promising materials, *i.e.*, oxides, hydroxides, carbides, nitrides, phosphides, phosphates, phosphites, chalcogenides, and conducting polymers, which results in the pulverization of the active material particles. This event reduces the structural integrity of the electrodes and the durability of the devices is shortened. Various mitigation strategies are applied, which include nanostructuring, core/shell structure, and morphology control by incorporating void space in the particle. The buffer space is mandatory to sustain the volume change during cycling, and thus, pulverization of particles is prevented. To improve the structural integrity of the active materials, the formation of composites with robust support is truly indispensable. For example, conducting polymer-based electrodes show a limited cycle life, which can be improved by forming composites with mechanically sturdy carbonaceous materials (graphene, GO, rGO, CNTs, CNFs, *etc.*) and metallic compounds. Nanostructuring is an important modification route in materials science, which improves the electrochemical behaviours of the active materials by increasing their surface area and porosity. The kinetic characteristics of devices are also improved by nanostructuring due to the increase in the electrolyte infiltration rate and shortening of the diffusion lengths for electrolyte ions. Moreover, the additional porosity due to nanostructuring acts as a buffer region, which can sustain the excessive volume change of particles upon cycling. The above-discussed modifications greatly improve the electrochemical performances of chemical supercapacitors by increasing their specific capacitance (*i.e.*, superior energy density), reducing their internal resistance (*i.e.*, superior power density) and prolonging their cycling stability. Furthermore, based on these material engineering, metallic compounds and conducting polymers can be envisaged for successful chemical supercapacitors, bringing a paradigm shift in supercapacitor technology.

In reality, scaled-up stand-alone devices with these engineered materials are truly in their nascent stages of development, and further innovative steps need to be considered. Thus, here we identify a few futuristic directions for the successful realization of chemical supercapacitor devices.

(i) Multi-variant characteristics of pseudocapacitive processes in various active materials need to be theoretically modelled and validated to be the same using *in situ* and *ex situ* experimental tools, allowing exact charge storage mechanisms to be understood. For example, composite active materials (binary, ternary and even quaternary) are indispensable for successful devices. The design of these materials is not trivial. Thus, computational designs of composite materials from fundamental scientific knowledge are highly appreciable and their theoretical performances for supercapacitive applications need to be evaluated. If the theoretical performance data pass the required benchmarks, then these materials should be characterized experimentally through various *in situ* and *ex situ* spectroscopic, morphological, diffraction and electrochemical means. Combined theoretical and experimental studies are required to comprehend the electronic structures and corresponding charge storage mechanisms for defect modulation in solid crystals through cation vacancies. To date, these studies are mostly limited to oxides and carbides (MXenes). This defect modulation approach can be extended for other metallic compounds such as nitrides, phosphides, phosphate, phosphites and chalcogenides. In many instances, surface modification of the active materials/electrodes is imperative to enhance the device performances. Thus, theoretical understanding on the surface electronic structure should be the foundation for designing the modification routes. Thereafter, the surface modification needs to be experimentally validated. Accordingly, different sophisticated techniques, such as ALD and CVD, may be employed for the surface modifications of active materials/electrodes. In case of nanosizing, core/shell structuring, morphology modulations, *etc.*, theoretical feasibility screening should be conducted before experimental attempts. Briefly, theoretical insight regarding underline mechanisms and computational screening for envisaged materials are highly recommended prior to experimental expeditions.

(ii) The design and synthesis of different materials have to be continued in order to expand the material-bank for device optimizations. It is noteworthy that the synthesis of advanced electrode materials is not adequate for the progress of devices development. The other device components, such as the electrolyte, separator, current-collector, and cell container, are equally crucial, and thus research on these aspects are just as important for product development. Hence, material research on both the active and passive components of device should be conducted also.

(iii) Employing interdisciplinary approaches is mandatory for developing scaled-up practical devices. Materials scientists and engineers design and develop different classes of materials

from the knowledge of their chemistry, which are evaluated through various electrochemical means. Electrochemists perform fundamental studies on chemical supercapacitors and generate information about the feasibility of these systems. The design of practical devices including various process regulations, such as electrolyte flow and heat management, is the responsibility of chemical engineers. Also, collaborative efforts from mechanical and electrical engineers are required for the establishments of efficient mass scale production channels. Finally, electronic engineers design the relevant power electronic circuitry (similar to the Battery-Management-System/BMS in lithium-ion batteries) of chemical supercapacitors towards intended applications.

(iv) The environmental impact of the production chain for chemical supercapacitors needs to be addressed properly. The choice of materials is crucial in this concern. Non-toxic and non-hazardous materials should get immense consideration for device development. For example, non-toxic conducting polymers and metallic compounds of Mn, Fe, V, Zn, Ti, Cu, Sn, Bi, *etc.* should be prioritized over the toxic metallic compounds of Ru, Ni, Co, Cr, Pb, Mo, W, In, *etc.*, even though the latter group shows prominent supercapacitive performances. Similarly, non-hazardous aqueous electrolyte systems should be preferable over the hazardous organic media and ionic liquids, despite the sacrifice of higher energy characteristics. Recyclability is an important criterion for commercial devices, and thus product engineers should design devices with the maximum recyclability of its components.

(v) Finally, cost consideration is an important aspect for the commercialization of chemical supercapacitors. Generally, the cost component of any energy storage device primarily depends on the abundance of its contributing (major) elements in the Earth's crust and the state-of-the-art technology for production. The cost component related to the second concern may be reduced over time by technology developments, while the first concern is the actual limiting case. Therefore, researchers should focus on chemical supercapacitors that can be fabricated based on earth abundant elements. Hence, conducting polymers and metallic compounds of Mn, Fe, V, Zn, *etc.* should get much attention as active materials in practical devices. Moreover, low-cost electrolytes (*i.e.*, aqueous media), low cost current collectors (*i.e.*, Al, SS, and carbon cloth/paper), low cost separators (*i.e.*, polymeric membranes and ceramic sheets) and other low cost passive components need to be evaluated for commercial-scale devices. Finally, engineers should consider low cost and easily operated technologies for mass scale production.

Conflicts of interest

There are no conflicts to declare.

Acknowledgements

Financial supports from Science and Engineering Research Board (SERB), India (File No. SRG/2019/000296) and University Grants Commission (UGC), India (No. F.30-509/2020(BSR)) are gratefully acknowledged. PN thanks to Council of Scientific and Industrial Research (CSIR), India for Junior Research Fellowship (File No. 08/155(0064)/2019-EMR-1).

References

1 H. S. Williams, *A History of Science*, vol. II, Part VI: The Leyden Jar Discovered, retrieved, 2013-03-17.
2 A. K. Shukla, A. Banerjee, M. K. Ravikumar and A. Jalajakshi, *Electrochim. Acta*, 2012, **84**, 165–173.
3 J. P. Zheng, J. Huang and T. R. Jow, *J. Electrochem. Soc.*, 1997, **144**, 2026–2031.
4 J. R. Miller, in *Proc. 8th International Seminar on Double Layer Capacitors and Similar Energy Storage Devices*, Deerfield Beach, Florida, Dec. 7–9, 1998, 1998.
5 A. F. Burke, *Laboratory testing of high energy density capacitors for electric vehicles*, EG and G Idaho, Inc., Report No. EGG-EP-9885, October, 1991.
6 W. Duff, *A Text-Book of Physics*, P. Blakiston's Son & Co., Philadelphia, 1916.
7 J. Bird, *Electrical and Electronic Principles and Technology*, Routledge, 2010, pp. 63–76.
8 T. R. Marshall and T. F. Strange, *US Pat.*, US6299752B1, 2001.
9 B. E. Conway, *Electrochemical supercapacitors: scientific fundamentals and technological applications*, Kluwer Academic/Plenum Publishers, New Yourk, 1999.
10 J. O. Bockris, M. A. V. Devanathan, K. Müller and J. A. V. Butler, *Proc. R. Soc. London, Ser. A*, 1963, **274**, 55–79.
11 A. Burke, *J. Power Sources*, 2000, **91**, 37–50.
12 R. Kötz and M. Carlen, *Electrochim. Acta*, 2000, **45**, 2483–2498.
13 A. S. Aricò, P. Bruce, B. Scrosati, J. M. Tarascon and W. van Schalkwijk, *Nat. Mater.*, 2005, **4**, 366–377.
14 G. Wang, L. Zhang and J. Zhang, *Chem. Soc. Rev.*, 2012, **41**, 797–828.
15 F. Béguin and E. Frackowiak, *Carbons for electrochemical energy storage and conversion systems*, CRC Press, Boca Raton, 2009.
16 Y. Gogotsi, Y. Gogotsi and V. Presser, *Carbon Nanomaterials*, CRC Press, Boca Raton, 2006.
17 J. Yang, Y. Liu, S. Liu, L. Li, C. Zhang and T. Liu, *Mater. Chem. Front.*, 2017, **1**, 251–268.
18 C. An, Y. Zhang, H. Guo and Y. Wang, *Nanoscale Adv.*, 2019, **1**, 4644–4658.
19 S. Yuan, S. Y. Pang and J. Hao, *Appl. Phys. Rev.*, 2020, **7**, 21304.
20 Y. Zhou, W. Guo and T. Li, *Ceram. Int.*, 2019, **45**, 21062–21076.
21 X. Li, X. Xiao, Q. Li, J. Wei, H. Xue and H. Pang, *Inorg. Chem. Front.*, 2018, **5**, 11–28.
22 C. Costentin, T. R. Porter and J. M. Savéant, *ACS Appl. Mater. Interfaces*, 2017, **9**, 8649–8658.
23 M. Winter and R. J. Brodd, *Chem. Rev.*, 2004, **104**, 4245–4269.
24 T. Brezesinski, J. Wang, J. Polleux, B. Dunn and S. H. Tolbert, *J. Am. Chem. Soc.*, 2009, **131**, 1802–1809.

25 W. G. Pell and B. E. Conway, *J. Power Sources*, 2004, **136**, 334–345.
26 C. Xiang, K. M. Papadantonakis and N. S. Lewis, *Mater. Horiz.*, 2016, **3**, 169–173.
27 C. A. Kraus and R. M. Fuoss, *J. Am. Chem. Soc.*, 1933, **55**, 21–36.
28 S. Sundriyal, H. Kaur, S. K. Bhardwaj, S. Mishra, K. H. Kim and A. Deep, *Coord. Chem. Rev.*, 2018, **369**, 15–38.
29 O. M. Yaghi and H. Li, *J. Am. Chem. Soc.*, 1995, **117**, 10401–10402.
30 C. R. Deblase, K. E. Silberstein, T. T. Truong, H. D. Abruña and W. R. Dichtel, *J. Am. Chem. Soc.*, 2013, **135**, 16821–16824.
31 A. M. Khattak, Z. A. Ghazi, B. Liang, N. A. Khan, A. Iqbal, L. Li and Z. Tang, *J. Mater. Chem. A*, 2016, **4**, 16312–16317.
32 Y. Deng, Y. Xie, K. Zou and X. Ji, *J. Mater. Chem. A*, 2016, **4**, 1144–1173.
33 Y. Wen, B. Wang, C. Huang, L. Wang and D. Hulicova-Jurcakova, *Chem.–Eur. J.*, 2015, **21**, 80–85.
34 J. Tian, H. Zhang, Z. Liu, G. Qin and Z. Li, *Int. J. Hydrogen Energy*, 2018, **43**, 1596–1605.
35 L. Niu, Z. Li, W. Hong, J. Sun, Z. Wang, L. Ma, J. Wang and S. Yang, *Electrochim. Acta*, 2013, **108**, 666–673.
36 Y. An, Z. Li, Y. Yang, B. Guo, Z. Zhang, H. Wu and Z. Hu, *Adv. Mater. Interfaces*, 2017, **4**, 1700033.
37 W. Qian, F. Sun, Y. Xu, L. Qiu, C. Liu, S. Wang and F. Yan, *Energy Environ. Sci.*, 2014, **7**, 379–386.
38 C. Hao, B. Yang, F. Wen, J. Xiang, L. Li, W. Wang, Z. Zeng, B. Xu, Z. Zhao, Z. Liu and Y. Tian, *Adv. Mater.*, 2016, **28**, 3194–3201.
39 C. C. Chen, L. Fu and J. Maier, *Nature*, 2016, **536**, 159–164.
40 J. T. Mefford, W. G. Hardin, S. Dai, K. P. Johnston and K. J. Stevenson, *Nat. Mater.*, 2014, **13**, 726–732.
41 V. Ruiz, J. Suárez-Guevara and P. Gomez-Romero, *Electrochem. Commun.*, 2012, **24**, 35–38.
42 G. M. Suppes, C. G. Cameron and M. S. Freund, *J. Electrochem. Soc.*, 2010, **157**, A1030–A1034.
43 G. Nagaraju, S. M. Cha, S. C. Sekhar and J. S. Yu, *Adv. Energy Mater.*, 2017, **7**, 1601362.
44 S. Roldán, C. Blanco, M. Granda, R. Menéndez and R. Santamaría, *Angew. Chem., Int. Ed.*, 2011, **50**, 1699–1701.
45 E. Mourad, L. Coustan, P. Lannelongue, D. Zigah, A. Mehdi, A. Vioux, S. A. Freunberger, F. Favier and O. Fontaine, *Nat. Mater.*, 2017, **16**, 446–453.
46 Z. Tian, X. Tong, G. Sheng, Y. Shao, L. Yu, V. Tung, J. Sun, R. B. Kaner and Z. Liu, *Nat. Commun.*, 2019, **10**, 4913.
47 B. Zhuang, Z. Guo, W. Chu, Z. Cao, T. Bold and Y. Gao, *Electrochim. Acta*, 2018, **283**, 1589–1599.
48 S. Trasatti and G. Buzzanca, *J. Electroanal. Chem. Interfacial Electrochem.*, 1971, **29**, A1–A5.
49 D. Galizzioli, F. Tantardini and S. Trasatti, *J. Appl. Electrochem.*, 1974, **4**, 57–67.
50 S. Hadži-Jordanov, H. Angerstein-Kozlowska and B. E. Conway, *J. Electroanal. Chem. Interfacial Electrochem.*, 1975, **60**, 359–362.
51 S. Hadži-Jordanov, H. Angerstein-Kozlowska, M. Vukovič and B. E. Conway, *J. Electrochem. Soc.*, 1978, **125**, 1471–1480.
52 B. E. Conway, V. Birss and J. Wojtowicz, *J. Power Sources*, 1997, **66**, 1–14.
53 S. L. Roberson, R. F. Davis and D. Finello, in *Sixth Intel. Seminar on Double-Layer capacitors and Similar Energy Storage Devices*, ed. S. P. Wolsky and N. Matincic, Florida Educational Seminar, Florida, Boca Raton, 1996.
54 J. M. Miller, B. Dunn, T. D. Tran and R. W. Pekala, *J. Electrochem. Soc.*, 1997, **144**, L309–L311.
55 J. P. Zheng, P. J. Cygan and T. R. Jow, *J. Electrochem. Soc.*, 1995, **142**, 2699–2703.
56 P. J. Mahon and C. J. Drummond, *Aust. J. Chem.*, 2001, **54**, 473–476.
57 C. C. Hu, W. C. Chen and K. H. Chang, *J. Electrochem. Soc.*, 2004, **151**, A281–A290.
58 C. D. Lokhande, D. P. Dubal and O. S. Joo, *Curr. Appl. Phys.*, 2011, **11**, 255–270.
59 T. P. Gujar, V. R. Shinde, C. D. Lokhande, W. Y. Kim, K. D. Jung and O. S. Joo, *Electrochem. Commun.*, 2007, **9**, 504–510.
60 C. C. Hu, C. C. Wang and K. H. Chang, *Electrochim. Acta*, 2007, **52**, 2691–2700.
61 C. C. Hu and W. C. Chen, *Electrochim. Acta*, 2004, **49**, 3469–3477.
62 J. W. Long, K. E. Swider, C. I. Merzbacher and D. R. Rolison, *Langmuir*, 1999, **15**, 780–785.
63 H. Kim and B. N. Popov, *J. Power Sources*, 2002, **104**, 52–61.
64 D. Hong and S. Yim, *Langmuir*, 2018, **34**, 4249–4254.
65 J. R. Oh, J. H. Moon, S. Yoon, C. R. Park and Y. R. Do, *J. Mater. Chem.*, 2011, **21**, 14167–14172.
66 W. Wei, X. Cui, W. Chen and D. G. Ivey, *Chem. Soc. Rev.*, 2011, **40**, 1697–1721.
67 H. Y. Lee and J. B. Goodenough, *J. Solid State Chem.*, 1999, **144**, 220–223.
68 D. Bélanger, T. Brousse and J. W. Long, *Electrochem. Soc. Interface*, 2008, **17**, 49–52.
69 S. C. Pang, M. A. Anderson and T. W. Chapman, *J. Electrochem. Soc.*, 2000, **147**, 444–450.
70 S. F. Chin, S. C. Pang and M. A. Anderson, *J. Electrochem. Soc.*, 2002, **149**, A379–A384.
71 J. N. Broughton and M. J. Brett, *Electrochim. Acta*, 2004, **49**, 4439–4446.
72 S. Zhu, L. Li, J. Liu, H. Wang, T. Wang, Y. Zhang, L. Zhang, R. S. Ruoff and F. Dong, *ACS Nano*, 2018, **12**, 1033–1042.
73 H. Jia, Y. Cai, J. Lin, H. Liang, J. Qi, J. Cao, J. Feng and W. Fei, *Adv. Sci.*, 2018, **5**, 1700887.
74 K. D. Katzer, W. Mertin, G. Bacher, A. Jaeger and K. Streubel, *Appl. Phys. Lett.*, 2006, **89**, 103522.
75 P. Ruetschi, *J. Electrochem. Soc.*, 1984, **131**, 2737–2744.
76 P. Ruetschi, *J. Electrochem. Soc.*, 1988, **135**, 2657–2663.
77 P. Ruetschi and R. Giovanoli, *J. Electrochem. Soc.*, 1988, **135**, 2663–2669.
78 P. Gao, P. Metz, T. Hey, Y. Gong, D. Liu, D. D. Edwards, J. Y. Howe, R. Huang and S. T. Misture, *Nat. Commun.*, 2017, **8**, 14559.
79 W. Li, J. Shao, Q. Liu, X. Liu, X. Zhou and J. Hu, *Electrochim. Acta*, 2015, **157**, 108–114.

80 L. Liu, L. Su, J. Lang, B. Hu, S. Xu and X. Yan, *J. Mater. Chem. A*, 2017, **5**, 5523–5531.
81 H. Darjazi, S. S. Hosseiny Davarani, H. R. Moazami, T. Yousefi and F. Tabatabaei, *Prog. Nat. Sci.: Mater. Int.*, 2016, **26**, 523–527.
82 A. Banerjee, Y. Shilina, B. Ziv, J. M. Ziegelbauer, S. Luski, D. Aurbach and I. C. Halalay, *J. Am. Chem. Soc.*, 2017, **139**, 1738–1741.
83 H. Liu, A. Banerjee, B. Ziv, K. J. Harris, N. P. W. Pieczonka, S. Luski, G. A. Botton, G. R. Goward, D. Aurbach and I. C. Halalay, *ACS Appl. Energy Mater.*, 2018, **1**, 1878–1882.
84 J. Yan, E. Khoo, A. Sumboja and P. S. Lee, *ACS Nano*, 2010, **4**, 4247–4255.
85 A. Banerjee, B. Ziv, Y. Shilina, S. Luski, D. Aurbach and I. C. Halalay, *ACS Energy Lett.*, 2017, **2**, 2388–2393.
86 X. Chen, K. Chen, H. Wang and D. Xue, *Mater. Focus*, 2015, **4**, 78–80.
87 B. Xu, M. Zheng, H. Tang, Z. Chen, Y. Chi, L. Wang, L. Zhang, Y. Chen and H. Pang, *Nanotechnology*, 2019, **30**, 204002.
88 Q. Xia, M. Xu, H. Xia and J. Xie, *ChemNanoMat*, 2016, **2**, 588–600.
89 G. S. Gund, D. P. Dubal, N. R. Chodankar, J. Y. Cho, P. Gomez-Romero, C. Park and C. D. Lokhande, *Sci. Rep.*, 2015, **5**, 12454.
90 C. Guan, J. Liu, Y. Wang, L. Mao, Z. Fan, Z. Shen, H. Zhang and J. Wang, *ACS Nano*, 2015, **9**, 5198–5207.
91 F. Li, H. Chen, X. Y. Liu, S. J. Zhu, J. Q. Jia, C. H. Xu, F. Dong, Z. Q. Wen and Y. X. Zhang, *J. Mater. Chem. A*, 2016, **4**, 2096–2104.
92 R. Kumar, R. K. Singh, A. R. Vaz, R. Savu and S. A. Moshkalev, *ACS Appl. Mater. Interfaces*, 2017, **9**, 8880–8890.
93 C. Long, L. Jiang, T. Wei, J. Yan and Z. Fan, *J. Mater. Chem. A*, 2014, **2**, 16678–16686.
94 B. T. Liu, M. Zhao, L. P. Han, X. Y. Lang, Z. Wen and Q. Jiang, *Chem. Eng. J.*, 2018, **335**, 467–474.
95 D. S. Kong, J. M. Wang, H. B. Shao, J. Q. Zhang and C. N. Cao, *J. Alloys Compd.*, 2011, **509**, 5611–5616.
96 M. M. Sk, C. Y. Yue, K. Ghosh and R. K. Jena, *J. Power Sources*, 2016, **308**, 121–140.
97 S. Nandy, U. N. Maiti, C. K. Ghosh and K. K. Chattopadhyay, *J. Phys.: Condens. Matter*, 2009, **21**, 115804.
98 R. S. Kate, S. A. Khalate and R. J. Deokate, *J. Alloys Compd.*, 2018, **734**, 89–111.
99 M. S. Wu, M. J. Wang and J. J. Jow, *J. Power Sources*, 2010, **195**, 3950–3955.
100 T. Liu, L. Zhang, B. Cheng, W. You and J. Yu, *Chem. Commun.*, 2018, **54**, 3731–3734.
101 Y. Chen, Z. Huang, H. Zhang, Y. Chen, Z. Cheng, Y. Zhong, Y. Ye and X. Lei, *Int. J. Hydrogen Energy*, 2014, **39**, 16171–16178.
102 C. Li, J. Balamurugan, T. D. Thanh, N. H. Kim and J. H. Lee, *J. Mater. Chem. A*, 2017, **5**, 397–408.
103 C. Yuan, L. Yang, L. Hou, L. Shen, X. Zhang and X. W. Lou, *Energy Environ. Sci.*, 2012, **5**, 7883–7887.
104 G. S. Jang, S. Ameen, M. S. Akhtar and H. S. Shin, *Ceram. Int.*, 2018, **44**, 588–595.
105 T. Liu, L. Zhang, W. You and J. Yu, *Small*, 2018, **14**, 1702407.
106 W. Deng, W. Lan, Y. Sun, Q. Su and E. Xie, *Appl. Surf. Sci.*, 2014, **305**, 433–438.
107 X. Sun, Y. Lu, T. Li, S. Zhao, Z. Gao and Y. Y. Song, *J. Mater. Chem. A*, 2019, **7**, 372–380.
108 M. Selvakumar, D. Krishna Bhat, A. Manish Aggarwal, S. Prahladh Iyer and G. Sravani, *Phys. B*, 2010, **405**, 2286–2289.
109 M. K. Seo and S. J. Park, *Curr. Appl. Phys.*, 2010, **10**, 391–394.
110 D. W. Kim, K. Y. Rhee and S. J. Park, *J. Alloys Compd.*, 2012, **530**, 6–10.
111 Y. Chen, X. Zhang, D. Zhang, P. Yu and Y. Ma, *Carbon*, 2011, **49**, 573–580.
112 W. Sugimoto, T. Ohnuma, Y. Murakami and Y. Takasu, *Electrochem. Solid-State Lett.*, 2001, **4**, A145–A147.
113 G. Lota, E. Frackowiak, J. Mittal and M. Monthioux, *Chem. Phys. Lett.*, 2007, **434**, 73–77.
114 W. Zhang, Y. H. Qu and L. J. Gao, *Chin. Chem. Lett.*, 2012, **23**, 623–626.
115 A. Banerjee, M. K. Ravikumar, A. Jalajakshi, P. Suresh Kumar, S. A. Gaffoor and A. K. Shukla, *J. Chem. Sci.*, 2012, **124**, 747–762.
116 Y. Tian, S. Cong, W. Su, H. Chen, Q. Li, F. Geng and Z. Zhao, *Nano Lett.*, 2014, **14**, 2150–2156.
117 I. H. Kim, J. H. Kim, B. W. Cho, Y. H. Lee and K. B. Kim, *J. Electrochem. Soc.*, 2006, **153**, A989–A996.
118 T. P. Gujar, V. R. Shinde, C. D. Lokhande and S. H. Han, *J. Power Sources*, 2006, **161**, 1479–1485.
119 J. Chang, W. Lee, R. S. Mane, B. W. Cho and S. H. Han, *Electrochem. Solid-State Lett.*, 2008, **11**, A9–A11.
120 I. Heng, C. W. Lai, J. C. Juan, A. Numan, J. Iqbal and E. Y. L. Teo, *Ceram. Int.*, 2019, **45**, 4990–5000.
121 R. Barik, V. Tanwar, R. Kumar and P. P. Ingole, *J. Mater. Chem. A*, 2020, **8**, 15110–15121.
122 S. S. Karade, S. Lalwani, J. H. Eum and H. Kim, *J. Electroanal. Chem.*, 2020, **864**, 114080.
123 A. Banerjee and A. K. Shukla, *J. Chem. Sci.*, 2015, **127**, 967–977.
124 A. K. Shukla, A. Banerjee, M. K. Ravikumar and S. A. Gaffoor, *US Pat.*, US9036332B2, 2015.
125 A. K. Shukla and A. Banerjee, Indian Patent application no. 1454/CHE/2014, 2014.
126 A. Banerjee and A. K. Shukla, *Ionics*, 2014, **21**, 201–212.
127 A. Banerjee, R. Srinivasan and A. K. Shukla, *Bull. Mater. Sci.*, 2015, **38**, 129–133.
128 A. Banerjee, R. Srinivasan and A. K. Shukla, *ECS Electrochem. Lett.*, 2014, **3**, A1–A3.
129 A. Banerjee, S. K. Ramasesha and A. K. Shukla, *Electrochem. Energy Technol.*, 2015, **1**, 10–16.
130 Y. Gao, L. Mi, W. Wei, S. Cui, Z. Zheng, H. Hou and W. Chen, *ACS Appl. Mater. Interfaces*, 2015, **7**, 4311–4319.
131 R. Li, X. Ba, H. Zhang, P. Xu, Y. Li, C. Cheng and J. Liu, *Adv. Funct. Mater.*, 2018, **28**, 1800497.
132 P. R. Deshmukh, Y. Sohn and W. G. Shin, *ACS Sustainable Chem. Eng.*, 2018, **6**, 300–310.

133 B. Sarma, R. S. Ray, S. K. Mohanty and M. Misra, *Appl. Surf. Sci.*, 2014, **300**, 29–36.
134 X. Feng, Y. Huang, M. Chen, X. Chen, C. Li, S. Zhou and X. Gao, *J. Alloys Compd.*, 2018, **763**, 801–807.
135 A. K. Shukla, S. Venugopalan and B. Hariprakash, *J. Power Sources*, 2001, **100**, 125–148.
136 F. Shi, L. Li, X. L. Wang, C. D. Gu and J. P. Tu, *RSC Adv.*, 2014, **4**, 41910–41921.
137 D. A. Corrigan and S. L. Knight, *J. Electrochem. Soc.*, 1989, **136**, 613–619.
138 P. Oliva, J. Leonardi, J. F. Laurent, C. Delmas, J. J. Braconnier, M. Figlarz, F. Fievet and A. d. Guibert, *J. Power Sources*, 1982, **8**, 229–255.
139 R. Barnard, C. F. Randell and F. L. Tye, *J. Appl. Electrochem.*, 1980, **10**, 109–125.
140 P. E. Lokhande, K. Pawar and U. S. Chavan, *Mater. Sci. Energy Technol.*, 2018, **1**, 166–170.
141 G. W. Yang, C. L. Xu and H. L. Li, *Chem. Commun.*, 2008, 6537–6539.
142 H. Wang, H. S. Casalongue, Y. Liang and H. Dai, *J. Am. Chem. Soc.*, 2010, **132**, 7472–7477.
143 A. D. Jagadale, G. Guan, X. Du, X. Hao, X. Li and A. Abudula, *RSC Adv.*, 2015, **5**, 56942–56948.
144 K. A. Owusu, L. Qu, J. Li, Z. Wang, K. Zhao, C. Yang, K. M. Hercule, C. Lin, C. Shi, Q. Wei, L. Zhou and L. Mai, *Nat. Commun.*, 2017, **8**, 14264.
145 Y. Fan, L. Wang, Z. Ma, W. Dai, H. Shao, H. Wang and G. Shao, *Part. Part. Syst. Charact.*, 2018, **35**, 1700484.
146 X. Li, D. Du, Y. Zhang, W. Xing, Q. Xue and Z. Yan, *J. Mater. Chem. A*, 2017, **5**, 15460–15485.
147 J. Zhao, J. Chen, S. Xu, M. Shao, D. Yan, M. Wei, D. G. Evans and X. Duan, *J. Mater. Chem. A*, 2013, **1**, 8836–8843.
148 L. Xie, G. Sun, L. Xie, F. Su, X. Li, Z. Liu, Q. Kong, C. Lu, K. Li and C. Chen, *New Carbon Mater.*, 2016, **31**, 37–45.
149 P. Sivakumar, M. Jana, M. G. Jung, A. Gedanken and H. S. Park, *J. Mater. Chem. A*, 2019, **7**, 11362–11369.
150 H. Chen, F. Cai, Y. Kang, S. Zeng, M. Chen and Q. Li, *ACS Appl. Mater. Interfaces*, 2014, **6**, 19630–19637.
151 G. Xiong, P. He, L. Liu, T. Chen and T. S. Fisher, *J. Mater. Chem. A*, 2015, **3**, 22940–22948.
152 T. Brousse, D. Bélanger and J. W. Long, *J. Electrochem. Soc.*, 2015, **162**, A5185–A5189.
153 Y. Gogotsi and R. M. Penner, *ACS Nano*, 2018, **12**, 2081–2083.
154 G. Hu, C. Tang, C. Li, H. Li, Y. Wang and H. Gong, *J. Electrochem. Soc.*, 2011, **158**, A695.
155 J. Liu, J. Wang, C. Xu, H. Jiang, C. Li, L. Zhang, J. Lin and Z. X. Shen, *Adv. Sci.*, 2018, **5**, 1700322.
156 S. L. Brock and K. Senevirathne, *J. Solid State Chem.*, 2008, **181**, 1552–1559.
157 M. Naguib, R. R. Unocic, B. L. Armstrong and J. Nanda, *Dalton Trans.*, 2015, **44**, 9353–9358.
158 W. Lengauer, in *Handbook of Ceramic Hard Materials*, ed. R. Riedel, Wiley-VCH, Weinheim, Germany, 2000, vol. 1.
159 M. Naguib, J. Halim, J. Lu, K. M. Cook, L. Hultman, Y. Gogotsi and M. W. Barsoum, *J. Am. Chem. Soc.*, 2013, **135**, 15966–15969.
160 Y. Xiao, P. Sun and M. Cao, *ACS Nano*, 2014, **8**, 7846–7857.
161 M. Naguib, M. Kurtoglu, V. Presser, J. Lu, J. Niu, M. Heon, L. Hultman, Y. Gogotsi and M. W. Barsoum, *Adv. Mater.*, 2011, **23**, 4248–4253.
162 J. Theerthagiri, G. Durai, K. Karuppasamy, P. Arunachalam, V. Elakkiya, P. Kuppusami, T. Maiyalagan and H. S. Kim, *J. Ind. Eng. Chem.*, 2018, **67**, 12–27.
163 Y. Dall'Agnese, M. R. Lukatskaya, K. M. Cook, P. L. Taberna, Y. Gogotsi and P. Simon, *Electrochem. Commun.*, 2014, **48**, 118–122.
164 T. Morishita, Y. Soneda, H. Hatori and M. Inagaki, *Electrochim. Acta*, 2007, **52**, 2478–2484.
165 M. Kim and J. Kim, *Phys. Chem. Chem. Phys.*, 2014, **16**, 11323–11336.
166 Q. Shan, X. Mu, M. Alhabeb, C. E. Shuck, D. Pang, X. Zhao, X. F. Chu, Y. Wei, F. Du, G. Chen, Y. Gogotsi, Y. Gao and Y. Dall'Agnese, *Electrochem. Commun.*, 2018, **96**, 103–107.
167 Y. Xiao, J. Y. Hwang and Y. K. Sun, *J. Mater. Chem. A*, 2016, **4**, 10379–10393.
168 T. C. Liu, W. G. Pell, S. L. Roberson and B. E. Conway, *J. Electrochem. Soc.*, 1998, **145**, 1882–1888.
169 M. S. Balogun, W. Qiu, W. Wang, P. Fang, X. Lu and Y. Tong, *J. Mater. Chem. A*, 2015, **3**, 1364–1387.
170 J. Shi, B. Jiang, C. Li, F. Yan, D. Wang, C. Yang and J. Wan, *Mater. Chem. Phys.*, 2020, **245**, 122533.
171 X. Xiao, X. Peng, H. Jin, T. Li, C. Zhang, B. Gao, B. Hu, K. Huo and J. Zhou, *Adv. Mater.*, 2013, **25**, 5091–5097.
172 Z. H. Gao, H. Zhang, G. P. Cao, M. F. Han and Y. S. Yang, *Electrochim. Acta*, 2013, **87**, 375–380.
173 Z. Hou, K. Guo, H. Li and T. Zhai, *CrystEngComm*, 2016, **18**, 3040–3047.
174 F. Cheng, C. He, D. Shu, H. Chen, J. Zhang, S. Tang and D. E. Finlow, *Mater. Chem. Phys.*, 2011, **131**, 268–273.
175 G. H. An, D. Y. Lee and H. J. Ahn, *J. Mater. Chem. A*, 2017, **5**, 19714–19720.
176 F. Grote, H. Zhao and Y. Lei, *J. Mater. Chem. A*, 2015, **3**, 3465–3470.
177 A. Achour, M. Chaker, H. Achour, A. Arman, M. Islam, M. Mardani, M. Boujtita, L. Le Brizoual, M. A. Djouadi and T. Brousse, *J. Power Sources*, 2017, **359**, 349–354.
178 O. Kartachova, A. M. Glushenkov, Y. Chen, H. Zhang, X. J. Dai and Y. Chen, *J. Power Sources*, 2012, **220**, 298–305.
179 D. Choi and P. N. Kumta, *J. Am. Ceram. Soc.*, 2011, **94**, 2371–2378.
180 S. Wang, L. Zhang, C. Sun, Y. Shao, Y. Wu, J. Lv and X. Hao, *Adv. Mater.*, 2016, **28**, 3768–3776.
181 B. Wei, H. Liang, D. Zhang, Z. Wu, Z. Qi and Z. Wang, *J. Mater. Chem. A*, 2017, **5**, 2844–2851.
182 H. Cui, G. Zhu, X. Liu, F. Liu, Y. Xie, C. Yang, T. Lin, H. Gu and F. Huang, *Adv. Sci.*, 2015, **2**, 1500126.
183 A. Achour, R. Lucio-Porto, M. Chaker, A. Arman, A. Ahmadpourian, M. A. Soussou, M. Boujtita, L. Le Brizoual, M. A. Djouadi and T. Brousse, *Electrochem. Commun.*, 2017, **77**, 40–43.
184 S. Dong, X. Chen, L. Gu, X. Zhou, H. Wang, Z. Liu, P. Han, J. Yao, L. Wang, G. Cui and L. Chen, *Mater. Res. Bull.*, 2011, **46**, 835–839.

185 W. Du, R. Kang, P. Geng, X. Xiong, D. Li, Q. Tian and H. Pang, *Mater. Chem. Phys.*, 2015, **165**, 207–214.
186 Y. Lu, J. Liu, X. Liu, S. Huang, T. Wang, X. Wang, C. Gu, J. Tu and S. X. Mao, *CrystEngComm*, 2013, **15**, 7071–7079.
187 A. M. Elshahawy, C. Guan, X. Li, H. Zhang, Y. Hu, H. Wu, S. J. Pennycook and J. Wang, *Nano Energy*, 2017, **39**, 162–171.
188 H. Li, H. Yu, J. Zhai, L. Sun, H. Yang and S. Xie, *Mater. Lett.*, 2015, **152**, 25–28.
189 Y. Zhao, Z. Chen, D. B. Xiong, Y. Qiao, Y. Tang and F. Gao, *Sci. Rep.*, 2016, **6**, 17613.
190 C. Chen, N. Zhang, Y. He, B. Liang, R. Ma and X. Liu, *ACS Appl. Mater. Interfaces*, 2016, **8**, 23114–23121.
191 H. C. Chen, S. Jiang, B. Xu, C. Huang, Y. Hu, Y. Qin, M. He and H. Cao, *J. Mater. Chem. A*, 2019, **7**, 6241–6249.
192 Y. Wang, J. Liu, M. Xie, Y. Zhang, J. Chen, C. Du and L. Wan, *J. Alloys Compd.*, 2020, **843**, 155921.
193 Y. Gao, J. Zhao, Z. Run, G. Zhang and H. Pang, *Dalton Trans.*, 2014, **43**, 17000–17005.
194 J. Cherusseri, N. Choudhary, K. Sambath Kumar, Y. Jung and J. Thomas, *Nanoscale Horiz.*, 2019, **4**, 840–858.
195 J. Theerthagiri, K. Karuppasamy, G. Durai, A. u. H. S. Rana, P. Arunachalam, K. Sangeetha, P. Kuppusami and H. S. Kim, *Nanomaterials*, 2018, **8**, 256.
196 A. Eftekhari, *J. Mater. Chem. A*, 2017, **5**, 18299–18325.
197 M. Pumera, Z. Sofer and A. Ambrosi, *J. Mater. Chem. A*, 2014, **2**, 8981–8987.
198 Y. Yang, H. Fei, G. Ruan, C. Xiang and J. M. Tour, *Adv. Mater.*, 2014, **26**, 8163–8168.
199 S. Kandula, K. R. Shrestha, N. H. Kim and J. H. Lee, *Small*, 2018, **14**, 1800291.
200 W. Cai, T. Lai, J. Lai, H. Xie, L. Ouyang, J. Ye and C. Yu, *Sci. Rep.*, 2016, **6**, 26890.
201 N. Choudhary, C. Li, H. S. Chung, J. Moore, J. Thomas and Y. Jung, *ACS Nano*, 2016, **10**, 10726–10735.
202 S. J. Patil, A. C. Lokhande and C. D. Lokhande, *Mater. Sci. Semicond. Process.*, 2016, **41**, 132–136.
203 H. Peng, G. Ma, K. Sun, Z. Zhang, J. Li, X. Zhou and Z. Lei, *J. Power Sources*, 2015, **297**, 351–358.
204 S. E. Moosavifard, M. F. El-Kady, M. S. Rahmanifar, R. B. Kaner and M. F. Mousavi, *ACS Appl. Mater. Interfaces*, 2015, **7**, 4851–4860.
205 N. Maheswari and G. Muralidharan, *Appl. Surf. Sci.*, 2017, **416**, 461–469.
206 J. Geng, C. Ma, D. Zhang and X. Ning, *J. Alloys Compd.*, 2020, **825**, 153850.
207 C. Huang, Q. Zhu, W. Zhang, P. Qi, Q. Xiao and Y. Yu, *Electrochim. Acta*, 2020, **330**, 135209.
208 J. Zhu, L. Cao, Y. Wu, Y. Gong, Z. Liu, H. E. Hoster, Y. Zhang, S. Zhang, S. Yang, Q. Yan, P. M. Ajayan and R. Vajtai, *Nano Lett.*, 2013, **13**, 5408–5413.
209 F. Idrees, J. Hou, C. Cao, F. K. Butt, I. Shakir, M. Tahir and F. Idrees, *Electrochim. Acta*, 2016, **216**, 332–338.
210 L. Niu, Z. Li, Y. Xu, J. Sun, W. Hong, X. Liu, J. Wang and S. Yang, *ACS Appl. Mater. Interfaces*, 2013, **5**, 8044–8052.
211 Z. H. Huang, Y. Song, D. Y. Feng, Z. Sun, X. Sun and X. X. Liu, *ACS Nano*, 2018, **12**, 3557–3567.
212 H. Gao, S. Cao and Y. Cao, *Electrochim. Acta*, 2017, **240**, 31–42.
213 M. Sharma and A. Gaur, *J. Phys. Chem. C*, 2020, **124**, 9–16.
214 S. Arunachalam, B. Kirubasankar, E. Rajagounder Nagarajan, D. Vellasamy and S. Angaiah, *ChemistrySelect*, 2018, **3**, 12719–12724.
215 A. R. Selvaraj, H. J. Kim, K. Senthil and K. Prabakar, *J. Colloid Interface Sci.*, 2020, **566**, 485–494.
216 S. Patil, S. Raut, R. Gore and B. Sankapal, *New J. Chem.*, 2015, **39**, 9124–9131.
217 X. Fang, S. Han, D. Liu and Y. Zhu, *Chem. Phys. Lett.*, 2020, **746**, 137282.
218 J. Zhao, Z. Li, X. Yuan, Z. Yang, M. Zhang, A. Meng and Q. Li, *Adv. Energy Mater.*, 2018, **8**, 1702787.
219 A. Sanger, A. Kumar, A. Kumar, P. K. Jain, Y. K. Mishra and R. Chandra, *Ind. Eng. Chem. Res.*, 2016, **55**, 9452–9458.
220 K. Zhu, Y. Jin, F. Du, S. Gao, Z. Gao, X. Meng, G. Chen, Y. Wei and Y. Gao, *J. Energy Chem.*, 2019, **31**, 11–18.
221 J. Xiao, J. Wen, J. Zhao, X. Ma, H. Gao and X. Zhang, *Electrochim. Acta*, 2020, **337**, 135803.
222 K. J. Samdani, D. W. Joh and K. T. Lee, *J. Alloys Compd.*, 2018, **748**, 134–144.
223 Q. Jiang, N. Kurra, M. Alhabeb, Y. Gogotsi and H. N. Alshareef, *Adv. Energy Mater.*, 2018, **8**, 1703043.
224 R. Prakash, A. Kumar, A. Pandey and D. Kaur, *Int. J. Hydrogen Energy*, 2019, **44**, 10823–10832.
225 J. Balamurugan, T. T. Nguyen, V. Aravindan, N. H. Kim and J. H. Lee, *Adv. Funct. Mater.*, 2018, **28**, 1804663.
226 Y. Yu, W. Gao, Z. Shen, Q. Zheng, H. Wu, X. Wang, W. Song and K. Ding, *J. Mater. Chem. A*, 2015, **3**, 16633–16641.
227 X. Liu, W. Zang, C. Guan, L. Zhang, Y. Qian, A. M. Elshahawy, D. Zhao, S. J. Pennycook and J. Wang, *ACS Energy Lett.*, 2018, **3**, 2462–2469.
228 M. Ishaq, M. Jabeen, W. Song, L. Xu, W. Li and Q. Deng, *Electrochim. Acta*, 2018, **282**, 913–922.
229 X. Chen, M. Cheng, D. Chen and R. Wang, *ACS Appl. Mater. Interfaces*, 2016, **8**, 3892–3900.
230 D. Wang, L. Bin Kong, M. C. Liu, W. Bin Zhang, Y. C. Luo and L. Kang, *J. Power Sources*, 2015, **274**, 1107–1113.
231 M. Liu, N. Shang, X. Zhang, S. Gao, C. Wang and Z. Wang, *J. Alloys Compd.*, 2019, **791**, 929–935.
232 P. K. Katkar, S. J. Marje, S. S. Pujari, S. A. Khalate, A. C. Lokhande and U. M. Patil, *ACS Sustainable Chem. Eng.*, 2019, **7**, 11205–11218.
233 B. Li, Y. Shi, K. Huang, M. Zhao, J. Qiu, H. Xue and H. Pang, *Small*, 2018, **14**, 1703811.
234 R. Xu, J. Lin, J. Wu, M. Huang, L. Fan, X. He, Y. Wang and Z. Xu, *Appl. Surf. Sci.*, 2017, **422**, 597–606.
235 Z. Sun, X. Yang, H. Lin, F. Zhang, Q. Wang and F. Qu, *Inorg. Chem. Front.*, 2019, **6**, 659–670.
236 W. Luo, G. Zhang, Y. Cui, Y. Sun, Q. Qin, J. Zhang and W. Zheng, *J. Mater. Chem. A*, 2017, **5**, 11278–11285.
237 S. Wang, W. Li, L. Xin, M. Wu, Y. Long, H. Huang and X. Lou, *Chem. Eng. J.*, 2017, **330**, 1334–1341.
238 C. V. V. Muralee Gopi, A. E. Reddy and H. J. Kim, *J. Mater. Chem. A*, 2018, **6**, 7439–7448.

239 R. McNeill, R. Siudak, J. H. Wardlaw and D. E. Weiss, *Aust. J. Chem.*, 1963, **16**, 1056–1075.
240 B. A. Bolto and D. E. Weiss, *Aust. J. Chem.*, 1963, **16**, 1076–1089.
241 B. A. Bolto, R. McNeill and D. E. Weiss, *Aust. J. Chem.*, 1963, **16**, 1090–1103.
242 A. Rudge, I. Raistrick, S. Gottesfeld and J. P. Ferraris, *Electrochim. Acta*, 1994, **39**, 273–287.
243 A. Rudge, J. Davey, I. Raistrick, S. Gottesfeld and J. P. Ferraris, *J. Power Sources*, 1994, **47**, 89–107.
244 G. A. Snook, P. Kao and A. S. Best, *J. Power Sources*, 2011, **196**, 1–12.
245 S. Gottesfeld, A. Redondo and S. W. Feldberg, *J. Electrochem. Soc.*, 1987, **134**, 271–272.
246 B. E. Conway and B. E. Conway, in *Electrochemical Supercapacitors*, Springer, 1999, pp. 299–334.
247 K. Lota, V. Khomenko and E. Frackowiak, *J. Phys. Chem. Solids*, 2004, **65**, 295–301.
248 D. Kumar, A. Banerjee, S. Patil and A. K. Shukla, *Bull. Mater. Sci.*, 2015, **38**, 1507–1517.
249 S. Suematsu, Y. Oura, H. Tsujimoto, H. Kanno and K. Naoi, *Electrochim. Acta*, 2000, **45**, 3813–3821.
250 Q. Meng, K. Cai, Y. Chen and L. Chen, *Nano Energy*, 2017, **36**, 268–285.
251 K. Naoi, S. Suematsu and A. Manago, *J. Electrochem. Soc.*, 2000, **147**, 420–426.
252 M. Skompska, J. Mieczkowski, R. Holze and J. Heinze, *J. Electroanal. Chem.*, 2005, **577**, 9–17.
253 M. D. Levi, Y. Gofer, D. Aurbach, M. Lapkowski, E. Vieil and J. Serose, *J. Electrochem. Soc.*, 2000, **147**, 1096–1104.
254 G. A. Snook and G. Z. Chen, *J. Electroanal. Chem.*, 2008, **612**, 140–146.
255 K. S. Ryu, K. M. Kim, N. G. Park, Y. J. Park and S. H. Chang, *J. Power Sources*, 2002, **103**, 305–309.
256 F. Faverolle, A. J. Attias, B. Bloch, P. Audebert and C. P. Andrieux, *Chem. Mater.*, 1998, **10**, 740–752.
257 M. Mastragostino, C. Arbizzani and F. Soavi, *Solid State Ionics*, 2002, **148**, 493–498.
258 H. Talbi, P. E. Just and L. H. Dao, *J. Appl. Electrochem.*, 2003, **33**, 465–473.
259 A. G. Pandolfo and A. F. Hollenkamp, *J. Power Sources*, 2006, **157**, 11–27.
260 J. H. Park and O. O. Park, *J. Power Sources*, 2002, **111**, 185–190.
261 S. R. Sivakkumar and D. W. Kim, *J. Electrochem. Soc.*, 2007, **154**, A134–A139.
262 S. R. Sivakkumar, D. R. MacFarlane, M. Forsyth and D. W. Kim, *J. Electrochem. Soc.*, 2007, **154**, A834–A838.
263 G. Louarn, M. Lapkowski, S. Quillard, A. Pron, J. P. Buisson and S. Lefrant, *J. Phys. Chem.*, 1996, **100**, 6998–7006.
264 D. W. Hatchett, M. Josowicz and J. Janata, *J. Electrochem. Soc.*, 1999, **146**, 4535–4538.
265 H. D. Tran, J. M. D'Arcy, Y. Wang, P. J. Beltramo, V. A. Strong and R. B. Kaner, *J. Mater. Chem.*, 2011, **21**, 3534–3550.
266 K. S. Ryu, K. M. Kim, Y. J. Park, N. G. Park, M. G. Kang and S. H. Chang, *Solid State Ionics*, 2002, **152–153**, 861–866.
267 S. R. Sivakkumar and R. Saraswathi, *J. Power Sources*, 2004, **137**, 322–328.
268 H. Zhou, H. Chen, S. Luo, G. Lu, W. Wei and Y. Kuang, *J. Solid State Electrochem.*, 2005, **9**, 574–580.
269 H. Li, J. Wang, Q. Chu, Z. Wang, F. Zhang and S. Wang, *J. Power Sources*, 2009, **190**, 578–586.
270 K. Wang, J. Huang and Z. Wei, *J. Phys. Chem. C*, 2010, **114**, 8062–8067.
271 J. Liu, J. Sun and L. Gao, *J. Phys. Chem. C*, 2010, **114**, 19614–19620.
272 X. F. Lu, X. Y. Chen, W. Zhou, Y. X. Tong and G. R. Li, *ACS Appl. Mater. Interfaces*, 2015, **7**, 14843–14850.
273 J. Zhang, L. Shi, H. Liu, Z. Deng, L. Huang, W. Mai, S. Tan and X. Cai, *J. Alloys Compd.*, 2015, **651**, 126–134.
274 J. Zhu, W. Sun, D. Yang, Y. Zhang, H. H. Hoon, H. Zhang and Q. Yan, *Small*, 2015, **11**, 4123–4129.
275 A. K. Das, S. K. Karan and B. B. Khatua, *Electrochim. Acta*, 2015, **180**, 1–15.
276 K. Naoi, Y. Oura and H. Tsujimoto, in *Proceedings of the Symposium on ElectrochemicalCapacitors II*, ed. F. M. Delnick, D. Ingersoll, X. Andrieu and K. Naoi, Electrochemical Society Inc., Pennington, 1997, vol. 96, pp. 120–126.
277 J. O. Iroh and K. Levine, *J. Power Sources*, 2003, **117**, 267–272.
278 Q. Yang, Z. Hou and T. Huang, *J. Appl. Polym. Sci.*, 2015, **132**, 41615.
279 M. Li and L. Yang, *J. Mater. Sci.: Mater. Electron.*, 2015, **26**, 4875–4879.
280 M. Rajesh, C. J. Raj, B. C. Kim, B. B. Cho, J. M. Ko and K. H. Yu, *Electrochim. Acta*, 2016, **220**, 373–383.
281 W. Wu, L. Yang, S. Chen, Y. Shao, L. Jing, G. Zhao and H. Wei, *RSC Adv.*, 2015, **5**, 91645–91653.
282 J. Keskinen, S. Tuurala, M. Sjödin, K. Kiri, L. Nyholm, T. Flyktman, M. Strømme and M. Smolander, *Synth. Met.*, 2015, **203**, 192–199.
283 C. J. Raj, B. C. Kim, W. J. Cho, W. G. Lee, S. D. Jung, Y. H. Kim, S. Y. Park and K. H. Yu, *ACS Appl. Mater. Interfaces*, 2015, **7**, 13405–13414.
284 B. Gao, D. He, B. Yan, H. Suo and C. Zhao, *J. Mater. Sci.: Mater. Electron.*, 2015, **26**, 6373–6379.
285 C. Zhou, Y. Zhang, Y. Li and J. Liu, *Nano Lett.*, 2013, **13**, 2078–2085.
286 M. Zhu, Y. Huang, Q. Deng, J. Zhou, Z. Pei, Q. Xue, Y. Huang, Z. Wang, H. Li, Q. Huang and C. Zhi, *Adv. Energy Mater.*, 2016, **6**, 1600969.
287 J. Liu, L. Zhang, H. Bin Wu, J. Lin, Z. Shen and X. W. Lou, *Energy Environ. Sci.*, 2014, **7**, 3709–3719.
288 J. Zhou, H. Zhao, X. Mu, J. Chen, P. Zhang, Y. Wang, Y. He, Z. Zhang, X. Pan and E. Xie, *Nanoscale*, 2015, **7**, 14697–14706.
289 Y. Xie and D. Wang, *J. Alloys Compd.*, 2016, **665**, 323–332.
290 D. Villers, D. Jobin, C. Soucy, D. Cossement, R. Chahine, L. Breau and D. Bélanger, *J. Electrochem. Soc.*, 2003, **150**, A747–A752.
291 C. Arbizzani, M. Mastragostino and L. Meneghello, *Electrochim. Acta*, 1995, **40**, 2223–2228.

292 C. Arbizzani, M. Catellani, M. Mastragostino and C. Mingazzini, *Electrochim. Acta*, 1995, **40**, 1871–1876.
293 K. S. Ryu, Y. G. Lee, Y. S. Hong, Y. J. Park, X. Wu, K. M. Kim, M. G. Kang, N. G. Park and S. H. Chang, *Electrochim. Acta*, 2004, **50**, 843–847.
294 A. Laforgue, P. Simon, J. F. Fauvarque, J. F. Sarrau and P. Lailler, *J. Electrochem. Soc.*, 2001, **148**, A1130–A1134.
295 C. Arbizzani, M. Mastragostino and F. Soavi, *J. Power Sources*, 2001, **100**, 164–170.
296 H. Zhang, Z. Hu, M. Li, L. Hu and S. Jiao, *J. Mater. Chem. A*, 2014, **2**, 17024–17030.
297 A. Alabadi, S. Razzaque, Z. Dong, W. Wang and B. Tan, *J. Power Sources*, 2016, **306**, 241–247.
298 M. R. Karim, J. H. Yeum, M. S. Lee and K. T. Lim, *Mater. Chem. Phys.*, 2008, **112**, 779–782.
299 J. Hong, I. H. Yeo and W. Paik, *J. Electrochem. Soc.*, 2001, **148**, A156–A163.
300 R. B. Ambade, S. B. Ambade, N. K. Shrestha, Y. C. Nah, S. H. Han, W. Lee and S. H. Lee, *Chem. Commun.*, 2013, **49**, 2308–2310.
301 H. Peng, G. Ma, J. Mu, K. Sun and Z. Lei, *J. Mater. Chem. A*, 2014, **2**, 10384–10388.
302 J. Fu, J. Yun, S. Wu, L. Li, L. Yu and K. H. Kim, *ACS Appl. Mater. Interfaces*, 2018, **10**, 34212–34221.
303 P. Yu, Z. Zhang, L. Zheng, F. Teng, L. Hu and X. Fang, *Adv. Energy Mater.*, 2016, **6**, 1601111.
304 D. Salinas-Torres, J. M. Sieben, D. Lozano-Castelló, D. Cazorla-Amorós and E. Morallón, *Electrochim. Acta*, 2013, **89**, 326–333.
305 J. Zhao, Y. Li, X. Chen, H. Zhang, C. Song, Z. Liu, K. Zhu, K. Cheng, K. Ye, J. Yan, D. Cao, G. Wang and X. Zhang, *Electrochim. Acta*, 2018, **292**, 458–467.
306 X. He, Q. Liu, J. Liu, R. Li, H. Zhang, R. Chen and J. Wang, *Chem. Eng. J.*, 2017, **325**, 134–143.
307 F. S. Omar, A. Numan, N. Duraisamy, M. M. Ramly, K. Ramesh and S. Ramesh, *Electrochim. Acta*, 2017, **227**, 41–48.
308 X. Li, J. Shen, W. Sun, X. Hong, R. Wang, X. Zhao and X. Yan, *J. Mater. Chem. A*, 2015, **3**, 13244–13253.
309 C. Huang, C. Hao, W. Zheng, S. Zhou, L. Yang, X. Wang, C. Jiang and L. Zhu, *Appl. Surf. Sci.*, 2020, **505**, 144589.
310 J. Shen, C. Yang, X. Li and G. Wang, *ACS Appl. Mater. Interfaces*, 2013, **5**, 8467–8476.
311 S. K. Tripathi, A. Kumar and S. A. Hashmi, *Solid State Ionics*, 2006, **177**, 2979–2985.
312 L. Long, Y. Yao, M. Yan, H. Wang, G. Zhang, M. Kong, L. Yang, X. Liao, G. Yin and Z. Huang, *J. Mater. Sci.*, 2017, **52**, 3642–3656.
313 N. Wang, X. Wang, Y. Zhang, W. Hou, Y. Chang, H. Song, Y. Zhao and G. Han, *J. Alloys Compd.*, 2020, **835**, 155299.
314 D. P. Dubal, N. R. Chodankar, Z. Caban-Huertas, F. Wolfart, M. Vidotti, R. Holze, C. D. Lokhande and P. Gomez-Romero, *J. Power Sources*, 2016, **308**, 158–165.
315 X. Zhang, J. Zhang, Y. Chen, K. Cheng, J. Yan, K. Zhu, K. Ye, G. Wang, L. Zhou and D. Cao, *J. Colloid Interface Sci.*, 2019, **536**, 291–299.
316 S. Liu, C. An, X. Chang, H. Guo, L. Zang, Y. Wang, H. Yuan and L. Jiao, *J. Mater. Sci.*, 2018, **53**, 2658–2668.
317 A. Maitra, A. K. Das, S. K. Karan, S. Paria, R. Bera and B. B. Khatua, *Ind. Eng. Chem. Res.*, 2017, **56**, 2444–2457.
318 S. Dhibar, A. Roy and S. Malik, *Eur. Polym. J.*, 2019, **120**, 109203.
319 C. Huang, C. Ni, L. Yang, T. Zhou, C. Hao, X. Wang, C. Ge and L. Zhu, *J. Alloys Compd.*, 2020, **829**, 154536.
320 S. Kulandaivalu, N. Suhaimi and Y. Sulaiman, *Sci. Rep.*, 2019, **9**, 4884.
321 S. Deshagani, A. Das, D. Nepak and M. Deepa, *ACS Appl. Polym. Mater.*, 2020, **2**, 1190–1202.
322 M. Rajesh, C. J. Raj, R. Manikandan, B. C. Kim, S. Y. Park and K. H. Yu, *Mater. Today Energy*, 2017, **6**, 96–104.
323 H. Vijeth, S. P. Ashokkumar, L. Yesappa, M. Niranjana, M. Vandana and H. Devendrappa, *J. Mater. Sci.: Mater. Electron.*, 2019, **30**, 7471–7484.
324 M. A. A. Mohd Abdah, N. H. N. Azman, S. Kulandaivalu and Y. Sulaiman, *Sci. Rep.*, 2019, **9**, 1–9.
325 H. Vijeth, S. P. Ashokkumar, L. Yesappa, M. Niranjana, M. Vandana and H. Devendrappa, *RSC Adv.*, 2018, **8**, 31414–31426.
326 K. Balakrishnan, M. Kumar and A. Subramania, *Adv. Mater. Res.*, 2014, **938**, 151–157.
327 I. K. Moon, B. Ki and J. Oh, *Chem. Eng. J.*, 2020, **392**, 123794.
328 A. Laforgue, P. Simon, J. F. Fauvarque, M. Mastragostino, F. Soavi, J. F. Sarrau, P. Lailler, M. Conte, E. Rossi and S. Saguatti, *J. Electrochem. Soc.*, 2003, **150**, A645–A651.
329 R. B. Ambade, S. B. Ambade, R. R. Salunkhe, V. Malgras, S. H. Jin, Y. Yamauchi and S. H. Lee, *J. Mater. Chem. A*, 2016, **4**, 7406–7415.
330 N. Kurra, R. Wang and H. N. Alshareef, *J. Mater. Chem. A*, 2015, **3**, 7368–7374.
331 X. Ju, L. Kong, J. Zhao and G. Bai, *Electrochim. Acta*, 2017, **238**, 36–48.
332 A. Laforgue, P. Simon, C. Sarrazin and J.-F. Fauvarque, *J. Power Sources*, 1999, **80**, 142–148.
333 B. H. Patil, A. D. Jagadale and C. D. Lokhande, *Synth. Met.*, 2012, **162**, 1400–1405.
334 P. Sivaraman, A. P. Thakur and K. Shashidhara, *Synth. Met.*, 2020, **259**, 116255.
335 D. P. Dubal, S. V. Patil, A. D. Jagadale and C. D. Lokhande, *J. Alloys Compd.*, 2011, **509**, 8183–8188.
336 S. S. Shinde, G. S. Gund, D. P. Dubal, S. B. Jambure and C. D. Lokhande, *Electrochim. Acta*, 2014, **119**, 1–10.
337 S. S. Shinde, G. S. Gund, V. S. Kumbhar, B. H. Patil and C. D. Lokhande, *Eur. Polym. J.*, 2013, **49**, 3734–3739.
338 D. S. Dhawale, R. R. Salunkhe, V. S. Jamadade, D. P. Dubal, S. M. Pawar and C. D. Lokhande, *Curr. Appl. Phys.*, 2010, **10**, 904–909.
339 D. S. Dhawale, D. P. Dubal, V. S. Jamadade, R. R. Salunkhe and C. D. Lokhande, *Synth. Met.*, 2010, **160**, 519–522.
340 V. Gupta and N. Miura, *Electrochem. Solid-State Lett.*, 2005, **8**, A630.
341 W. Wu, D. Pan, Y. Li, G. Zhao, L. Jing and S. Chen, *Electrochim. Acta*, 2015, **152**, 126–134.

342 H. Guan, L. Z. Fan, H. Zhang and X. Qu, *Electrochim. Acta*, 2010, **56**, 964–968.
343 G. P. Shumakovich, O. V. Morozova, M. E. Khlupova, I. S. Vasil'eva, E. A. Zaitseva and A. I. Yaropolov, *RSC Adv.*, 2017, **7**, 34192–34196.
344 C. Hu, S. He, S. Jiang, S. Chen and H. Hou, *RSC Adv.*, 2015, **5**, 14441–14447.
345 H. P. Cong, X. C. Ren, P. Wang and S. H. Yu, *Energy Environ. Sci.*, 2013, **6**, 1185–1191.
346 Y. Wang, S. Tao, Y. An, S. Wu and C. Meng, *J. Mater. Chem. A*, 2013, **1**, 8876–8887.
347 J. Cao, Y. Wang, J. Chen, X. Li, F. C. Walsh, J.-H. Ouyang, D. Jia and Y. Zhou, *J. Mater. Chem. A*, 2015, **3**, 14445–14457.
348 D. Kong, W. Ren, C. Cheng, Y. Wang, Z. Huang and H. Y. Yang, *ACS Appl. Mater. Interfaces*, 2015, **7**, 21334–21346.
349 Y. Li, X. Zhao, Q. Xu, Q. Zhang and D. Chen, *Langmuir*, 2011, **27**, 6458–6463.
350 W. Jiang, D. Yu, Q. Zhang, K. Goh, L. Wei, Y. Yong, R. Jiang, J. Wei and Y. Chen, *Adv. Funct. Mater.*, 2015, **25**, 1063–1073.
351 I. Chakraborty, N. Chakrabarty, A. Senapati and A. K. Chakraborty, *J. Phys. Chem. C*, 2018, **122**, 27180–27190.
352 H. Lin, Q. Huang, J. Wang, J. Jiang, F. Liu, Y. Chen, C. Wang, D. Lu and S. Han, *Electrochim. Acta*, 2016, **191**, 444–451.
353 Z. Xu, Z. Zhang, H. Yin, S. Hou, H. Lin, J. Zhou and S. Zhuo, *RSC Adv.*, 2020, **10**, 3122–3129.
354 K. Naoi, K. Kawase, M. Mori and M. Komiyama, *J. Electrochem. Soc.*, 1997, **144**, L173–L175.